Enhanced Stability and Photovoltaic Performance of Perovskite Solar Cells Prepared in Ambient Atmosphere

Enhanced Stability and Photovoltaic Performance of Perovskite Solar Cells Prepared in Ambient Atmosphere

Graduate School of Life Science and System Engineering
Kyushu Institute of Technology

Dissertation for the Degree of Doctor of Philosophy

Fu Yang

February 2019

Supervisor: Professor Shuzi Hayase

Abstract

Halide perovskite solar cells have gained overall attention because of high power convention efficiency and low-cost fabrication process. However, the most researchers use glovebox for the perovskite fabrication as the perovskite materials are easily affected by water, oxygen and other uncontrolled condition, which increases the fabrication cost and prevent the commercialization of perovskite solar cells. Therefore, research in preparing perovskite solar cells in ambient air condition is changeling and meaningful. Herein, the thesis mainly focuses on the fabrication of high-performance perovskite solar cells in ambient air condition.

In chapter 1, the background of perovskite solar cells is discussed. The existing challenge is pointed out for the commercialization of perovskite solar cells. Finally, the research state of ambient air processed perovskite solar cells are reviewed.

In chapter 2, the research on different acetate based antisolvent was compared for preparing high-quality $CH_3NH_3PbI_3$ perovskite film in the ambient air condition. The quality of perovskite film was checked by UV-vis, X-ray, SEM and AFM spectra. The photovoltaic performance was investigated by planar perovskite solar cells.

In chapter 3, alcohols were used as the additive into diethyl ether antisolvent for the enhanced crystallization of $CH_3NH_3PbI_3$ perovskite layer in humid atmosphere. The results were proved by the X-ray, SEM, AFM and FTIR spectra. The photovoltaic performance was investigated by the planar perovskite solar cells.

In chapter 4, magnesium (II) iodide was used as a dopant into $CH_3NH_3PbI_3$ perovskite for enhanced crystallinity and stability. The magnesium doped perovskite showed a decreased bandgap and deeper valence band level which was proved by the photoelectron yield spectroscopy and UV-vis spectra. The perovskite film contained a bigger grain size when magnesium was incorporated into the perovskite layer. Finally, the photovoltaic performance was investigated by the mesoporous perovskite solar cells.

In chapter 5, a pyrene core based organic, 1-(ammonium acetyl) pyrene was used for the 2D materials into $CH_3NH_3PbI_3$ perovskite layer for the 2D/3D heterostructure in humid atmosphere. The 2D/3D perovskite film was proved by the X-ray spectra and showed obvious stability in the humid air condition. Furthermore, 2D/3D perovskite showed an increased

bandgap and deeper valence band level which was proved by the photoelectron yield spectroscopy and UV-vis spectra. Finally, the photovoltaic performance was investigated by the planar perovskite solar cells.

In chapter 6, all-inorganic perovskite, $CsPb_{1-x}Ge_xI_2Br$, was prepared in the humid air condition. The germanium incorporated $CsPbI_2Br$ perovskite showed great phase stability compared to the pure $CsPbI_2Br$ perovskite, which was proved by the UV-vis spectra and X-ray spectra. At last, the photovoltaic performance was investigated by the planar perovskite solar cells.

In the final chapter 7, general conclusions were summarized. Researches in preparing high-quality perovskite solar cells in ambient air condition are still changelings. For the commercialization of perovskite solar cells, fabricating the high-performance perovskite devices without using the glovebox is greatly needed.

Table of contents

Chapter 1. Introduction

1.1 Perovskite solar cells

The organometallic halide perovskite solar cells (PSCs) has attracted overall attention due to their super charge carrier mobility, high absorption coefficient and band gaps close to Shockley-Queisser limit.[1-2] From 2009, Miyasaka et.al first applied the organometallic halide perovskite in to dye-sensitized solar cell to obtain power convention efficiency (PCE) of 3.8%.[3] However, the perovskite materials is easily degraded because of the liquid electrode. In order to solve this problem, in 2012, Park et al. first introduced solid hole transport material, Spiro-OMeTAD, into the perovskite solar cell to get a PCE of 9.7% along with a better PSCs` stability.[4] At the same year, Snaith et al. first introduced chloride into the perovskite layer $CH_3NH_3PbI_{3-x}Cl_x$, which greatly improved the carrier transmission distance and the PSCs` stability. Meanwhile, they replaced the mesoporous titanium dioxide with insulation material aluminum oxide, which proved that the perovskite can not only acted as light absorbance layer, but also acted as the electron transport layer. The efficiency of the reformed PSCs has been increased up to 10.9%.[5-6] Later in 2012, Etgar et al. directly evaporated gold on the $CH_3NH_3PbI_3$ layer achieving the PCE of 5.5%, which proved that the perovskite layer could also act as the hole transport layer.[7]

After 2012, the PSCs came to the repaid developing period. In 2013, Gratzel et al introduced two-step method to prepare the $CH_3NH_3PbI_3$ perovskite layer and achieved a high PCE up to 15%.[8] Later, Snaith et al. intruded the thermal vapor deposition method to obtain a dense perovskite film along with the PCE up to 15.4%.[1] In 2014, Yang et al. used polyethyleneimine ethoxylated (PEIE) to modify the ITO electrode and doped the TiO_2 layer

with yttrium achieving high PCE of 19.3%.[9] In 2016, Seong Sik Shin et al doped HI by intramolecular exchanging process achieving a breakthrough PCE of 22.1%.[10] And until now, the PCE of the PSCs is still keeping on increasing, which reaching a much higher level than other third-generation solar cells.

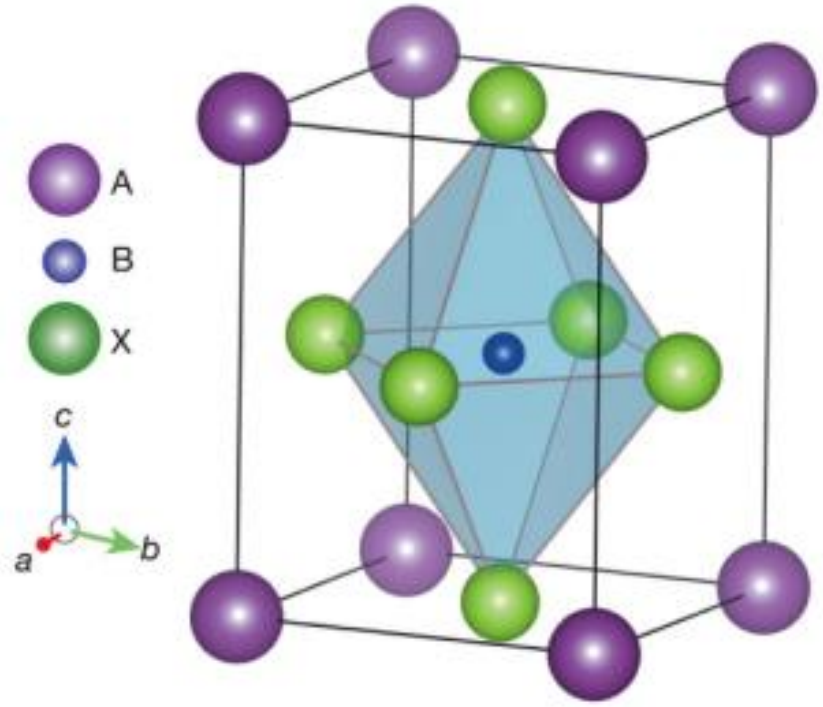

Figure 1.1 Crystal structure of ABX_3 perovskite materials.

1.2 Structure of perovskite solar cells

Perovskite generally means the crystal structure related to the structure of mineral $CaTiO_3$. ABX_3 is used as the general description of the perovskite structure, where A and B are cations, and X is anion. The crystal structure is shown in Figure 1.1. The A, B, and X ions form a simple cubic crystal structure, where A is located in the center, B is located at the top corner, and X is located at the midpoint of the 12 ribs of the cubic structure. For the

perovskite materials used into the solar cells, A is usually large cation, like $CH_3NH_3^+$, $NH_2CH{=}NH_2^+$, Cs^+, to balance the electric charge. B is usually the metal cation, such as Pb^{2+}, Sn^{2+} , Ge^{2+}, and X is usually halide, such as I^-, Br^- and Cl^-.

The stability of perovskite crystal structure is related to the tolerance factor (TF), which can be defined by the following equation:

$$TF = \frac{R_A + R_x}{\sqrt{2}(R_B + R_X)}$$

where R_A, R_B and R_X represent the radius of A, B, X ions. For the high-symmetry cubic structure, the TF is near 1. Therefore, A ion should be larger than B ion. For the stable perovskite crystal structure, the TF is 0.8~1.0. When TF is between 1 and 0.89, the cubic crystal structure (α phase) may form. In addition, TF less than 0.89 results in lower-symmetry orthorhombic (γ phase) or tetragonal (β phase) crystal structures. For example, $CH_3NH_3PbI_3$, the radius of $CH_3NH_3^+$, Pb^{2+} and I^- is 180 pm, 119 pm and 220 pm, respectively. The composition of perovskite materials and annealing temperature determine the actual crystal symmetry. For example, the calculated TF of $CH_3NH_3PbI_3$ is 0.834, which the crystal structure of $CH_3NH_3PbI_3$ is tetragonal at room temperature and cubic in 330 K. While, if the TF is more than 1, the three-dimensional (3D) crystal structure will be undermined result in the two-dimensional (3D) layer structure. However, from density functional theory (DFT) calculations, as it is quite hard to satisfy the ideal condition TF = 1, the cubic structure is the most unstable and the orthorhombic structure is the most stable structure.

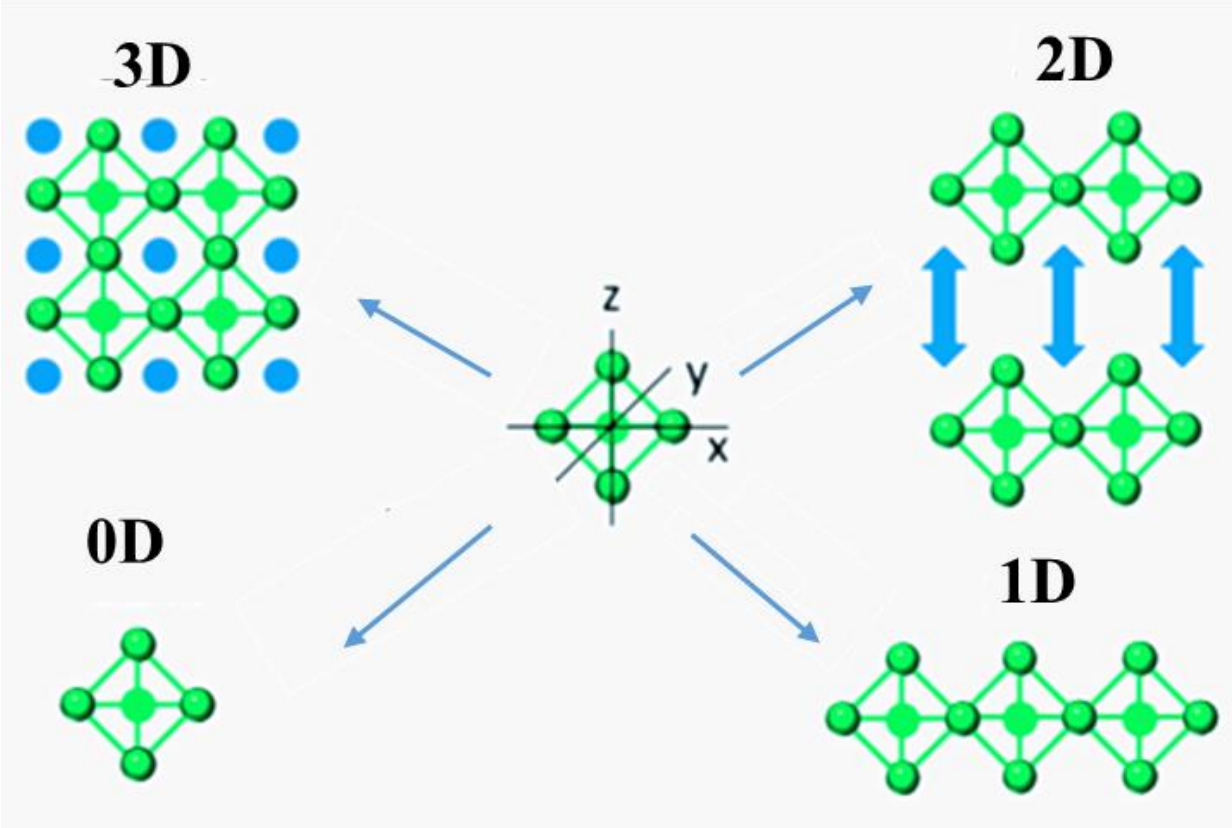

Figure 1.2 Schematic exhibitions showing the connectivity of BX_6 octahedra in different dimensional perovskites

In addition, the composition tunability and remarkable structural also are possessed by perovskites, which means that the basic building unit of perovskite, $[BX_6]^{4-}$, could be arranged in different path. The units can be connected in three-dimensional (3D), two-dimensional (2D), one-dimensional (1D), and zero-dimensional (0D) crystal structures, shown in Figure 1.2. Perovskites with the ABX_3 formula are classified as 3D perovskites in which the $[BX_6]^{4-}$ octahedra are corner-shared with all three 4-fold octahedral axes. 2D perovskites with layered structure organized from octahedral that connected with two octahedral axes. Slicing along specific crystallographic planes of 3D perovskites, the 2D perovskites could be derived. The 1D perovskites can be derived from 2D perovskites by slicing perpendicular to the inorganic sheets, leaving octahedra remaining connected only

along one axis. Slicing of 1D perovskites to form no connected octahedra or octahedral based clusters, the 0D perovskites are obtained. Perovskites can also be formed by superposition of two or more categories, i.e. a superstructure of 3D and 2D is often called quasi-2D perovskites. It is important to mention that a cationic organic or inorganic sublattice is used to stabilize the framework in perovskites of all dimensionalities.

The devices of perovskite solar cells usually have a transparent conductive oxide (TCO) as the cathode, an electron transport layer, a perovskite absorbance layer, a hole transport layer and a metal anode. Although perovskite solar cells have been fabricated by different structural configurations, there are mainly three types of structures of perovskite solar cells, including mesoporous structure, planar p-i-n structure and planar inverted i-n-p structure, shown in Figure 1.3. The mesoporous structure of perovskite solar cells usually contains a mesoporous scaffold of TiO_2 (200 nm) filled with perovskite absorber and a thin compact TiO_2 layer (20-40 nm) on the TCO to avoid shunting losses. In the planar structure of perovskite solar cells, the two categories of regular (n-i-p) and inverted (p-i-n) are divided by which selective contact is used on the surface of the TCO. Perovskite solar cells based on planar structure also can achieve high power conversion efficiency as well as mesoporous perovskite devices.

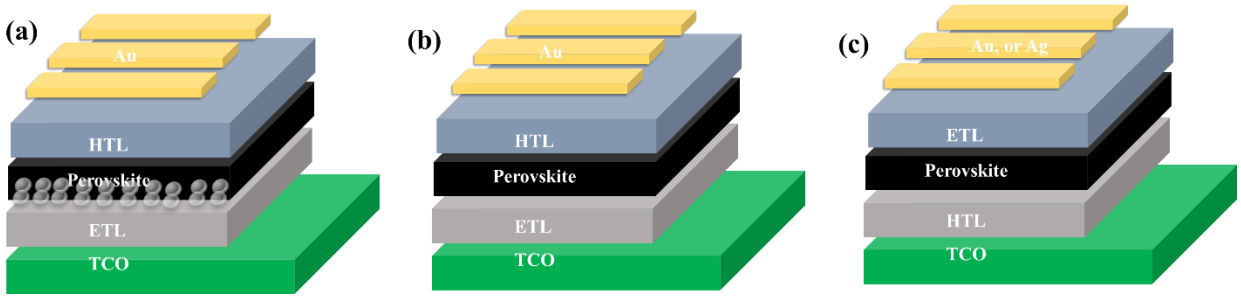

Figure 1.3 Three typical device structures of perovskite solar cells: (a) mesoporous, (b) regular planar structure, and (c) inverted planar structure.

1.3 Working principle

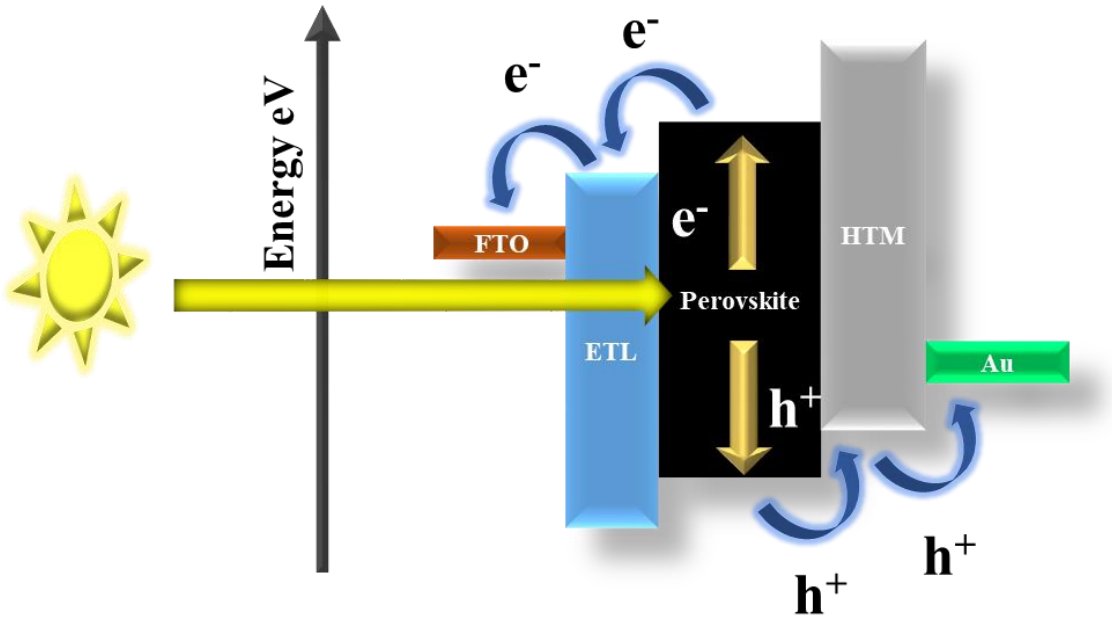

Figure 1.4 Schematic exhibitions of working principle of perovskite solar cells.

The working principle of the perovskite solar cells is exhibited in Figure 1.4. When sun light is applied on the perovskite absorbance layer, the photos are absorbed generating electron-hole pairs. The electrons will move to the conduction band then diffuse into the compact electron transport layer (ETL) and FTO. At the same time, the holes will move to valence band then will be absorbed by the hole transport layer (HTL) and Au. The typical ETL materials can be inorganic oxides, like TiO_2, SnO_2 and ZnO, or organic compound, i. e. [6,6]-Phenyl C61 butyric acid methyl ester ($PC_{61}BM$), Fullerene-C60. . The typical ETL materials can be inorganic compound, like CuSCN, CuI, NiO_2 and MoO_3, or organic compound, i. e. poly(3,4-ethylenedioxythiophene) polystyrene sulfonate (PEDOT/PSS), Poly(3-hexylthiophene-2,5-diyl) (P3HT), poly(triaryl amine) (PTAA) and

$N^2,N^2,N^{2'},N^{2'},N^7,N^7,N^{7'},N^{7'}$-octakis(4-methoxyphenyl)-9,9′-spirobi[9H-fluorene]-2,2′,7,7′-tetramine (Spiro-OMeTAD).

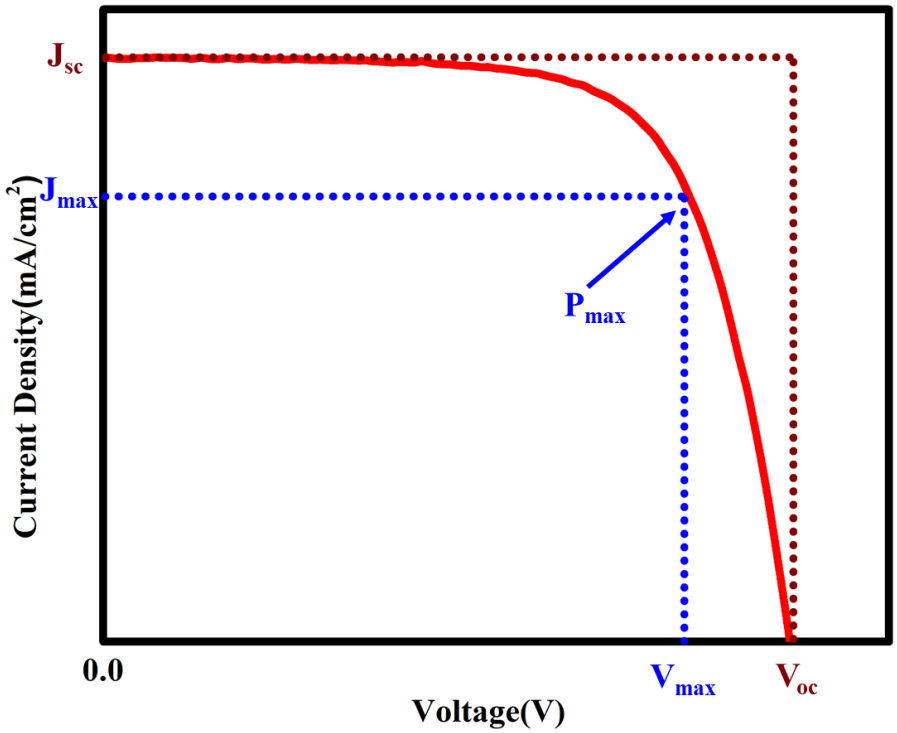

Figure 1.5 Schematic exhibitions of J-V curve.

The basic performance parameters of perovskite solar cells are open-circuit voltage (V_{OC}), short-circuit current (J_{SC}), fill factor (FF), power conversion efficiency (PCE) and external quantum efficiency (EQE). The V_{OC}, J_{SC}, FF and PCE can be obtained from current–voltage (J–V) curve, shown in Figure 1.5. The V_{OC} is the maximum voltage available from a solar cell, and this occurs at zero current, which corresponding to the amount of forward bias on the solar cell due to the bias of the solar cell junction with the light-generated current. The band gap of the perovskite materials and the interface between different layers determine the V_{OC} of perovskite solar cells. The J_{SC} is the current through the solar cell when the voltage

across the solar cell is zero. The J_{SC} is due to the generation and collection of light-generated carriers. The bandgap of perovskite materials and the thickness of perovskite layer determine the J_{sc} of perovskite solar cells. The FF is defined as the ratio of the maximum power from the solar cell to the product of V_{OC} and J_{SC}, which determined by the interface connection and quality of perovskite layers. The EQE is the ratio of extracted free charge carriers to incident photons. This ratio is obtained by measuring the photocurrent spectrum of the photovoltaic device under test and comparing it to the photocurrent spectrum of a calibrated reference photodetector, thereby removing the spectral characteristics of the test system.

1.4 Challenges and opportunities

Organometallic halide perovskite solar cells (PSCs) have attracted considerable attention around the world owing to the high absorption coefficient, ambipolar charge transport, long diffusion length, and high mobility of both electrons and holes.[2-3, 5, 11-13] The efficiency of solid-state PSCs has increased from 3.8 % in 2009 to 23.3 % so far, which is much higher than other third-generation solar cells.[10, 14] Although lots papers have been published, claiming the improvement of the increase of PSCs performances, the stability of perovskite devices still is the main issue for the commercializing applications. The stability of the organic-inorganic perovskite materials is the key point for the perovskite devices as those lead perovskites can degrade easily in the ambient air. Thus, it is significantly challenging and important to prepare high-quality perovskite films in humid ambient air. Another main issue is toxicity of lead, while lead is good in photovoltaic modules. It is desirable to find alternatives with comparable photovoltaic performance of lead.

1.5 Purpose and innovation of this thesis

In order to prepare high-quality perovskite films in humid ambient air atmosphere. Five reformations we have tried in the antisolvent assisted one-step spin coating process. Firstly, the research on different acetate based antisolvent was compared for preparing high-quality

$CH_3NH_3PbI_3$ perovskite film in the ambient air condition. Secondly, we tried using alcohols as the additive into diethyl ether antisolvent for the enhanced crystallization of $CH_3NH_3PbI_3$ perovskite film in humid atmosphere. Thirdly, we tried using magnesium (II) iodide as a dopant into $CH_3NH_3PbI_3$ perovskite layer for enhanced crystallinity and stability. Fourthly, we tried using a pyrene core based organic, 1-(ammonium acetyl) pyrene for the 2D materials into $CH_3NH_3PbI_3$ perovskite layer for the 2D/3D heterostructure in humid atmosphere. Lastly, a novel all-inorganic perovskite, $CsPb_{1-x}Ge_xI_2Br$, was prepared in the humid air condition.

Chapter 2. Fabrication of high humidity fabrication of $MAPbI_3$ perovskite devices in ambient atmosphere by acetate based anti-solvent

2.1 Introduction

Besides remarkable photovoltaic performance of perovskite solar cells, the easy and cheap solution-based fabrication process also could lower the fabrication cost and promote their wide commercialization around the world.[15-17] One of key points for preparing high-performance PSCs is to control the morphology and crystal structure of perovskite materials. Numerous techniques for preparing the perovskite films have been reported, such as one-step spin-coating, sequential deposition, thermal evaporation and vapor processing of components.[18-21] One-step spin-coating method is widely used for fabricating the perovskite layer, as the method is simple to control. However, the films always have incomplete surface coverage and poor morphology, which results in charge recombination in solar cells. To address this issue, anti-solvent washing method has been developed using solvents such as chlorobenzene, toluene, or diethyl ether during spin-coating process of perovskite films. A mixture of N,N-dimethylformamide (DMF) and dimethyl sulfoxide (DMSO) is well known polar solvents for the preparation of perovskite precursor solution. The function of the anti-solvent is to remove the high boiling point solvent DMF and form a transparent intermediate adduct (CH_3NH_3I-PbI_2-DMSO) from its perovskite precursor solution, which leads to a smooth, pinhole free and homogenous perovskite film with high electronic properties.[22]

Despite the high efficiency of PSCs, the perovskite layer is very sensitive to moisture and easily degrades in high humidity either during fabrication process or device measurement.[23-25] To solve this problem, most researchers prepared PSCs inside

nitrogen/argon filled glovebox to avoid water, which increases the solar cells manufacturing cost. Therefore, research in the area of fabricating perovskite films in ambient air is desirable. Yan and co-workers reported use of lead (II) thiocyanate ($Pb(SCN)_2$) precursor for fabricating $CH_3NH_3PbI_{3-x}(SCN)_x$ PSCs in more than 70 % humidity showing efficiency up to 15 %.[26] With the assistance of hydrochloric acid, Zhao and co-workers prepared high-quality $CH_3NH_3PbI_3$ perovskite films in ~60 % humidity.[27] Recently, Watson and co-workers used ethyl acetate as an anti-solvent during one-step deposition; where they suggested that ethyl acetate acted as a moisture absorber protecting sensitive perovskite intermediate phases from water molecules during film formation and annealing.[28] However, there are still quite few reports on one-step deposition of perovskite film in the high humidity ambient air condition.

In this chapter, four different acetate-based solvents (methyl acetate (MA), ethyl acetate (EA), propyl acetate (PA), butyl acetate (BA)) were used as the anti-solvent for preparing high-quality $CH_3NH_3PbI_3$ perovskite film in high humidity (60-70 % RH) air condition. It was explored that MA could give a high-quality perovskite film with more homogeneous morphology than other three kinds of acetate anti-solvents. Upon optimization, the best solar cell by MA washing exhibited a stabilized PCE of 16.3% with low hysteresis. Moreover, the PCE still kept at 15.6 % even though 2 v% deionized water was added in the MA for preparing the perovskite layer. We believe that this study would give a good direction for PSCs fabrication in humid climate and uncontrolled laboratories, potentially enabling the commercialization of devices.

2.2 Experimental section

2.2.1 Preparation of perovskite solar cells

All reagents were directly used without further purification, if not specified. F-doped SnO_2 layered glass (FTO glass, Nippon Sheet Glass Co. Ltd) glass was first patterned and cleaned by using Zinc powder and 6 N hydrochloric acid solution. Tin (II) chloride (Aldrich, 98%) was dissolved in anhydrous ethanol (Wako, 99.8%) to form a 0.1 M $SnCl_2$ concentration solution. Then the $SnCl_2$ solution was spun on the FTO glass at 2000 rpm for 30 seconds. The substrate was heated at 100 °C for 5 minutes and then annealed at 180 °C for 60 minutes on a hot plate to get a compact SnO_2 electron transport layer.[29] 1.5 M $CH_3NH_3PbI_3$ in anhydrous dimethylformamide (DMF, Aldrich, 99.8%) and anhydrous dimethyl sulfoxide (DMSO, Aldrich, 99.8) solution (DMF: DMSO, 4:1) were prepared by mixing equal molar ratio of CH_3NH_3I (TCI, 98%) and PbI_2 (TCI, 99.99%) and stirred at room temperature for more than 1 hour. The perovskite precursor solution was spun on the substrate at 4000 rpm for 25 seconds and 10 seconds after starting the spin-coating process, 0.5 mL of the anti-solvent was slowly dropped onto the film. After that, the immediate perovskite phase was heated at 65 °C for 1 minute and 100 °C for 10 minutes. The spiro-MeOTAD layer was prepared by spin coating a chlorobenzene solution containing 180 mM spiro-MeOTAD (Aldrich, 99 %), 60 mM tert-butylpyridine (Aldrich, 96 %), 30 mM Li-TFSI (Aldrich, 99.95 %) (520 mg/mL in acetonitrile) and 33 mM FK209 (Aldrich, 99 %) (300 mg/mL in acetonitrile) at 4000 rpm for 30 seconds. Finally, a 80 nm thickness Au counter electrode was deposited by thermal evaporation. All procedures were performed in 60-70 % relative humidity ambient air condition, Relative humidity was recorded using a hygrometer

accurate to ± 5% RH between 25 % and 69.9 % RH, ±10 % RH between 70 % and 90.0 % RH) (A&D Company, AD-5681).

2.2.2 Characterization

Solar cell performances were evaluated using a solar simulator (CEP-2000SRR, Bunkoukeiki Inc., AM 1.5G 100 mWcm-2) and a black mask on top of the devices with an exposure area 0.10 cm^2 was used during the photovoltaic measurements. The current-voltage (J-V) curves of these solar cells were measured with a 0.01V/s scanning rate in reverse (from the open-circuit voltage (V_{oc}) to the short-current density (J_{sc})) and forward (from J_{sc} to V_{oc}) modes under standard global AM 1.5 illumination. X-ray Diffraction (XRD) Study. X-ray diffraction analyses (RINT-Ultima III, Rigaku, Japan) were performed in the range 3°−80°. The surface morphology of the samples were observed through a scanning electron microscope (SEM) (JEOL, Neoscope, JCM-6000) and a Bruker Innova atomic force microscopy (AFM) (JSPM-5200). Attenuated Total Reflectance Fourier transform IR spectras (FT-IR) were tested by FT-IR spectrometer (JASCO, FT/IR-4100 Series) via an attenuated total reflectance (ATR) crystal.

2.3 Result and discussions

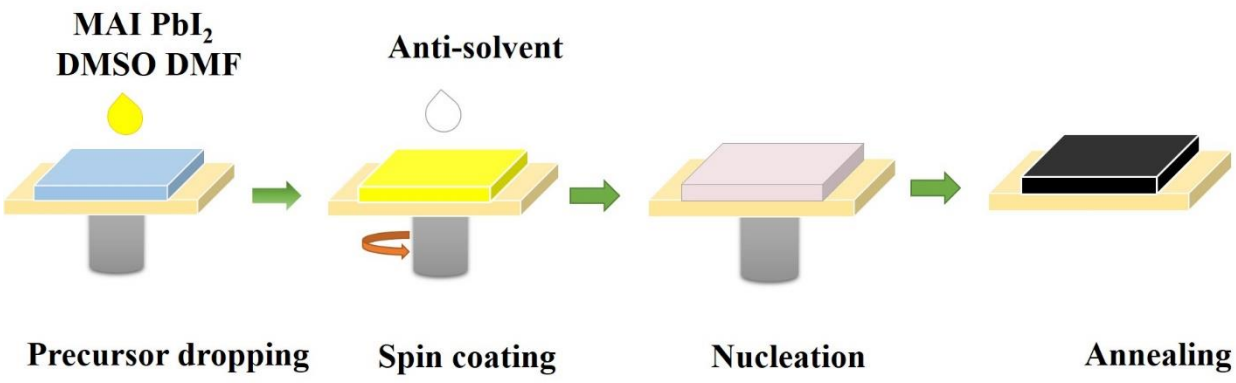

Figure 2.1 Schematic illustration of the one-step process using anti-solvent for fabricating perovskite films.

In the anti-solvent based one-step preparation process, the perovskite layer is formed by spin coating of the precursor solution followed by the thermal annealing. This preparation process usually has two stages, which shown in Figure 2.1. In the first stage, the liquid film is thinning by the centrifugal forces. After a transition point, evaporation rate of the solvent dominates the film thinning, which depends on the vapor pressure of the solvent. Then at the second stage, solution becomes supersaturated, nucleation happens and growths, solid intermediate (or perovskite) film forms. Thus, in order to prepare high-quality perovskite film, the important stage is to accelerate the evaporation rate of excess DMF and control the perovskite crystallization process.[30] For two immiscible solvents, the total vapor pressure of the mixed solution is close to the plus of the two solvents' vapor pressures, and the boiling point of the mixture should be lower than each solvent.[31] Follow this rule, introducing the high vapor pressure anti-solvent for one-step preparing perovskite film will help promote a uniform and high-quality film.

As perovskite layer is sensitive to moisture within the air during spin coating. Watson and co-workers proposed that when using EA as the anti-solvent in one-step deposition,

moisture in the air is preferred in solution with the anti-solvent rather than reacting with the perovskite intermediate phase.[28] So one way to solve this problem is to introduce more water-soluble anti-solvent to avoid the water absorption of the perovskite intermediate phase during the spin coating process. In addition, after the perovskite intermediate phase formed, it is better to reduce contacting time of this intermediate phase with the moisture within the air to avoid the water affection. Therefore, the second way is to speed up the perovskite forming procession to reduce the formation time of perovskite intermediate phase to perovskite. So from the above discussions, we assume that using the solvent which has high vapor pressure and more water solubility as the anti-solvent in one step spin-coating progression will be great helpful to fabricate a high-quality perovskite film.

Table 2.1 Physical properties (vapor pressure, boiling point, solubility in water) of solvents.

Solvent	Vapor pressure at 25 °C (Kpa)	Boiling point (°C)	Solubility in H_2O (g/100 mL)
MA	28.8	56.9	24.4
EA	12.4	77.1	8
PA	4.8	101.5	1.6
BA	1.1	126.1	0.68

Physical properties (vapor pressure, boiling point and water solubility) of the four acetate-based solvents were illustrated in Table 2.1. Among those four acetates, MA had the relative highest vapor pressure (28.8 Kpa), lowest boiling point (56.9 °C) and best water solubility. The high vapor pressure and low boiling point would accelerate the evaporation rate of excess DMF and control the perovskite crystallization process. Moreover, the more water solubility of the anti-solvent could decrease the moisture affection of the perovskite intermediate phase during the spin coating process. Hence, it could be noticed that perovskite

fabrication by MA treatment would give a high-quality perovskite film with more homogeneously morphology than other three acetates (EA, PA, BA).

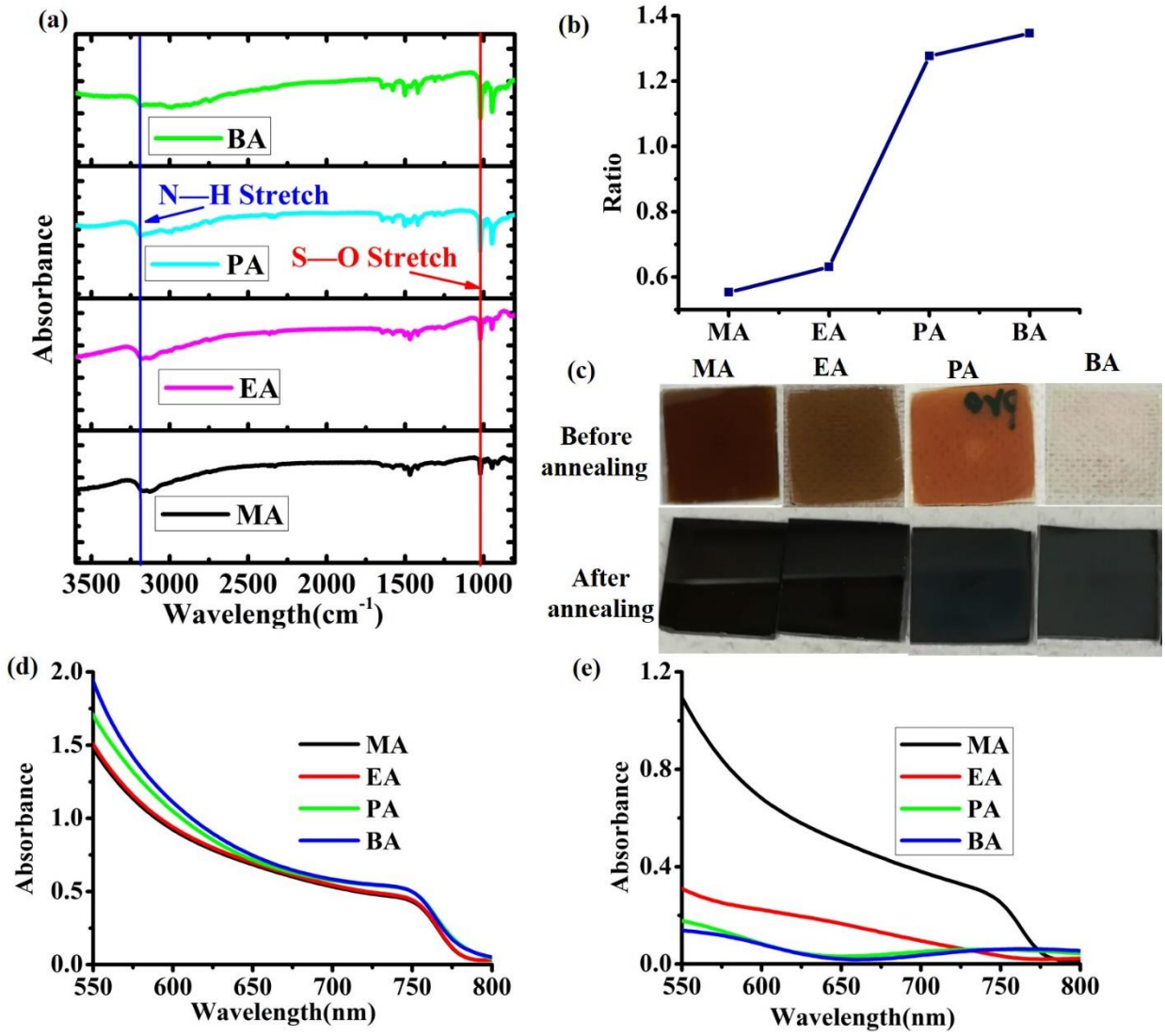

Figure 2.2. (a) Attenuated Total Reflectance Fourier transform IR spectra of $CH_3NH_3PbI_3$ films (on Pt/glass substrates) prepared by MA, EA, PA and BA without annealing. (b) Ratio of intensity of absorbance at 1050 cm^{-1} and 3190 cm^{-1} (1050 cm^{-1} : 3190 cm^{-1}). (c) The perovskite film on FTO/compact SnO_2 after spinning by different anti-solvents before and

after annealing. (d) UV-vis absorption spectra of perovskite films prepared with by different solvents without annealing and (e) with annealing.

Figure 2.2a showed FT-IR spectra of $CH_3NH_3PbI_3$ film prepared with different anti-solvents (MA, EA, PA and BA) without annealing. The non-annealing films showed similar absorbance peak positions. All the films showed N-H vibration peaks at 3200 cm^{-1} and at approximately 1470 cm^{-1} attributed to CH_3NH_3I, and S-O stretching at 1020 cm^{-1} attributed to DMSO.[32] By taking the ratio (absorbance at 1020 cm^{-1} to the absorbance at 3200 cm^{-1}), the concentration of DMSO in the intermediate phase can be deduced. From this ratio, it was found that the DMSO content decreased form MA to BA, as shown in the Figure 2.2b. The less DMSO ratio mean the few intermediate phase of CH_3NH_3I-PbI_2-$DMSO_x$, which indicated the speeding up of perovskite formation process.[33] Figure 2.2c showed the fresh perovskite film by different anti-solvents with or without annealing. The color of the annealing-free film gradually changed from dark brown (MA) to transparent (BA), which meant increased DMSO content in the intermediate phase films.[34] This result was in agreement with the FT-IR spectra. Furthermore, the annealed films exhibited decreased glossiness of the perovskite films from MA to BA, which indicated that the $CH_3NH_3PbI_3$ perovskite films became more inhomogeneous. Ahn et al. reported that the DMSO intermediate phase was unfavorable due to the gradual vaporization of DMSO from the surface of the spin-coated film, which led to an inhomogeneous $CH_3NH_3PbI_3$ film.[22] Figure 2.2d and 2.2e showed the absorption spectra of perovskite films prepared by different anti-solvents treatment before and after annealing. The UV-vis absorption spectrum of a freshly perovskite film prepared by MA treatment was almost close to that of the annealed film, indicating that the using of MA resulted in nearly complete $CH_3NH_3PbI_3$ crystallization at

room temperature. Therefore, from the above results, we concluded that a large amount of redundant DMSO in the annealing-free perovskite layers might be harmful for the performance of PSCs when preparing perovskite in high humidity air condition.

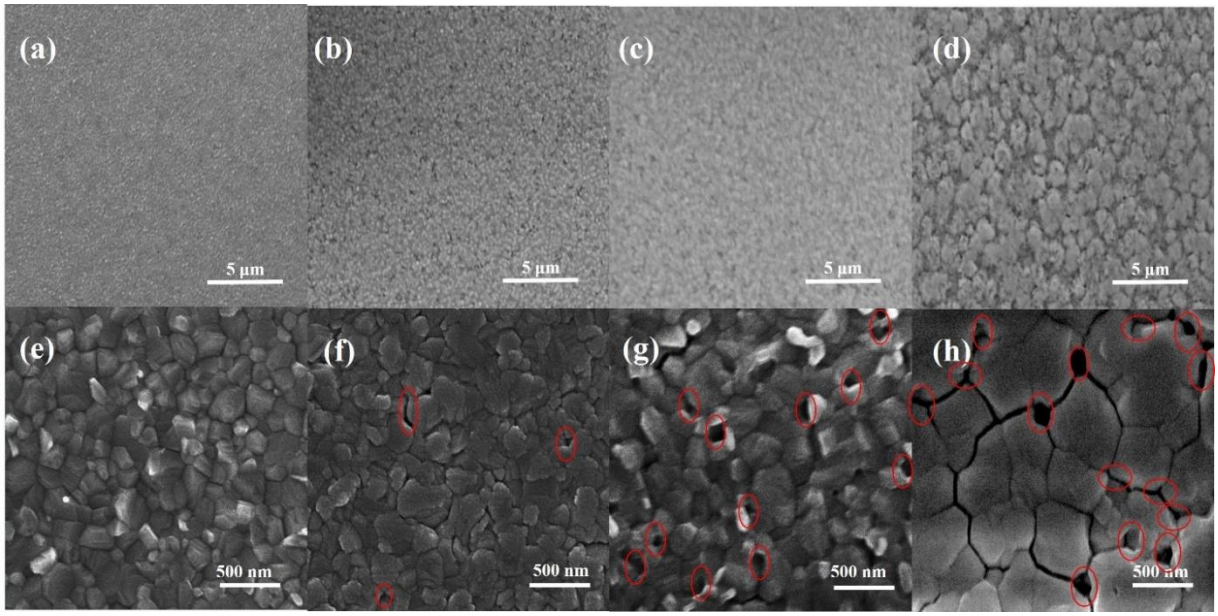

Figure 2.3. The scanning electron microscopy of annealed $CH_3NH_3PbI_3$ films of FTO/Compact SnO_2 by different anti-solvents. (a), (e) MA; (b) (f) EA; (c) (g) PA; (d) (h) BA.

Figure 2.3 showed the surface morphology of the annealed $CH_3NH_3PbI_3$ perovskite films based on different anti-solvents by scanning electron microscopy (SEM). The perovskite film prepared by MA treatment showed extremely dense, homogeneous and almost no pinholes, which shown in Figure 2.3a and 2.3e. However, with EA treatment, the perovskite film became slightly inhomogeneous and the presence of pinholes could be observed in Figure 2.3b and 2.3f. Especially in the case of BA, the presence of pinholes was very prominent (Figure 2.3d and 2.3h). This result was consistent with the image in Figure 2.2c where the film appeared the least luminous. Moreover, the grain size of the $CH_3NH_3PbI_3$ perovskite

gradually increased, which maybe owning to the increase of DMSO content in the intermediate perovskite phase.[17]

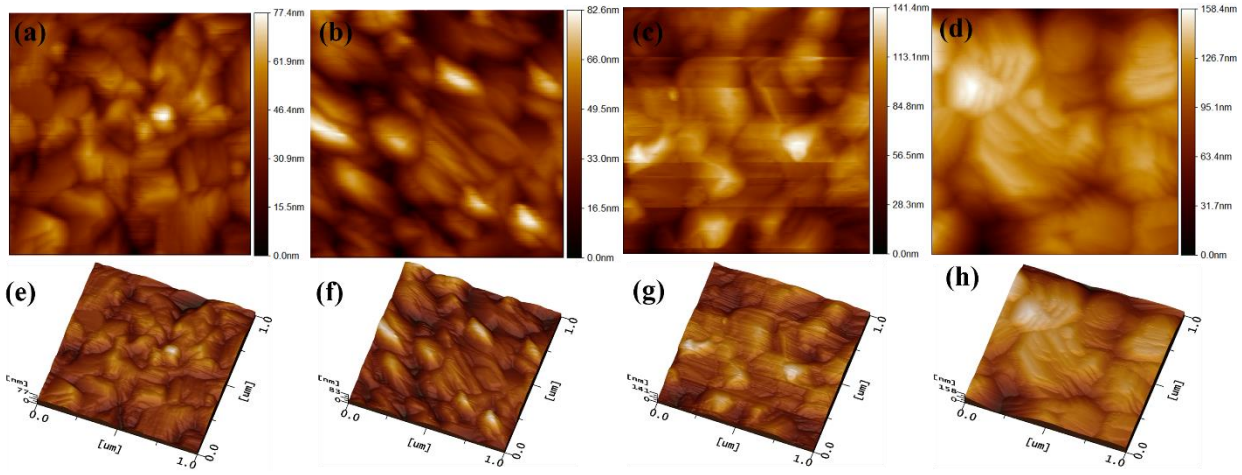

Figure 2.4. Atomic force microscopy (AFM) height (a, b, c, d) and 3D surface plot images (e, f, g, h) of the perovskites film on FTO/SnO_2 prepared by MA (a, e) or EA (b, f), PA (c, g) and BA (d, h) treatment processes. The scanning range of the images is 1 μm×1 μm.

Atomic force microscopy (AFM) was employed to study the surface morphology perovskite films prepared by different anti-solvents, as shown in Figure 2.4. The annealing time was fixed at 10 min. It was found that the grain sizes of perovskite samples were graduate increased by the treatment way from MA, EA, PA, to BA, which was in consistence with Figure 2.3. The Rq roughness values were measured to be 10.2, 13.8, 22.7 and 25.8 nm for samples prepared by MA, EA, PA and BA, respectively. The roughness value was smallest for perovskite film prepared by MA treatment, and increased from MA, EA, PA to BA, which is in accordance with the Figure 2.3a-d. The 3D surface plot images shown in Figure 2.4e-h could clearly show the increase of the surface roughness for perovskite films. This surface topography indicated that perovskite films prepared by MA had better coverage

on the top of perovskite film, resulting in larger parallel resistance and lower serial resistance, as evidenced by the improved diode characteristics.

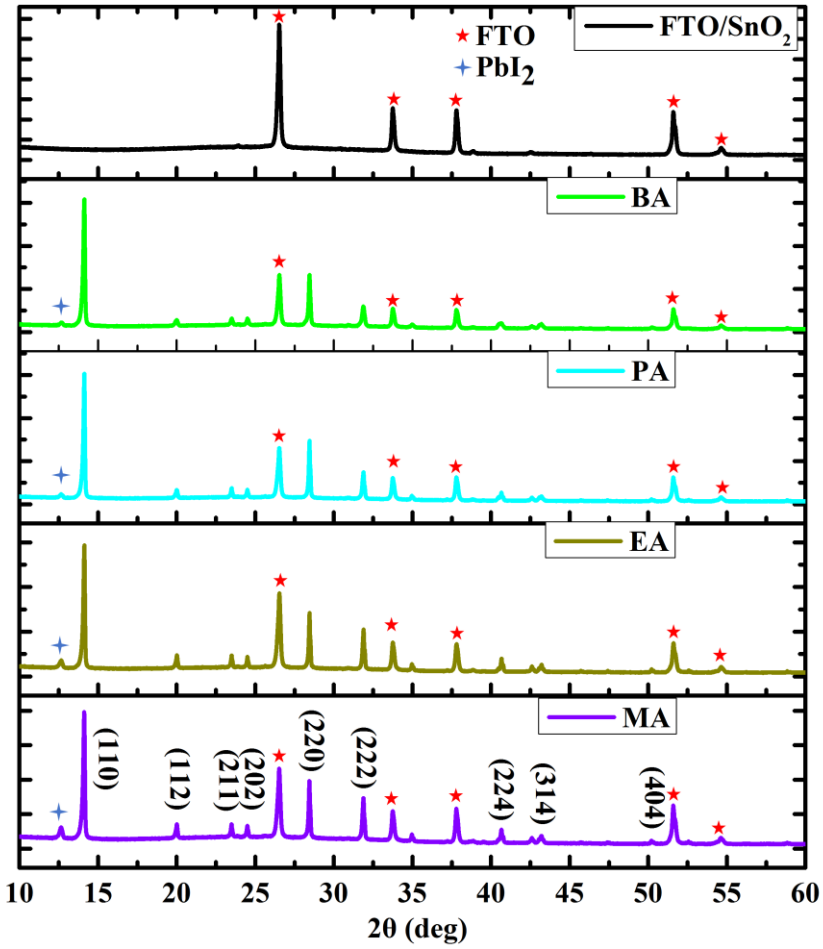

Figure 2.5. X-ray diffraction (XRD) of $CH_3NH_3PbI_3$ films on FTO/compact SnO_2 substrates prepared by different anti-solvents.

Figure 2.5 shows the X-ray diffraction (XRD) patterns of $CH_3NH_3PbI_3$ layer on FTO/SnO_2 substrate with different anti-solvents. Peaks from the substrates were indicated by triangles. Strong diffraction peaks located at 14.1°, 20.0°, 23.5°, 24.5°, 28.4°, 31.9°, 40.7°, 43.1° and 50.2° for 2θ scan were observed corresponding to the planes of (110), (112), (211),

(202), (220), (222), (224), (314) and (404), which were in good agreement with the previous reports.[21, 35-36] The result confirmed the films are highly crystallized perovskite phase.[37-38] Meanwhile, a weak diffraction pattern of PbI_2 appeared at 12.7°, where the intensity of the peak decreases upon changing the anti-solvent from MA to BA. This decrease of PbI_2 content in perovskite film could be ascribed to the different solubility of PbI_2 and CH_3NH_3I compounds in various anti-solvents.[39] Although there were many discussions about the function of residual PbI_2, it was hard to tell the exact impact of such little remaining PbI_2 on this anti-solvent process for perovskite formation.

To show the reproducibility of devices efficiency, the PCEs of 20 planar perovskite solar cells prepared by different anti-solvents were measured. High efficiency PSCs generally uses titanium oxide (TiO_2) as an electron transport layer; however, some drawbacks such as UV light instability because of the photocatalytic activity hinder reproducibility over the time. Tin-oxide (SnO_2) as an alternative to TiO_2, has been reported to exhibit better electron mobility and stability. In addition, a higher band gap with deep valence band maximum is supposed to effectively block the photo-generated holes from the absorber layer to recombine with the electrons in conducting oxide layer (TCO). Therefore, a planar PSC structure employing SnO_2 was chosen for preparing high-quality $CH_3NH_3PbI_3$ perovskite films in high humidity (60-70% RH). Figure 2.6a and 2.6b exhibited schematic structure and energy diagram of the PSCs. The current density-voltage (J-V) performance data were shown in Figure 2.6c-f, and Table 2.2 summarized the photovoltaic parameters of the solar cells. There was a clear decreasing trend of all the parameters of PSCs (V_{oc}, J_{sc}, FF, PCE) among the four anti-solvents treatments, because of the inhomogeneous perovskite layer.[40-42] We could see from Figure 2.6c-f that an average V_{oc} of 1.04±0.02 V, J_{sc} of 21.78±0.45 mA/cm^2, FF of

68.9±1.42 %, and PCE of 15.6±0.7 % were obtained for devices fabricated using MA treatment. The champion device of MA treatment perovskite devices had a V_{oc} of 1.05 V, a J_{sc} of 22.21 mA/cm^2, a FF of 70.0 % and an efficiency of 16.3 %. Such high efficiency could be attributed to the reproducible and uniform growth of $CH_3NH_3PbI_3$ layer obtained by anti-solvent deposition process.

Table 1.2. Devices performance data of FTO/c-SnO_2/$CH_3NH_3PbI_3$/Spiro-OMeTAD/Au by different anti-solvents.

Solvent	Classification	V_{oc} (V)	J_{sc} (mA/cm^2)	FF (%)	PCE (%)
Methyl acetate	Champion [a]	1.05	22.21	70.0	16.3
	Average [b]	1.04±0.02	21.78±0.45	68.9±1.42	15.6±0.7
Ethyl acetate	Champion	1.04	21.71	66.9	15.1
	Average	1.02±0.03	21.44±0.82	64.6±3.89	14.2±1.1
Propyl acetate	Champion	0.97	20.67	66.8	13.4
	Average	0.95±0.05	20.30±0.75	62.9±5.60	12.2±1.0
Butyl acetete	Champion	0.96	19.97	66.5	12.7
	Average	0.94±0.04	20.26±0.34	60.4±2.61	11.4±0.7

a, the best performance of PSCs. b, the average performance of 20 PSCs.

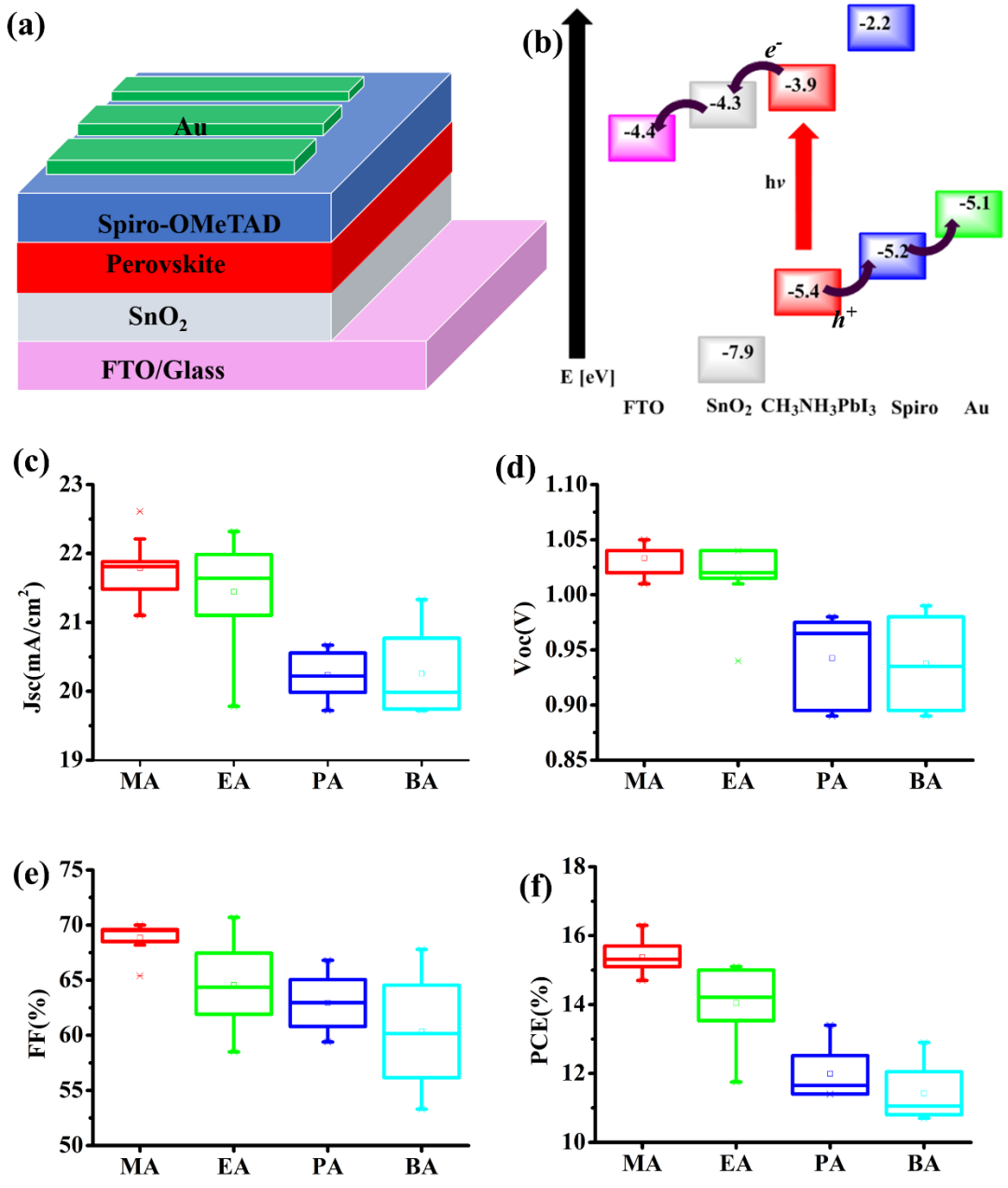

Figure 2.6. Schematic structure (a) and (b) energy diagram of the planar FTO/c-SnO2/ $CH_3NH_3PbI_3$/Spiro-OMeTAD/Au planar perovskite solar cells. Photovoltaic statistics for the planar perovskite solar cells processed by anti-solvents. (c) Short-circuit current, (d) Open circuit voltage, (e) Fill factor, (f) Efficiency. The boxes represent 80 data from the V_{oc}-to-J_{sc} scan direction.

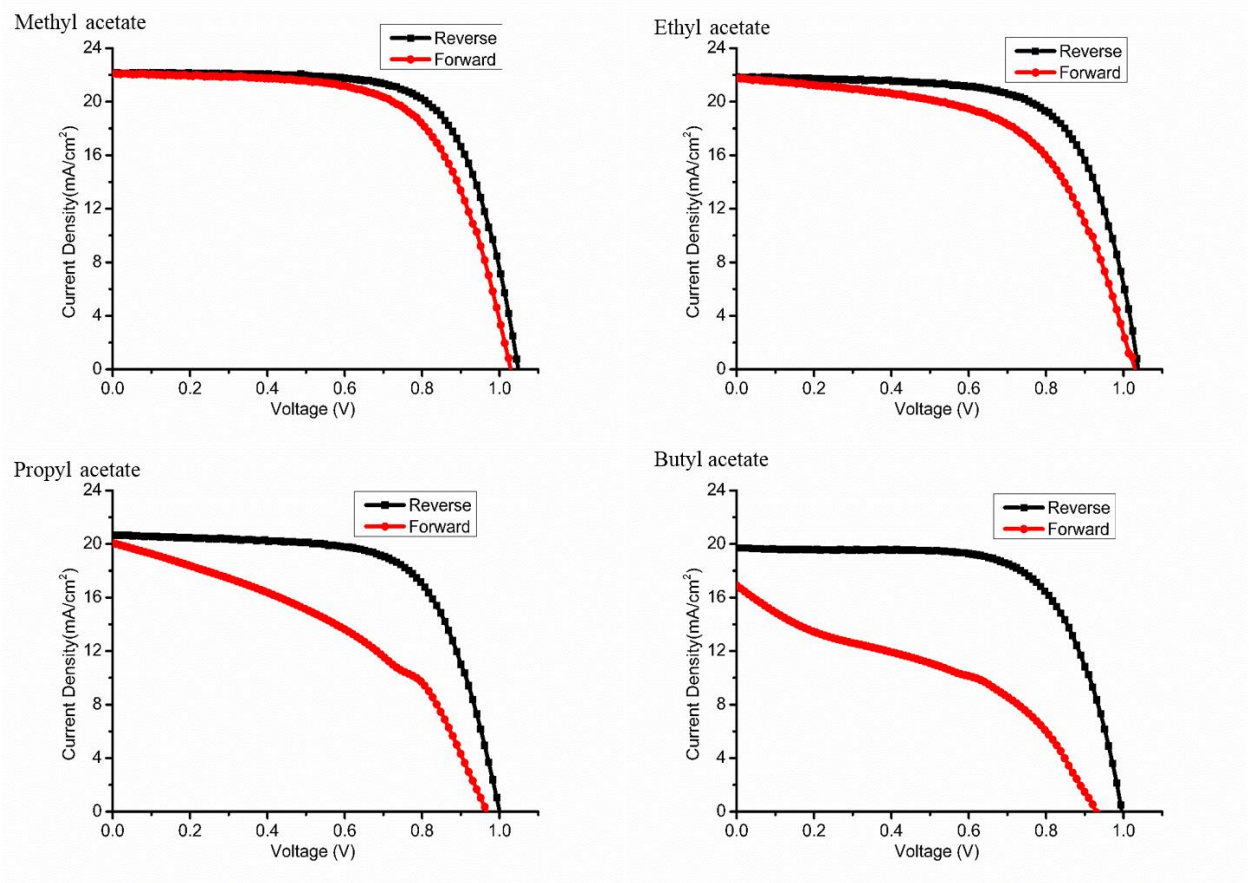

Figure 2.7 J-V curves of the best-performing perovskite $CH_3NH_3PbI_3$-based solar cell under reverse and forward voltage scans.

The performance of EA treated perovskite film was marginally lower than MA with an average V_{oc} of 1.02±0.03 V, J_{sc} of 21.44±0.82 mA/cm^2, FF of 64.6±3.89 %, and PCE of 14.2±1.1 %. However, the performances with PA and BA treatments decreased significantly, with an average V_{oc} of 0.95±0.05 V, J_{sc} of 20.30±0.75 mA/cm^2, FF of 62.9±5.60 %, PCE of 12.2±1.0 %, and V_{oc} of 0.94±0.04 V, J_{sc} of 20.26±0.34 mA/cm^2, FF of 60.4±2.61 %, PCE of 11.4±0.7 %, respectively. Figure 2.7 demonstrated the J-V curve of reverse direction and forward direction. Figure 2.8 showed the J-V curves and the corresponding IPCE for the PSCs. The calculated J_{sc} from the IPCE agreed well with the measured J_{sc}. Importantly, intended to quantitatively compare the hysteresis effect across diverse samples, a modified

hysteresis index (HI) values were calculated from the J-V curves, shown in Figure 2.8a.[43] The hysteresis of the solar cell performance indicated an approximate increasing trend, which was demonstrated by the HI values of MA (HI, 0.10), EA (0.21), PA (0.40) and PA (0.56).

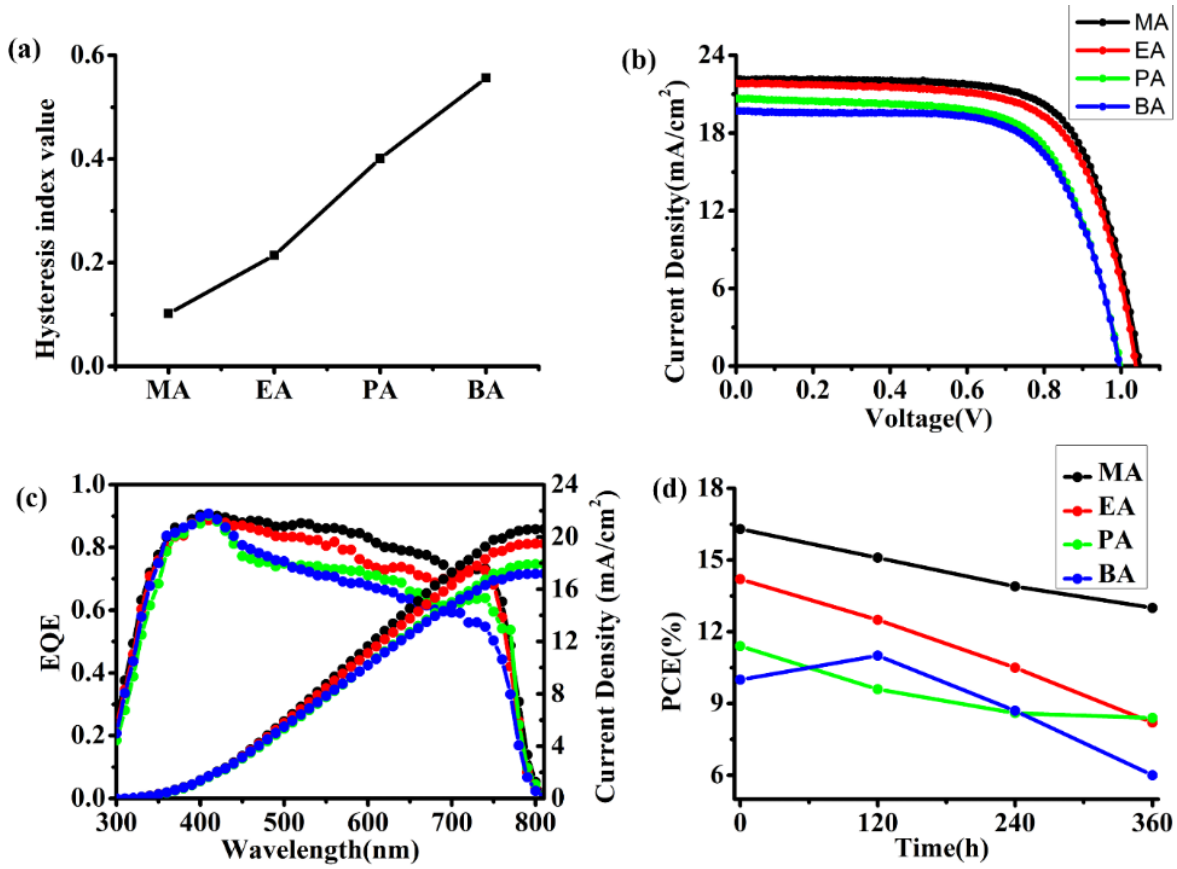

Figure 2.8. (a) Hysteresis index value calculated from the J-V curve of four acetate based champion devices. J-V (b) and the correspondent IPCE (c) curves of different anti-solvents based planar FTO/c-SnO_2/$CH_3NH_3PbI_3$/Spiro-OMeTAD/Au champion devices. (d) Stability test for 360 h of the different anti-solvents based planar FTO/c-SnO_2/$MAPbI_3$/Spiro-OMeTAD/Au devices under ambient atmosphere without sealing, and the average humidity is about 60% RH.

Furthermore, the indoor environment stability of the different anti-solvents processed devices were investigated as shown in Figure 2.8d. The perovskite devices were stored at ambient room temperature and under controlled humidity about 60-70% RH without sealing. After 360 h, the PCE of the perovskite devices prepared by MA treatment still retain over 80% of its original efficiency, while the PCE of perovskite devices prepared by the other three acetates decreased to less than 60% of the fresh devices. It is interesting to note that all the PSC devices` fabrication processes were accomplished in the 60-70% RH air condition. In addition, for comparison, the devices based on commonly used anti-solvents (diethyl ether, chlorobenzene, and toluene) were also prepared in the 60-70% RH air condition. However, all those devices showed poor performances compared to acetate-based solvents (Table 2.3). Hence, it is safe to assume that the MA treated devices are the most stable compared with other acetate solvents processed devices.

Table 2.3. Photovoltaic parameters derived from J-V measurements of FTO/c-SnO2/$CH_3NH_3PbI_3$/Spiro-OMeTAD/Au by different anti-solvents.

Materials	Voc (V)	Jsc (mA cm^{-2})	FF (%)	PCE (%)
Diethyl ether	0.60±0.03	16.02±1.98	53.0±6.5	5.1±1.8
Chlorobenzene	0.45±0.02	0.89±0.22	52.2±7.8	0.2±0.1
Toluene	0.39±0.02	0.81±0.32	57.6±7.2	0.2±0.1

Watson and co-workers claimed that when using EA as the anti-solvent in one-step deposition perovskite film, the moisture in air tend to mix with the anti-solvent rather than with the perovskite intermediate phase.[28] Therefore, we assumed high water solubility of the anti-solvent would be beneficial during the fabrication of PSCs. In order to prove this hypothesis, 2 v % deionized water was deliberately added to the anhydrous MA, EA, PA and

BA were used during the fabrication of PSCs. The current density-voltage (J-V) performance data were shown in Figure 2.9, and the resulting photovoltaic parameters of the solar cells were summarized in Table 2.4. In the case of MA, the addition of 2 v % deionized water had nearly no influence on devices performance with high efficiency of 15.6 % (average PCE, 14.8±0.5 %, kept at 94%). However, for the other three acetates, there was a significant decrease in the device performance from EA (average PCE, 9.9±1.7 %, kept at 69.5 %), PA (average PCE, 5.1±1.2 %, kept at 42.5 %) to BA (average PCE, 2.9±1.1 %, kept at 25.4 %). This could be attributed to the high solubility of water in MA which screens the perovskite film from getting dissipated by water molecules.

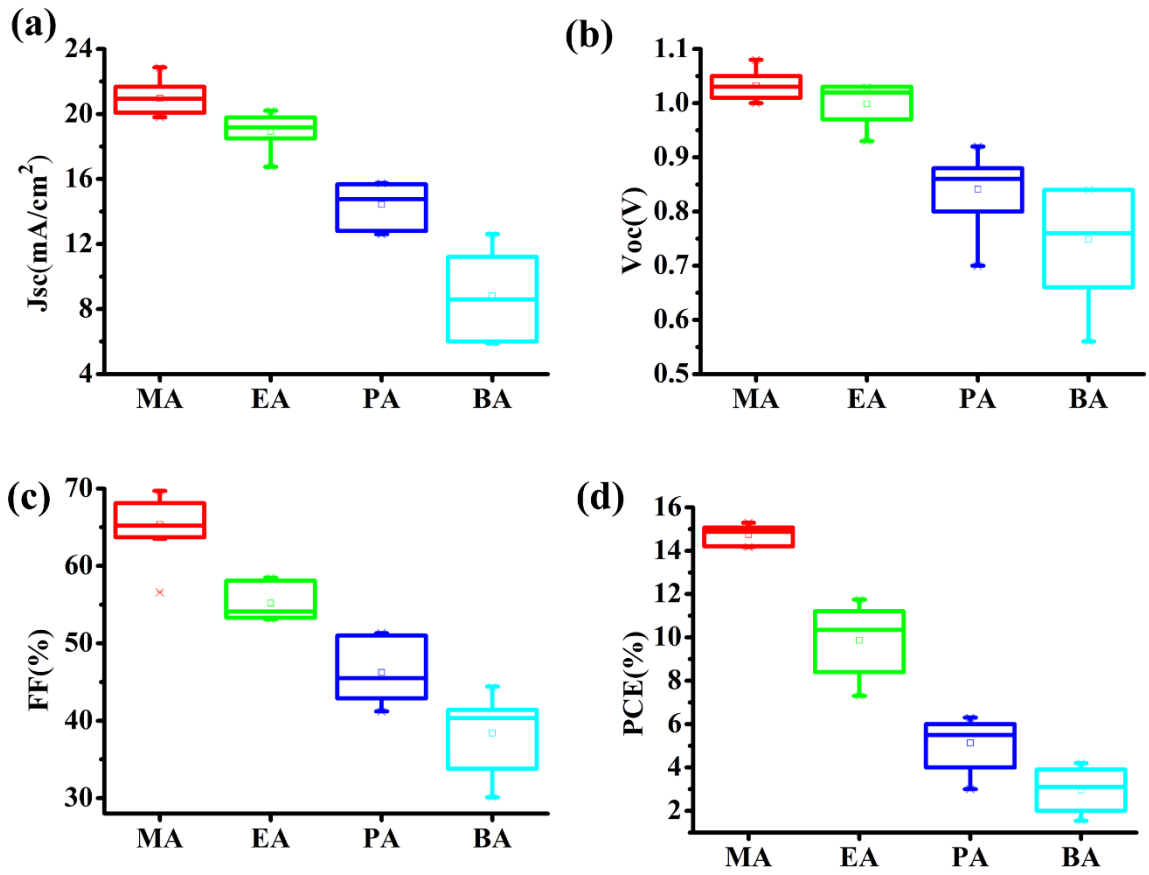

Figure 2.9. Photovoltaic statistics for FTO/c-SnO_2/$CH_3NH_3PbI_3$/Spiro-OMeTAD/Au planar perovskite solar cells processed by 2 v% deionized water added into anti-solvents. (a) Short-circuit current, (b) Open circuit voltage, (c) Fill factor, (d) Efficiency. The boxes represent 40 data from the V_{oc}-to-J_{sc} scan direction.

Table 2.4. Photovoltaic parameters derived from J-V measurements of FTO/c-SnO2/MAPbI3/Spiro-OMeTAD/Au by different contaminated with 2 v% deionized water anti-solvents.

Materials	Voc (V)	Jsc (mA cm^{-2})	FF (%)	PCE (%)
Methyl acetate	1.03±0.02	20.97±1.02	65.37±4.07	14.8±0.4
Ethyl acetate	0.99±0.03	18.93±1.24	55.25±2.46	9.9±1.7
Propyl acetate	0.84±0.07	14.43±1.26	46.23±4.15	5.1±1.2
Butyl acetate	0.74±0.10	8.81±2.95	38.40±50.34	2.9±1.1

2.4 Conclusion

In conclusion, four different acetate-based solvents (MA, EA, PA, BA) were used as anti-solvent for preparing the $CH_3NH_3PbI_3$ PSCs in high humidity ambient atmosphere (60%-70% RH). The highest solar cell efficiency was obtained with $CH_3NH_3PbI_3$ perovskite layer prepared by employing MA, showing the best PCE of 16.3% along with the improved photovoltaic parameters such as V_{oc} of 1.05 V, J_{sc} of 22.21 mA/cm^2, FF of 70.0%. Moreover, the performance decreases from using MA to BA. In addition, the stability test was performed which showed the superior performance of the MA based perovskite solar cell, reserving more than 80% of its original performance. The notable performance of the solar cell was attributed to the better film morphology of the perovskite film with condensed grains and no pinholes. The high water solubility of MA also meant that the perovskite layer was protected

from contact with water due to the water molecules tend to remain in MA as the PCE still kept at 15.6 % when 2 v% deionized water added in MA for preparing PSCs. All the experiments were accomplished without the requirement for stringent atmospheric control. This study would give a direction for PSC production at commercial level in robust environment, which could lower the cost and reduce the time for fabricating the high efficiency PSCs.

Chapter 3. Alcohols additive into anti-solvent for achieving high-quality $MAPbI_3$ perovskite film in humid atmosphere

3.1 Introduction

The superior characteristics of perovskite solar cells is attributed to the high crystallinity of the perovskite material which can be prepared using one-step method with anti-solvent process. Perovskite intermediate phase is formed when the anti-solvent is dropped during the spin-coating process where the evaporation rate of the solvent determines the film thickness after which the solution becomes supersaturated, leading to nucleation and finally crystal growth. The anti-solvent is responsible for controlling the morphology of the perovskite material by inducing fast precipitation of perovskite resulting in highly dense and smooth perovskite film. Typically used anti-solvents are diethyl ether,[22] toluene,[32] chlorobenzene[44-45] and ethyl acetate[28, 33, 46] which have low boiling point, a weak electron donating capability and a poor coordination ability with perovskite precursors. The week coordination of the anti-solvents can modify the balance between the reduction of grain boundaries and the adjustment of the perovskite films.[39] Therefore, it is important to study the effect of the anti-solvent in coordinating perovskite crystal growth and film formation as the choice of the anti-solvent affects the overall morphology and hence the optoelectronic performance of the perovskite layer. In addition, the fabrication process of PSCs is usually performed inside nitrogen/argon filled glovebox to avoid moisture, as perovskite layer can degrade easily in the ambient humidity condition.[47-48] Moreover, it was reported that it was difficult to get a high-quality perovskite film by using diethyl ether, chlorobenzene or toluene as the anti-solvent in the humid ambient air.[28] Thus, it is significant chanlengeful and meaningful to prepare high-quality perovskite films in the humid ambient air. Yan group used lead (II)

thiocyanate ($Pb(SCN)_2$) to increase the humidity resistance for preparation of $MAPbI_{3-x}SCN_x$ perovskite film in more than 70 % relative humidity (RH) showing efficiency up to 15 %.[26] By employing the assistance of hydrochloric acid to accelerate $MAPbI_3$ perovskite film formation, Zhao et al prepared high quality MAPbI3 perovskite films which showing efficiency of 14.76 % in about 60 % RH air condition.[27] Watson and his group reported ethyl acetate as an anti-solvent to prepare pinhole-free MAPbI3 perovskite films with efficiency of 14.5 % in 75 % RH air atmosphere, where ethyl acetate acts as a moisture absorber protecting sensitive perovskite intermediate phases from water molecules during film formation and annealing.[28] However, there are still quite few reports on deposition of perovskite films in the high humidity ambient air condition. Generally, the morphology of perovskite film could be enhanced by controlling growth and crystallization of the perovskite.[49] There are many reports about the perovskite crystallinity enhancement by adding some additives into perovskite precursor solution, which lead to an increased photovoltaic performance of the solar cell devices.[50-53] Moreover, high performance perovskite solar cells need to be fabricated inside glovebox to avoid moisture, as organometallic halide perovskite is easily dissolved and degrade in water. A dry atmosphere slightly raises the costs of fabrication of PSCs, while the ambient air can significantly simplify fabrication processes, reduce costs and move forward commercial production of PSCs. However, as far as we know, there is no report revealing the influence of additive into anti-solvent on perovskite crystal growth and film formation in the humid ambient air. In this Chapter, we employed methanol as an additive in diethyl ether to control the morphology and investigate the growth mechanism of $MAPbI_3$ perovskite films using one-step fabrication process in high humidity atmosphere. Compared to diethyl ether, the methanol additive anti-

solvent has a stronger solubility of water and dimethyl sulfoxide (DMSO), which plays a critical role in preparing high density, pinhole-free and uniform $MAPbI_3$ perovskite film as evidenced from scanning electron microscope image and atomic force microscopy. When increasing the ratio of methanol in diethyl ether, the water resistance of perovskite is enhanced, which results in a high quality and pinhole-free perovskite film. In addition, methanol can modify a proper DMSO ratio to form in the intermediate perovskite phase accelerating perovskite crystal formation. The best solar cells exhibited PCE of 16.4 % prepared with 3 % additive anti-solvent, which is approximately 160 % higher than the devices fabricated using diethyl ether without methanol additive. We believe that this additive anti-solvent method would be useful for understanding the formation mechanism of perovskite layer and indicate a desirable direction for PSCs fabrication in humid and uncontrolled condition.

3.2 Experimental section

3.2.1 Preparation of perovskite solar cells

All reagents including diethyl ether (Aldrich, 99.8 %) and methanol (Wako, 99.5 %) were used without further purification. For preparing the additive ant-solvent, different volume methanol was added in diethyl ether, i. e 60 µl methanol was added in 2 mL diethyl ether for getting 3% methanol additive anti-solvent. F-doped SnO_2 (FTO glass, Nippon Sheet Glass Co. Ltd) substrates were first patterned and cleaned using zinc powder and 6 N hydrochloric acid solution. Tin (II) chloride (Aldrich, 98 %) was dissolved in ethanol (Wako, 99.8 %) to form 0.1 M SnCl2 solution. Then the SnCl2 solution was spin-coated on the cleaned FTO glass at 2000 rpm for 30 seconds.[29] The substrate was annealed at 180 °C for 60 minutes on a hot plate to form a dense SnO_2 electron transport layer. Equal molar ratio of

MAI (TCI, 98 %) and PbI_2 (TCI, 99.99 %) were dissolved in anhydrous dimethylformamide (DMF, Aldrich, 99.8 %) and anhydrous dimethyl sulfoxide (DMSO, Aldrich, 99.8 %) (DMF: DMSO, 4:1) to prepare 1.5 M $MAPbI_3$ precursor solution and stirred at room temperature for 1 hour. The perovskite precursor solution was spin-coated on SnO_2-coated substrate at 4000 rpm for 25 seconds and the anti-solvent (0.5 ml) was dripped on the substrate 10 seconds after starting the spin-coating process, followed by heating at 100 °C for 10 minutes. The Spiro-MeOTAD layer was prepared by spin-coating a chlorobenzene solution containing 180 mM Spiro-MeOTAD (Aldrich, 99 %), 60 mM tert-butylpyridine (Aldrich, 96 %), 30 mM Li-TFSI (Aldrich, 99.95 %) (520 mg/mL in acetonitrile) and 33 mM FK209 (Aldrich, 99 %) (300 mg/mL in acetonitrile) at 4000 rpm for 30 seconds. Finally, 80 nm-thick Au counter electrode was deposited by thermal evaporation. All procedures were performed at around 50 % relative humidity in ambient air condition (Relative humidity was recorded using a hygrometer accurate to ± 5 % RH between 25 % and 69.9 % RH, ±10 % RH between 70 % and 90 % RH) (A&D Company, AD-5681)).

3.2.2 Characterization

Solar cell performance was measured by a solar simulator (CEP-2000SRR, Bunkoukeiki Inc., AM 1.5G 100 $mWcm^{-2}$) and a mask with exposure area 0.10 cm^2 was used during the photovoltaic measurements with a 0.1 V/s scanning rate in reverse (from the open-circuit voltage (Voc) to the short-current density (Jsc)) and forward (from Jsc to Voc) modes under standard global AM 1.5 illumination. The IPCE spectra were recorded using a monochromatic Xenon lamp (Bunkouki CEP-2000SRR). X-ray Diffraction (XRD) Study. The surface morphology of the samples was observed through a scanning electron

microscope (SEM) (JEOL, Neoscope, JCM-6000) and a Bruker Innova atomic force microscopy (AFM) (JSPM-5200). Attenuated Total Reflectance Fourier transform IR spectras (FT-IR) were tested by FT-IR spectrometer (JASCO, FT/IR-4100 Series) via an attenuated total reflectance (ATR) crystal. The XRD patterns were obtained by a Rigaku Smartlab X-ray diffractometer with monochromatic Cu-Kβ irradiation (45 kV/200 mA). The UV-Vis measurement was performed using a JASCO V-670. Spectrophotometer. Electrochemical impedance spectroscopic (EIS) measurements were performed in the dark using an electrochemical workstation with a frequency range from 1 Hz to 1 MHz at 0.7 V applied bias.

3.3 Results and discussion

Figure 3.1a shows the X-ray diffraction (XRD) patterns of perovskite films prepared on glass substrates by different ratio methanol in the diethyl ether (0 %, 1 %, 2 %, 3 %, 4 %). Strong diffraction peaks locate at 14.1°, 28.4°, 31.9°, 40.7° and 43.1° for 2θ scan are observed, corresponding to the planes of (110), (220), (222), (224) and (314) of perovskite which are in agreement with previous reports.[36-38] Therefore, we can make sure from the XRD results that the perovskite films are highly crystallized perovskite phase. In addition, a weak diffraction peak of PbI_2 appeared at 12.7°, where the intensity of the peak increased upon higher methanol ratio. This increment of PbI_2 concentration could be ascribed to the high solubility of methylammonium iodide (MAI) in methanol in which the methylammonium component is removed from the perovskite structure leaving behind PbI_2.[54] It is noticed that (110) peaks shifted to the left (Figure 3.1b) when compared to the control sample, suggesting that the crystallites are experiencing homogenous strain as there was only peak shift but not peak broadening.[55] Figure 3.1c shows the UV-vis absorption spectra of the different

perovskite samples. The absorbance increased upon addition of methanol reaching the highest absorbance at 3% methanol concentration and then started to decrease when more methanol is added. This is mainly due to improved surface coverage and reduction of pinholes of the perovskite thin film. [56-57]

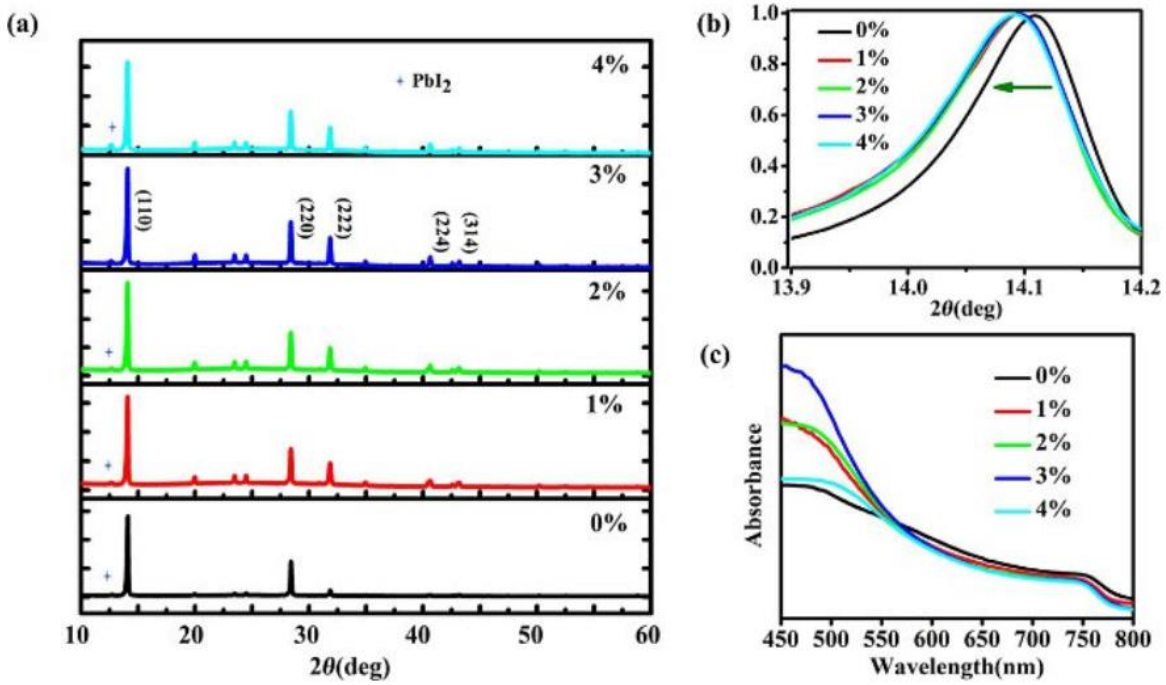

Figure 3.1. (a) XRD of $MAPbI_3$ films on glass substrates prepared by different methanol additive in diethyl ether (0%, 1%, 2%, 3%, 4%). (b) Normalized XRD plot of (110) peak. (c) UV-vis absorption spectra of perovskite films prepared by various concentration of additive anti-solvent.

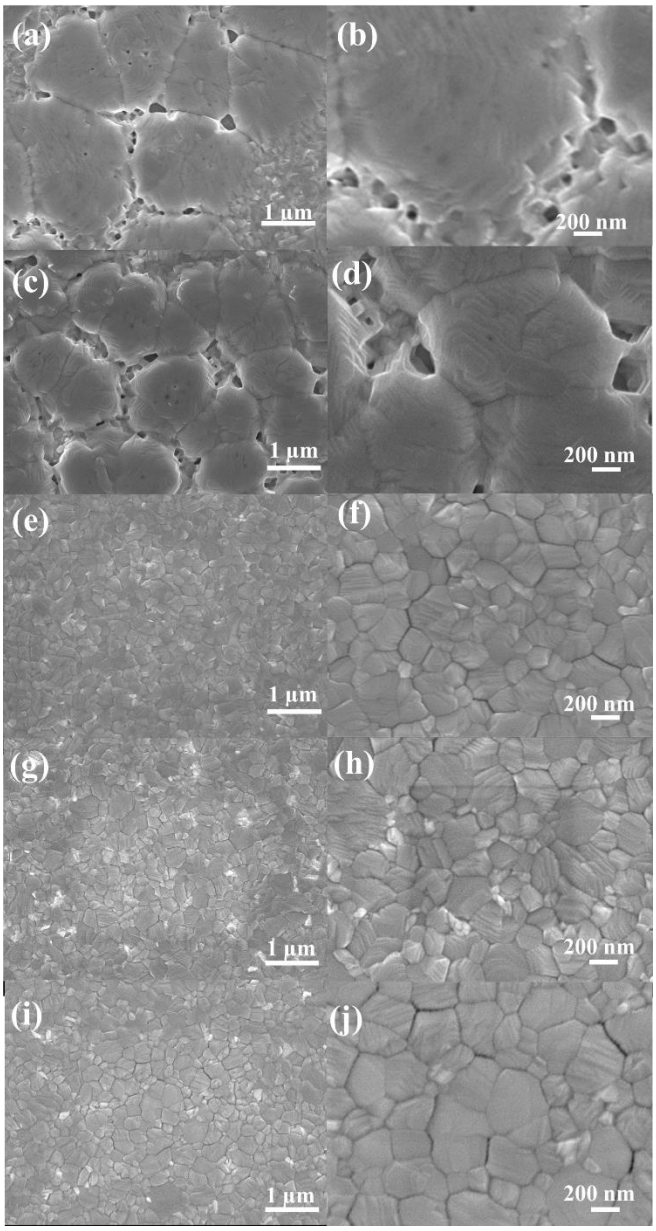

Figure 3.2. SEM images of annealed $MAPbI_3$ perovskite film on FTO substrates prepared by different methanol content in diethyl ether. (a) (b) 0 %; (c) (d) 1 %; (e) (f) 2 %; (g) (h) 3 %; (i) (j) 4 %.

Figure 3.2 shows the surface morphology of annealed $MAPbI_3$ perovskite films prepared by different methanol additive ratio anti-solvent by SEM. With diethyl ether, it can be seen the crystals are badly formed with the presence of pinholes. When 1 % addition of

methanol, similar morphology was observed. However, adding 2 % and more methanol changed the morphology significantly. The crystallinity of the perovskite sample was improved in which the size distribution is homogenous throughout the sample in addition to the reduction of pinholes. The largest crystal size was obtained with the sample prepared using 4% methanol although there was a big inhomogeneity in size between grains. The statistical result of grain size of the film has been summarized in Figure 3.3, with an average grain size of 240 nm for 2 % additive anti-solvent, 340 nm for 3 % additive anti-solvent, and 280 nm for 4 % additive anti-solvent. For the 0 % and 1 % additive anti-solvent sample, the average size could not be determined due to the poorly formed crystals.

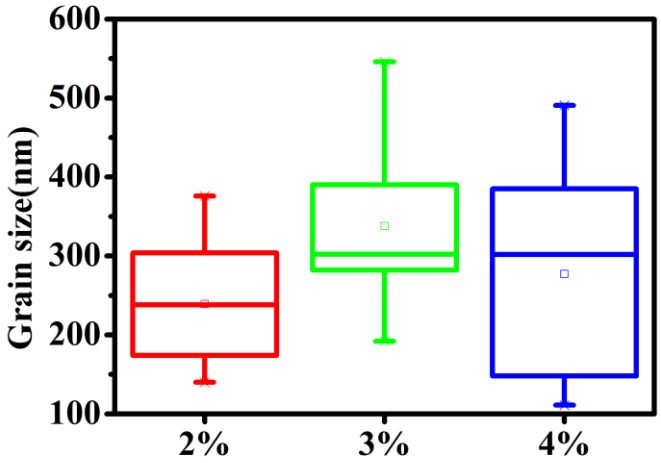

Figure 3.3 The statistics of grain size based on the SEM image of $MAPbI_3$ perovskite films on FTO glasses prepared by 2%, 3%, and 4% methanol additive anti-solvent.

Figure 3.4 shows the AFM images of perovskite film prepared by different methanol ratio additive anti-solvent. The Rq roughness values were measured to be 26.9, 23.1, 11.6, 10.4 and 10.1 for samples prepared by different methanol content of 0 %, 1 %, 2 %, 3 % and 4 %, respectively. The decreased roughness from methanol content from 0 % to 4 % supports

the data obtained from SEM images in which high quality with improved surface morphology is obtained with methanol addition. The 3D surface images shown in Figure 3.4 b, d, f, h, j clearly shows the decrease of surface roughness of the perovskite films. It is expected that these improvements will be reflected at the perovskite/Spiro-OMeTAD interface which could enhance the performance of the solar cells.

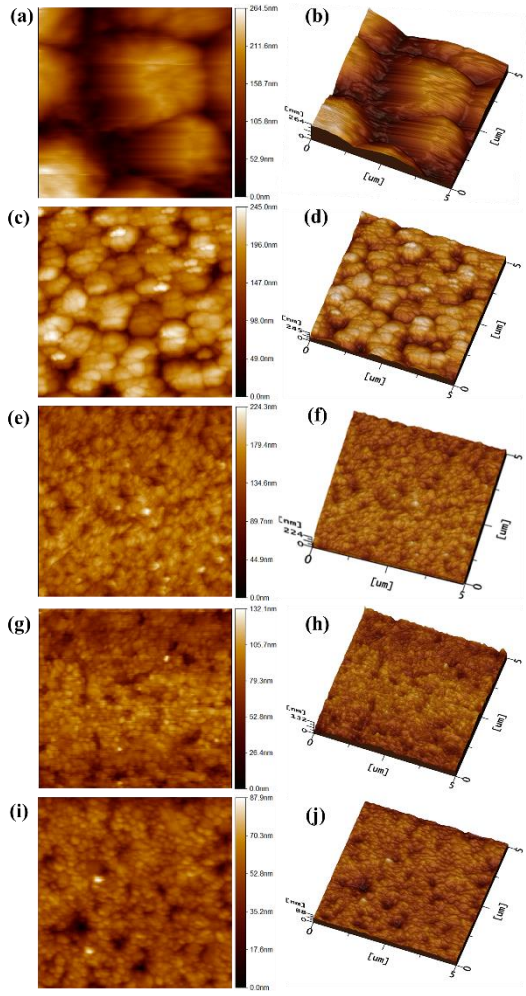

Figure 3.4. AFM images (a, c, e, g, i) and the corresponding 3D surface plot images (b, d, f, h, j) of $MAPbI_3$ films prepared by different methanol additive content anti-solvent. (a) (b) 0 %; (c) (d) 1 %; (e) (f) 2 %; (g) (h) 3 %; (i) (j) 4 %.

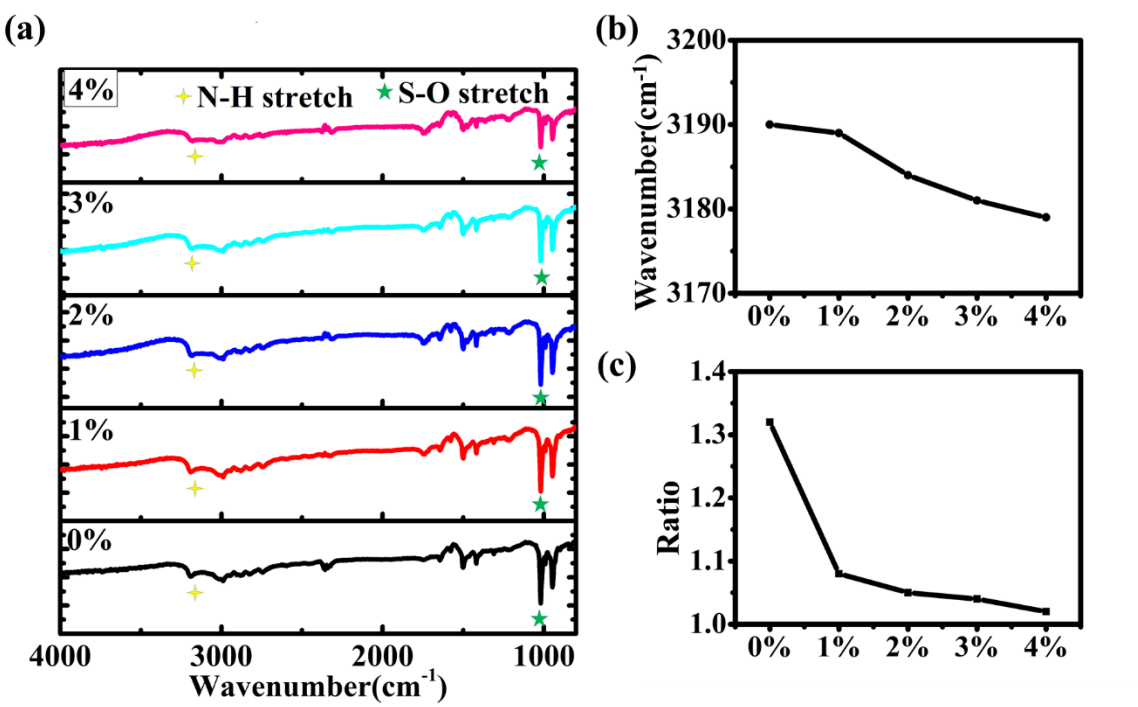

Figure 3.5. (a) Attenuated Total Reflectance FTIR spectra of $MAPbI_3$ films (on Pt substrates) prepared by different methanol concentration additive anti-solvent (0%, 1%, 2%, 3%, 4%). (b) The N-H stretch peak position of the non-annealed film by different methanol additive anti-solvent. (c) Ratio of intensity of absorbance at 1020 cm^{-1} to 3190 cm^{-1} (1020 cm^{-1}: 3190 cm^{-1}).

Figure 3.5 shows FTIR spectra of perovskite films prior to annealing prepared by various methanol concentration in the additive anti-solvent (0 %, 1 %, 2 %, 3 %, 4 %). The films of perovskite intermediate phase demonstrated similar peak positions. The S–O stretching vibration and N–H stretching vibration are located at 1020 cm^{-1} and around 3190 cm^{-1}, respectively, as shown in Figure 3.5a.[58] The N-H peak shifted to long wavenumber when N-H bond coordinated to DMSO, implying that an intermediate phase of MAI-PbI_2-DMSO has been formed.[59-60] The N-H peak of the intermediate phase is at 3190 cm^{-1} for 0 % methanol concentration in the additive anti-solvent, 2189 cm^{-1} for 1 % methanol additive , 3184 cm^{-1} for 2 % methanol additive , 3181 cm^{-1} for 3 % methanol additive and 3179 cm^{-1}

for 4 % methanol additive . This means that amount of DMSO is extracted by the additive anti-solvent method. In addition, the change of DMSO concentration in the intermediate phase can be deduced by calculating the ratio of S-O intensity peak at 1020 cm^{-1} to N-H intensity peak at around 3190 cm^{-1} shown in Figure 3.5c. The ratio decreased from 1.32, 1.08, 1.05, and 1.04 to 1.02 as the methanol content is increased. Park et al. reported that excessive amount of DMSO in the perovskite intermediate phase would lead to an inhomogeneous perovskite film because of the gradual vaporization of DMSO from the perovskite film.[22] In addition, the less DMSO in the intermediate phase also means that the time needed for the phase change from perovskite intermediate phase to perovskite film is accelerated.[61] Inversely, excessive amount of DMSO in the intermediate phase also lead to inhomogeneous perovskite film with small grain size. Therefore, by adjusting the methanol ratio in the additive anti-solvent, a proper amount of DMSO into the perovskite intermediate phase can be controlled to assist crystallization leading to a pinhole-free homogenous perovskite film.

In the anti-solvent based one-step preparation process, the perovskite layer is formed by spin coating of the precursor solution followed by the thermal annealing. This preparation process usually has two stages. In the first stage, the liquid film is thinning by the centrifugal forces. After a transition point, evaporation rate of the solvent dominates the film thinning, which depends on the vapor pressure of the solvent. Then at the second stage, solution becomes supersaturated, nucleation happens and growths, solid intermediate (or perovskite) film forms. Thus, in order to prepare high-quality perovskite film, the important stage is to accelerate the evaporation rate of excess DMF and control the perovskite crystallization process.[30] For two immiscible solvents, the total vapor pressure of the mixed solution is close to the plus of the two solvents' vapor pressures, and the boiling point of the mixture should

be lower than each solvent.[31] Follow this rule, introducing the high vapor pressure anti-solvent for one-step preparing perovskite film will help promote a uniform and high-quality film. In addition, after the perovskite intermediate phase formed in the humid air atmosphere, it is better to reduce contacting time of this intermediate phase with the moisture within the air to avoid the water affection. Therefore, the second way is to speed up the perovskite nucleus growth rate to reduce the formation time of perovskite intermediate phase to perovskite. Figure 3.6 shows the schematic diagram representing the perovskite crystal growth mechanism between pure diethyl ether and the additive anti-solvent. It is known that diethyl ether has high vapor pressure (71.8 Kpa at 25 ºC) and is immiscible in both DMSO and water (1.5 vol% of water). [62-63] While, DMSO, water and methanol are mutual miscible. During the normal diethyl ether anti-solvent process, diethyl ether quickly extracts DMF from the perovskite film. As the same time, perovskite and perovskite precursors are insoluble in diethyl ether. Therefore, after diethyl ether extracting the solvents from the perovskite film in the washing process, some water from the humid air atmosphere remains on the wet MAI-PbI_2-DMSO perovskite intermediate film before annealing and can only be removed upon heating above 100 ºC. Hence, an inhomogeneous film with many pinholes and rough surface is formed, which was proved by the SEM image of Figure 3.2a. When methanol is added into the diethyl ether, methanol removes the residual water quickly through its infinite solubility with water, which lead to a pinhole-free homogeneous film with a smoother surface, shown in SEM image of Figure 3.2g. Meanwhile, methanol could also remove redundant DMSO from the perovskite intermediate phase to accelerate the perovskite formation as methanol can slightly dissolve DMSO, which was proved by the FIIR spectra in Figure 3.5.

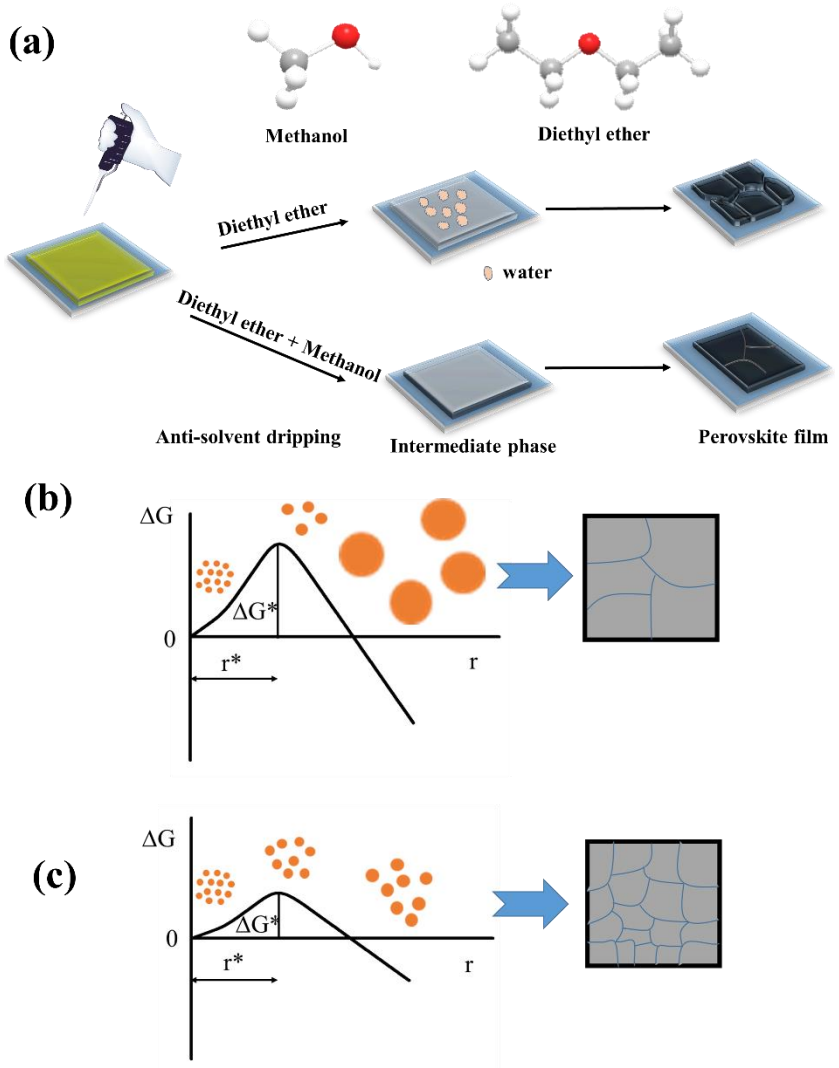

Figure 3.6. (a) Schematic diagram of anti-solvent step using diethyl ether and methanol additive diethyl ether. (b) Gibbs free energy diagrams for nucleation and growth of $MAPbI_3$ perovskite film by diethyl ether anti-solvent. (c) Gibbs free energy diagrams for nucleation and growth of $MAPbI_3$ perovskite film by methanol additive diethyl ether anti-solvent.

It is suggested a proper intermediate phase is a key point for preparing the perovskite layer with desirable morphology.[64] Thus, an optimum methanol concentration can extract suitable amount of DMSO content from the precursor solutions to accelerate the perovskite formation and give an appropriate MAI-PbI_2-DMSO intermediate phase. On the other hand,

in the perovskite film growth process, the crystal grain growth rate is determined by the Gibbs free energy, which includes chemical energy difference, surface energy and interface energy of the grains. Acik and co-workers have proved that the overall Gibbs free energy was lower when using alcohols (include methanol) to catalyze the growth of $MAPbI_3$ crystals.[65] In the common homogenous nucleation, the relationship of overall Gibbs free energy change (ΔG) and nucleus radius (r) can be given as the equation:[66]

$$\Delta G(r) = -\frac{4\pi r^3}{3V_M} RT \ln(S) + 4\pi r^2 \gamma$$

where R, T, S, γ and V_M represent gas constant, absolute temperature, supersaturating ratio, energy of liquid-crystalline nucleus interface and nucleus` molar volume, respectively. Figure 3.6b and 3.6c schematically depict the Gibbs free energy diagrams as a function of nuclei radius in case of the anti-solvent treatment without or with methanol additive. When methanol is used as an additive in the anti-solvent for preparing the perovskite film, the Gibbs free energy is lower than that of without methanol additive because of the chemical heterogeneity effect.[67] As a result, more nuclei are formed, which lead to the small size grain growth, shown in Figure 3.2c.

The effect of methanol additive into diethyl ether anti-solvent method on solar cells performance was investigated via planar FTO/SnO_2/$MAPbI_3$/Spiro/Au perovskite solar cells. Devices were fabricated under around 50 % RH humid air condition. Figure 3.7a, b illustrates the schematic structure and energy diagram of the PSCs. Figure 3.7c shows the J−V curves of devices prepared with various methanol concentration in the additive anti-solvent. The measured photovoltaic parameters of the champion the different devices are listed in Table 3.1. Device prepared using only diethyl ether showed the lowest power conversion efficiency of 6.3 % mainly due to the low V_{OC}. Upon addition of methanol into the anti-solvent, there

is an increasing trend of all the parameters of PSCs. The most efficient device was prepared by 3 % methanol additive anti-solvent, with a champion PCE of 16.4 %, J_{sc} of 22.48 mA/cm^2, V_{OC} of 1.04 V, and FF of 70.0 %. The efficiency value is approximately 160 % higher than the cell fabricated using pure diethyl ether as anti-solvent treatment. The obtained JSC follows the same trend as the UV-Vis absorption spectra in which 3 % sample has the highest absorption followed by 2 %, 4%, 1 % and finally 0 %. The high absorptance resulted in higher number of photons being absorbed by the perovskite active layer and be converted into electrons.

Table 3.1. Photovoltaic parameters of champion planar PSCs devices.

Condition[a]	J_{sc} (mA/cm^2)	Voc (V)	FF (%)	PCE (%)
0%	18.93	0.61	53.9	6.3
1%	19.60	0.93	63.4	11.6
2%	21.71	1.03	63.5	14.2
3%	22.48	1.04	70.0	16.4
4%	21.06	0.98	63.4	13.1

[a] The ratio of different methanol concentration in diethyl ether (0%, 1%, 2%, 3%, 4%).

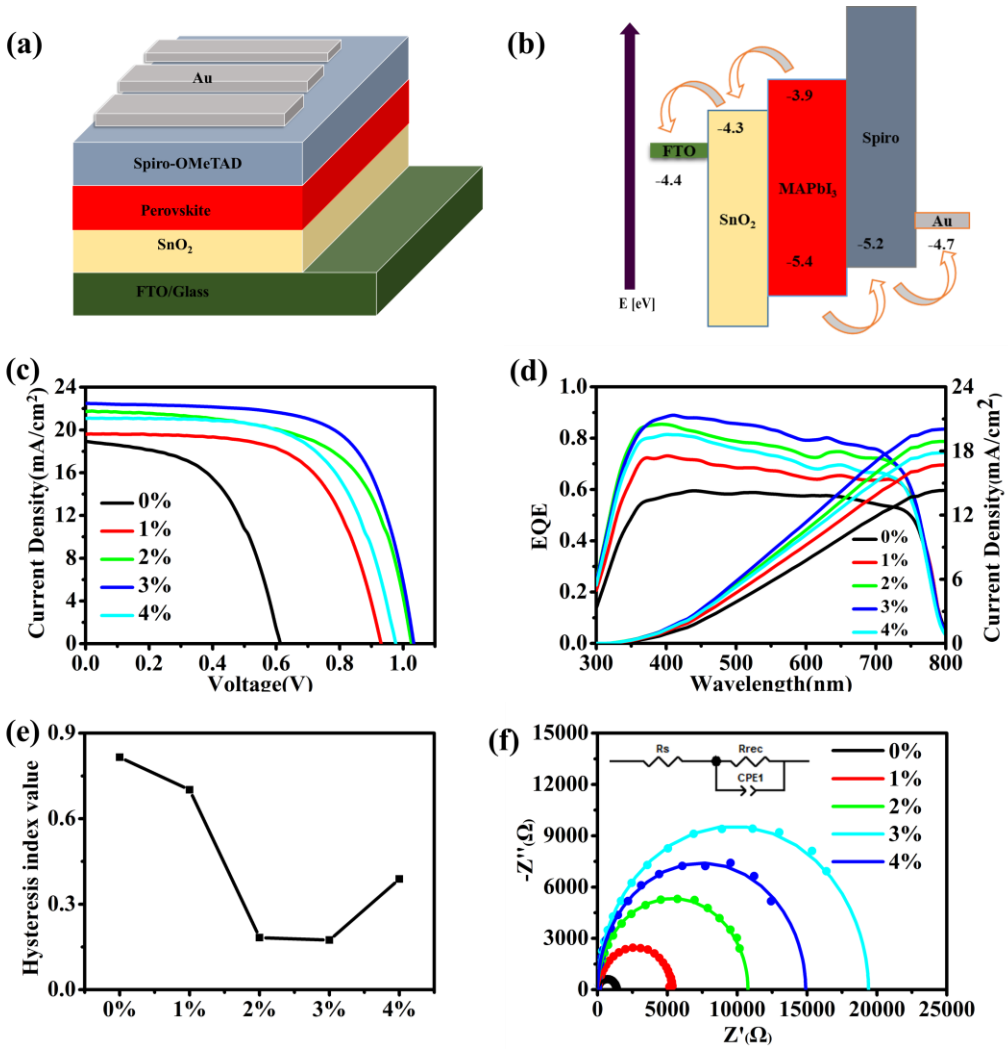

Figure 3.7. Schematic structure (a) and (b) energy diagram of the planar FTO/SnO_2/ $MAPbI_3$/Spiro-OMeTAD/Au planar perovskite solar cells. (c) J−V curves of the control and additive anti-solvent as anti-solvent treated devices measured under illumination of an AM 1.5 solar simulator (100 mWcm $^{-2}$) in air. The scanning direction is from open-circuit voltage to short-circuit current (reverse). (d) EQE spectra of the control and additive anti-solvent as anti-solvent treated devices measured in air. (e) Hysteresis index value calculated from the J-V curves; (f) The Nyquist plots of different condition additive anti-solvent based planar champion devices measured in the dark under 0.7 V applied bias and the equivalent circuit diagram, the fitted curves and the experimental data are shown as solid lines corresponding

points, respectively. (a) Attenuated Total Reflectance FTIR spectra of $MAPbI_3$ films (on Pt substrates) prepared by different methanol concentration additive anti-solvent (0 %, 1 %, 2 %, 3 %, 4 %). (b) The N-H stretch peak position of the non-annealed film by different methanol additive anti-solvent. (c) Ratio of intensity of absorbance at 1020 cm^{-1} to 3190 cm^{-1} (1020 cm^{-1}: 3190 cm^{-1}).

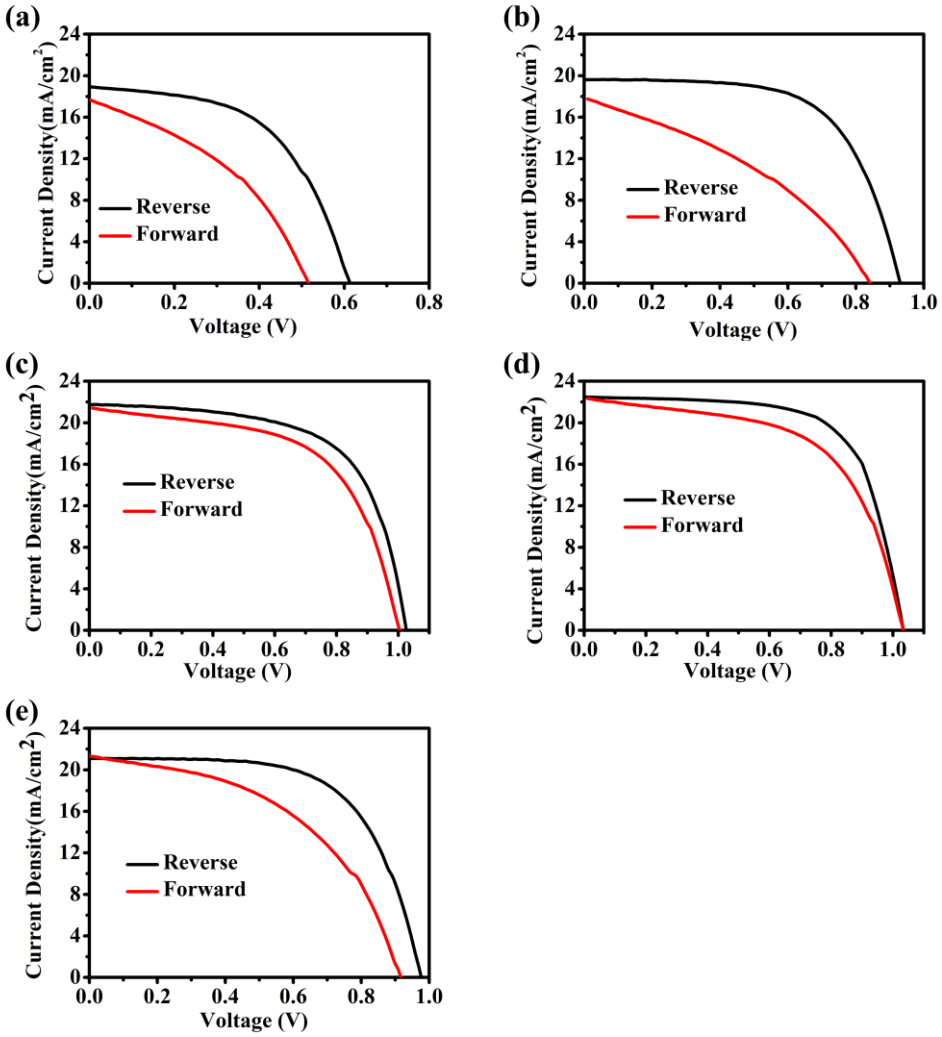

Figure 3.8 J–V curves of the best-performing $MAPbI_3$ solar cells prepared by different methanol additive anti-solvent under reverse and forward voltage scans. (a) 0 %; (b) 1 %; (c) 2 %; (d) 3 %; (i) (e) 4 %.

The calculated J_{SC} is obtained by integrating the IPCE curve shown in Figure 3.7d. The value obtained is in agreement with the measured value from the J-V curve. Figure 3.8 demonstrates the J-V curve of reverse and forward direction for each type of device. Figure 3.9 shows the photovoltaic statistics for the planar PSCs prepared by different additive anti-solvent condition.

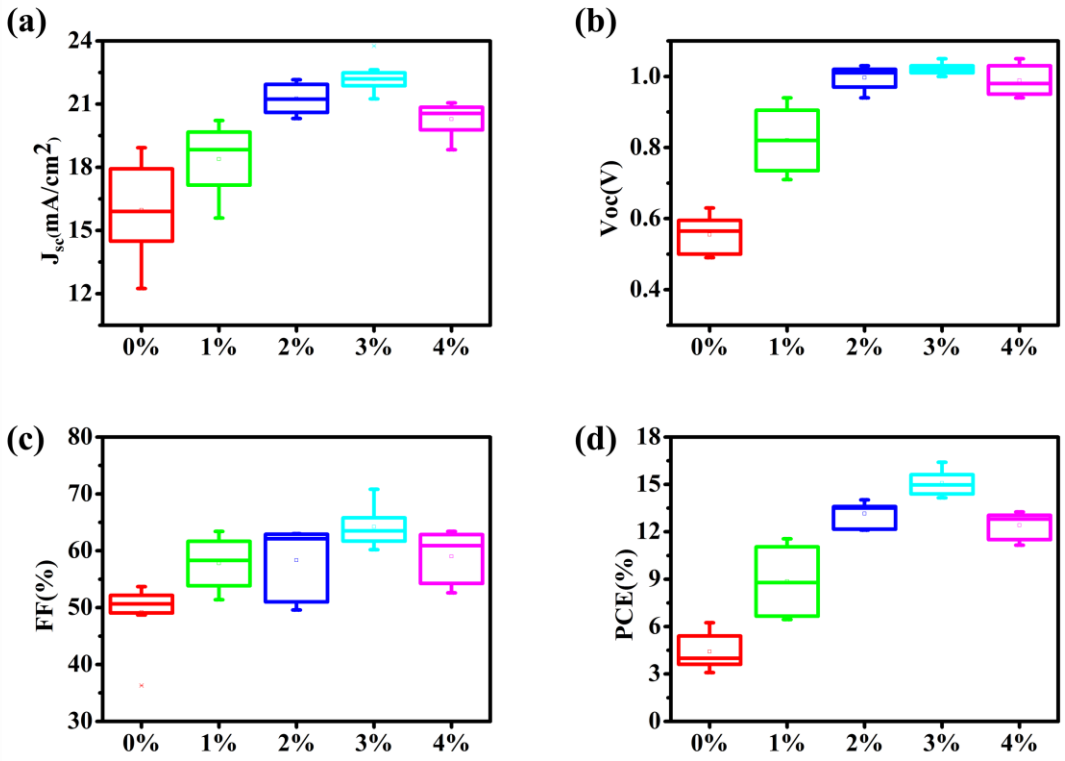

Figure 3.9 Photovoltaic statistics for the planar perovskite solar cells processed by different methanol additive mixed anti-solvent. (a) J_{SC}, (b) V_{OC}, (c) Fill factor, (d) Efficiency. The boxes represent 40 data from the V_{OC}-to-J_{SC} scan direction.

In order to compare the quality of the perovskite layers and hence the PSCs, the hysteresis index (HI) value was calculated shown in Figure 3.7e.[43] The HI value was 0.81 for 0 % methanol additive, 0.70 for 1 % methanol additive, 0.18 for 2 % methanol additive, 0.17

for 3 % methanol additive, and 0.38 for 4 % methanol additive, respectively which means the hysteresis of PSCs decreased as the methanol content increased. There are many reports analyzing the origin of hysteresis in perovskite solar cells such as ionic motions within perovskite, charge trapping and de-trapping due to crystal defects and band bending between the different interfaces. Such low HI index could be attributed to the uniform growth of the $MAPbI_3$ layer obtained by additive anti-solvent deposition process, effectively reducing the presence of grain boundaries and thus charge transfer between grains are more efficient.

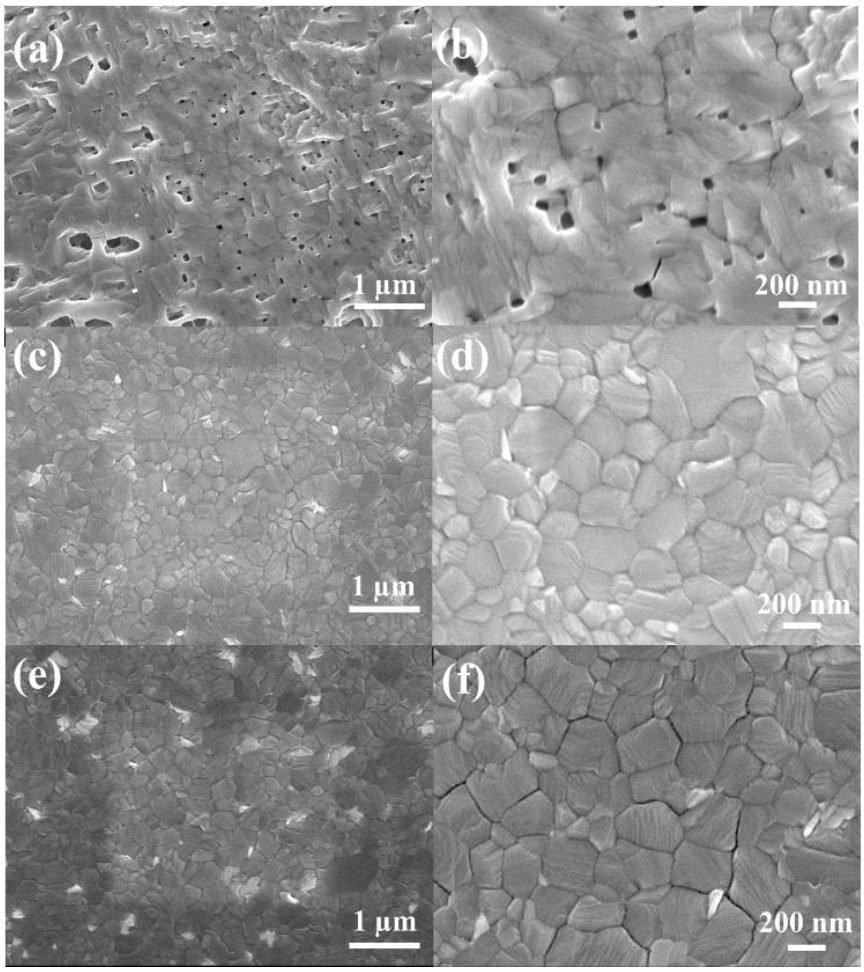

Figure 3.10. SEM images of annealed $MAPbI_3$ perovskite film on FTO substrates by water contaminated additive anti-solvent. (a) (b) 0.5 % water in diethyl ether; (c) (d) 0.5 % water in 3 % methanol additive anti-solvent; (e) (f) 1 % water in 3 % methanol additive anti-solvent.

To investigate the charge transfer mechanism at the interfaces, electrochemical impedance spectroscopy (EIS) measurement was performed. The Nyquist plots of PSC devices are shown in Figure 3.7f where the illustrated equivalent circuit diagram was used to fit the plot. Here, one semicircle is seen at high frequency corresponding to the charge transport at the back electrode and hole transporting material (HTM) as reported previously.[68] From Figure 3.7f, the same trend as the J-V curve is observed with the Nyquist plot where the sample prepared with 3 % methanol additive anti-solvent has the highest recombination resistance (R_{rec}) as determined from the width of the semicircle and decreased when less methanol content was employed. The large R_{rec} suggests that the electron-hole recombination is suppressed at the $MAPbI_3$/Spiro interface due to better interfacial contact because of the pinhole-free perovskite layer. This allows for efficient charge extraction at both the electron and hole transporting materials.

Upon addition of a small amount of methanol into the anti-solvent, it is assumed that the water retention of the additive anti-solvent is enhanced compared to pure diethyl ether. To confirm this hypothesis, deionized water was deliberately added to the anhydrous diethyl ether and 3 % methanol additive anti-solvent. Figure 3.10 shows the SEM images of perovskite films fabricated with different water content added to diethyl ether and 3 % methanol additive anti-solvent. In the case of 0.5 % volume water added to pure diethyl ether, the formation of more pinholes was observed as shown in Figure 3.10a. This is due to more water molecules present in the perovskite intermediate phase during crystal growth. However, the 3 % additive anti-solvent contaminated with even 1 % water exhibited crystalline and a pinhole-free surface which is due to the miscibility of water in methanol and thus the water molecules are extracted together with methanol. Furthermore, planar perovskite solar cells

were prepared by 3 % additive anti-solvent contaminated with 0.5 % and 1 % water, shown in Figure 3.11. For 0.5 % water in 3% additive methanol anti-solvent treatment device, we can got the PCE up to 14.3%. And for 1 % water in 3% additive methanol anti-solvent treatment device, the champion PCE was 12.3%. However, for the 0.5 % water in only diethyl ether anti-solvent, the champion PCE is just 4.6 %. Those results mean that disadvantage in the presence of moisture (water) can be nearly prevented by utilizing the methanol additive anti-solvent method.

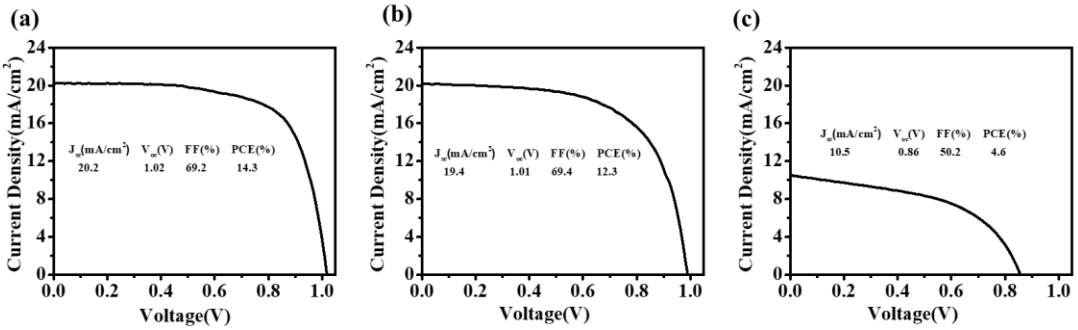

Figure 3.11. J−V curves of the best-performing $MAPbI_3$ solar cells prepared by different volum ratio water in anti-solvent under reverse scan. (a) 0.5 % water in 3 % methanol additive diethyl ether anti-solvent. (b) 1 % water in 3 % methanol additive diethyl ether anti-solvent. (c) 0.5 % water in diethyl ether anti-solvent.

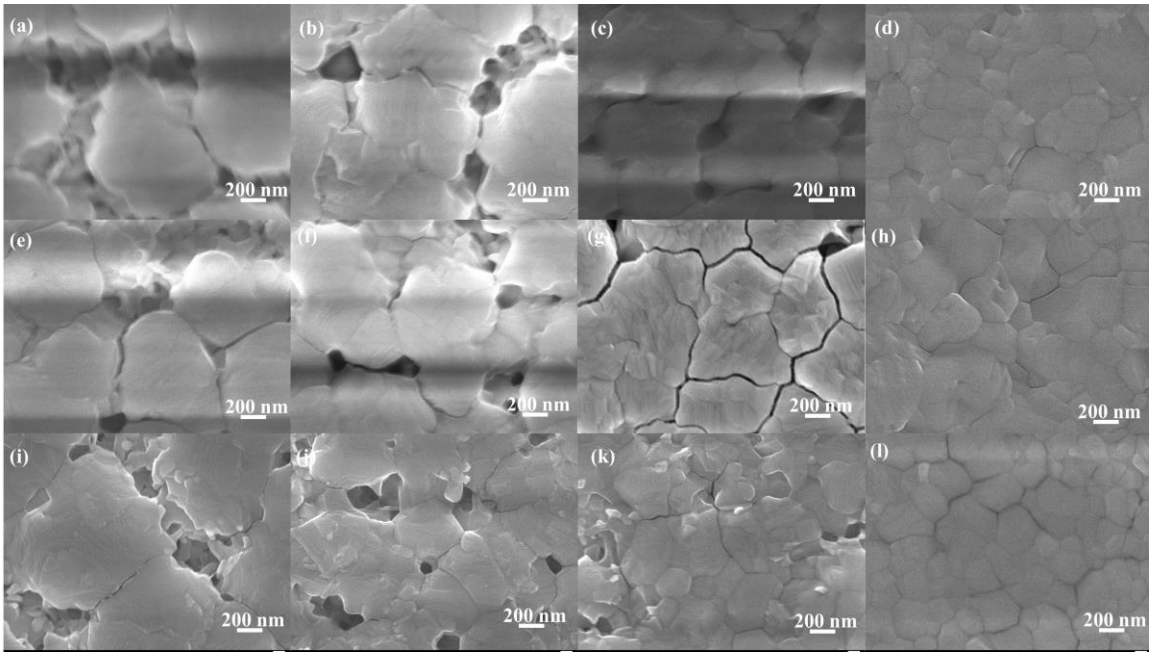

Figure 3.12 SEM images of $MAPbI_3$ perovskite film prepared by different kind of alcohol additive into diethyl ether anti-solvent. (a) 2% ethanol. (b) 3% ethanol. (c) 4% ethanol. (d) 5% ethanol. (e) 2% 2-propanol. (f) 4% 2-propanol. (g) 6% 2-propanol. (h) 8% 2-propanol. (i) 3% 1-butanol. (j) 6% 1-butanol. (k) 9% 1-butanol. (l) 12% 1-butanol.

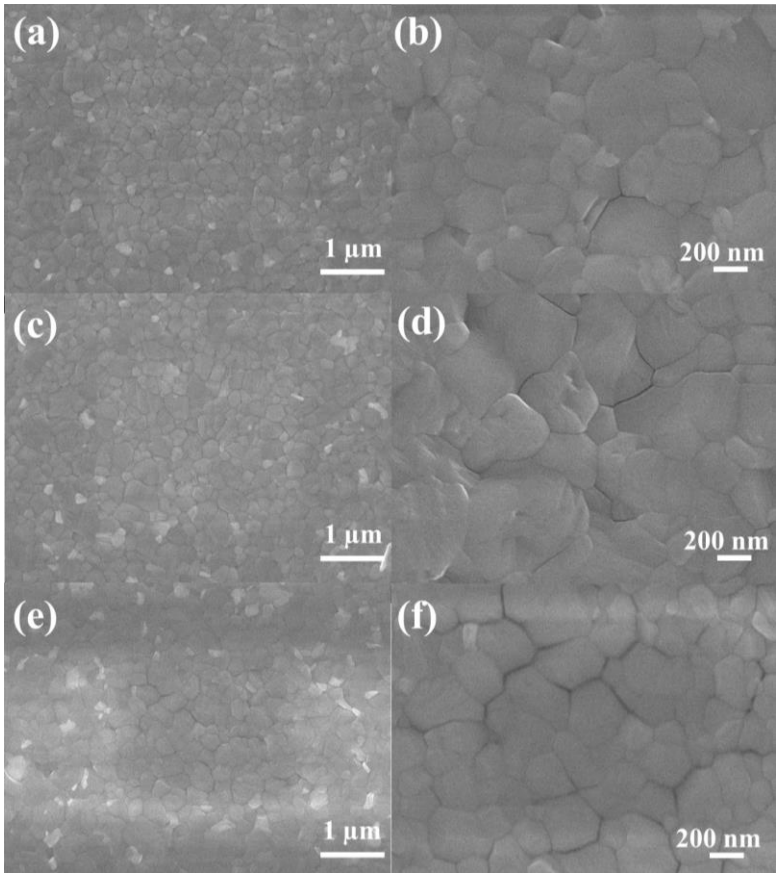

Figure 3.13. SEM images of annealed $MAPbI_3$ perovskite film on FTO substrates by different kind of alcohol additive anti-solvent. (a) (b) 5% ethanol additive in diethyl ether; (c) (d) 8 % 2-propanol additive in diethyl ether anti-solvent; (e) (f) 12 % 1-butanol additive in diethyl ether anti-solvent.

To further investigate universality of the additive method, other alcohols including ethanol, 2-propanol and 1-butanol were used as the additive into diethyl ether anti-solvent for preparing $MAPbI_3$ perovskite films and solar cells. An interesting sight is that when increasing the alcohol additive content in diethyl ether, similar results were achieved. With the raise of alcohol` content, the perovskite film showed less pinholes, shown in Figure 3.12. At last, the pinhole free perovskite films were obtained by 5% ethanol, 8% 2-propanol and 12% 1-butanol, respectively, shown in Figure 3.13. Then planar solar cells were prepared by

5% ethanol, 8% 2-propanol and 12% 1-butanol additive in diethyl ether anti-solvent. The champion device for 5% ethanol additive anti-solvent is 15.4%, for 8% 2-propanol additive anti-solvent is 14.8% and for 12% 1-butanol additive is 15.2 %, shown in Figure 3.14. Those results demonstrated that the additive method is a universal method for preparing the high quality perovskite films in the humid air atmosphere. Therefore, from the above discussion, we can draw the conclusion that alcohols additive in diethyl ether will be a good direction for the fabrication of high performing perovskite solar cells in humid ambient atmosphere which is beneficial from the low-cost and mass-production point of view.

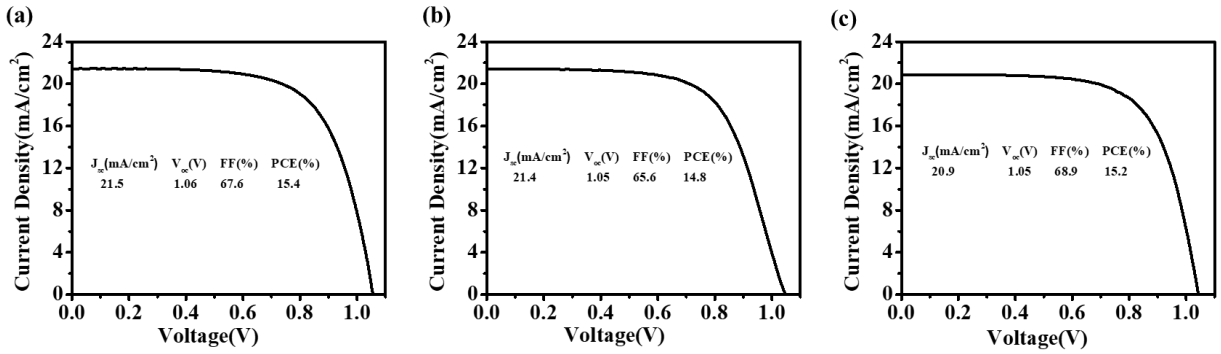

Figure 3.14. J-V curve of the champion perovskite solar cell prepared by 3% different kind of alcohol additive into diethyl ether anti-solvent. (a) 5% ethanol. (b) 8% 2-propanol (c) 12% 1-butanol.

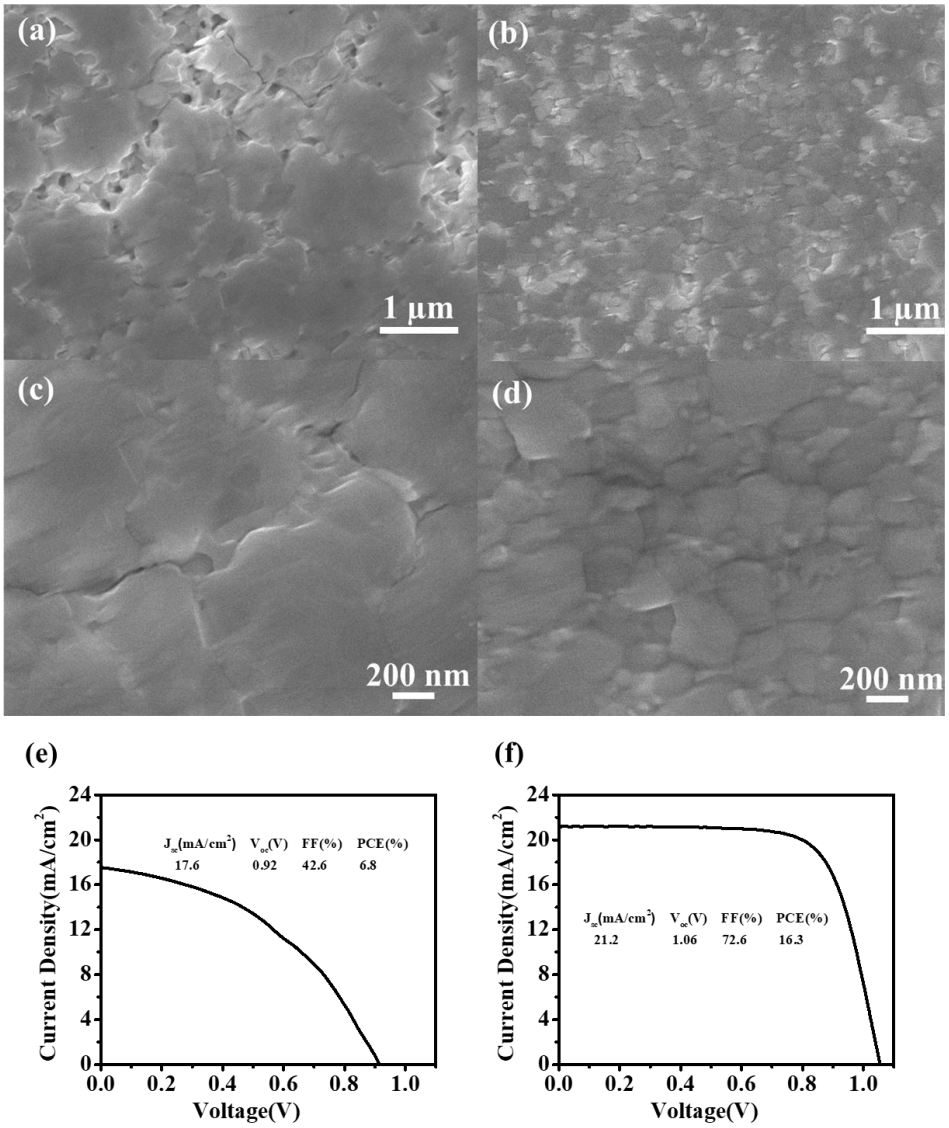

Figure 3.15 (a) (c) SEM images of $MAPbI_3$ perovskite film prepared by diethyl ether anti-solvent in around 30% RH air atmosphere. (b) (d) SEM images of $MAPbI_3$ perovskite film prepared by 3% methanol additive diethyl ether anti-solvent in around 30% RH air atmosphere. (e) J-V curve of the champion perovskite solar cell prepared by diethyl ether anti-solvent in 30% RH air atmosphere. (f) J-V curve of the champion perovskite solar cell prepared by 3% methanol additive diethyl ether anti-solvent in around 30% RH air atmosphere.

3.4 Conclusion

In conclusion, high performing planar $MAPbI_3$ perovskite solar cells has been fabricated at high relative humidity (around 50 % RH) using methanol additive into diethyl ether anti-solvent. The highest solar cell efficiency was obtained with perovskite layer prepared with 3 % methanol in diethyl ether showing a PCE of 16.4 %, V_{oc} of 1.04 V, J_{sc} of 22.48 mA/cm^2, and FF of 70.0 %. The reason for this high performing device can be attributed to the formation of dense perovskite film with smooth surface due to fast extraction of water molecules during annealing as methanol has high water solubility. This has been proved experimentally by deliberately adding water into the perovskite precursor solution and prepared the perovskite solar cells using 3 % methanol-diethyl ether anti-solvent. Despite the addition of water in the precursor solution, the film still showed highly crystalline and smooth surface morphology. Additionally, addition of methanol can provide the optimum DMSO content in the intermediate perovskite phase to accelerate perovskite formation. Moreover, due to the improved interfacial contact of the highly crystalline perovskite, the hysteresis issue has been improved together with the reduction of electron-hole recombination reaction as seen from the impedance measurement. Furthermore other alcohols including ethanol, 2-propanol and 1-butanol were tried as the additive into diethyl ether similarly worked as well, which proving the universal usage of the additive into anti-solvent method. This work provides a good direction for the fabrication of high performing perovskite solar cells at high humidity ambient atmosphere which is beneficial from the low-cost and mass-production point of view.

Chapter 4. Magnesium iodide additive into $MAPbI_3$ Perovskite Layer in Humid Air Atmosphere

4.1 Introduction

The prototypical organic-inorganic perovskite, $MAPbI_3$ (MA, $CH_3NH_3^+$) has a tetragonal structure and a band gap of around 1.5 eV. Despite these excellent properties, the material is still far from being used in real application due to low stability in air and prone to degradation in humid atmosphere.[28, 69-70] The organic cation MA is mainly responsible for the tetragonal structure stability and $MAPbI_3$ perovskite layer. And it has been reported that partial caesium or rubidium substitution of MA can effectively improve the stability because of the smaller size of inorganic cation could induce an entropic stabilisation.[71-72] The electronic properties of perovskite material are mainly determined by the Pb-site. Moreover, the chemical composition of the perovskite also determine the electrical and optical properties of the perovskite materials.[73] Therefore, partials substituting lead or doping with other metals cations can effectively modify the optoelectronic properties of perovskite materials.[74-76] Zhao et al. investigated the effect of alkali metal doing in $MAPbI_3$ perovskite.[77] They suggested that potassium passivated the trap states in the perovskite and led to bigger grain size. Similar effect has also been observed in the case of doping with bivalent and trivalent metals, Zn^{2+}, Sb^{3+} and Sr^{2+}.[78-80] Doping of $MAPbI_3$ with Ag has also been investigated where decreased in the electron concentration and thus improved electron mobility has been cited as the factors leading to the increase in the PSC efficiency.[81] The nontoxic alkaline-earth metals of beryllium (Be, ionic radius 59 pm) magnesium (Mg, ionic radius 86 pm), calcium (Ca, ionic radius 114pm), strontium (Sr, ionic radius 132 pm), and

barium (Ba, ionic radius 149 pm) are the earth abundant elements have a stable divalent oxidation state which are considered of good candidates for the replacement of toxic lead (Pb, ionic radius 132 pm). Many studies have focused on research in the energy band structure by doping the perovskite with Ba^{2+}, Sr^{2+} and Ca^{2+}.[82-84] However, rarely no experiment research of Mg^{2+} doping into the perovskite is reported. The band gap of $MAMgI_3$ is 1.39 eV that is obvious narrower than the other three metals (3.97 eV, 3.94 eV and 3.89 eV for $MABaI_3$ $MASrI_3$ and $MACaI_3$, respectively), which is approach to the band gap of $MAPbI_3$ (1.55 eV).[85] In addition, $MAMgI_3$ exhibits a strong and wide absorption at 4.5-9.5 eV in the ultraviolet spectrum region, which would be a promising material for solar cells in the region. Therefore, research in how Mg^{2+} affect into energy band structure and the morphology of the perovskite will be challenge and meaningful.

In this chapter, for the first time, we explored experimentally the effect of Mg doping in $MAPbI_3$ perovskite. The X-ray diffraction (XRD) analysis shows that there was no change in the crystal structure of the perovskite upon doping with Mg. Although the doping did not alter bandgap of the perovskite, from the photoelectron yield spectroscopy measurement, the valence band value became deeper. The perovskite materials were then evaluated for their photovoltaic properties and the lifetime stability was also performed at 30-40 % relative humidity (RH). The efficiency of the solar cell was increased from 14.2 % of the doping-free solar cell to 17.8 % of 1.0 % Mg doped device. Moreover, 90 % of the original PCE was still retained after storage in 30~40% relative humidity for 600 h.

4.2 Experimental section

4.2.1 Preparation of perovskite solar cells

Fluorine-doped tin oxide (FTO glass, Nippon Sheet Glass Co. Ltd) substrates were etched with r hydrochloric acid solution and zinc powder. The titanium dioxide compact layer was spin-coated 0.15 M titanium diisopropoxide bis(acetyacetonate) (75 wt% in isopropanol, Aldrich) in 1-butanol (99.8 %, Aldrich) on an the FTO substrate at 2000 rpm for 30 seconds. Then the substrate was heated at 125 ^{o}C for 5 min. Next, the titanium dioxide paste (Dyesol 30NRD, diluted in ethanol at 1:4 weight ratio) was spin-coated at 500 rpm 5s and 5000 rpm for 30 s. After drying at 125 °C for 30 min, the substrate was annealed at 500 °C for 30 min. The perovskite solution was prepared by dissolving 239 mg MAI (TCI, 98 %) and 692mg PbI_2 (TCI, 99.99 %) into 0.2 mL dimethyl sulfoxide (DMSO, Aldrich, 99.8 %) and 0.8 mL dimethylformamide (DMF, Aldrich, 99.8 %) to achieve 1.5 M $MAPbI_3$ perovskite precursor solution. For preparing the Mg doped perovskite precursor solution, adding the proper ratio of MgI_2 (99.998 %, Aldrich) into the 1.5 M $MAPbI_3$ perovskite precursor solution. The Spiro-MeOTAD solution was prepared by mixing 72.3 mg Spiro-MeOTAD (Aldrich, 99 %), 28.8 μ L tert-butylpyridine (Aldrich, 96 %) , 17.5 μ L Li-TFSI (Aldrich, 99.95 %) (520 mg/mL in acetonitrile) and 29 μ L FK209 (Aldrich, 99 %) (300 mg/mL in acetonitrile) in 1 mL chlorobenzene solution. The perovskite layer was prepared on the mesoporous TiO_2 substrate by adding 0.1 mL perovskite precursor solution and spin-coated at 4000 rpm for 25 s. 0.5 mL ethyl acetate (99.8 %, Aldrich) antisolvent was dripped during the spin-coated progress.[86] The spin-coated perovskite film was annealed at 100 °C for 10 min. The Spiro-MeOTAD layer spin-coated on the perovskite layer at 4000 rpm for 30 s. Finally, Au electrode with 80 nm thickness was deposited on the Spiro film by thermal evaporation.

4.2.2 Characterization

Current-density-voltage curves of the perovskite solar cells with a 0.10 cm^2 exposure area were measured under AM 1.5G 100 $mWcm^{-2}$ irradiation uing a solar simulator (CEP-2000SRR, Bunkoukeiki Inc.,). The EQE spectra were recorded using a Xenon lamp, a potentiostat and a monochromator (Bunkouki CEP-2000SRR). The scanning electron microscope (JEOL, Neoscope, JSM-6700F) was used to measure morphologies of perovskite layer. XRD patterns were obtained by the monochromatic Cu-Kβ irradiation with a X-ray diffractometer (Rigaku Smartlab, 45 kV/200 mA). The UV-Vis spectra was obtained with a UV/Vis spectrophotometer (JASCO V-670). Electrochemical impedance spectroscopic measurements were tested with a frequency range from 1 Hz to 1 MHz at 0.7 V applied bias under dark condition. Photoelectron yield spectroscopy (PYS) was used to determine the valence band using a Bunkoukeiki KV205-HK ionization energy measurement system with – 5.0 V of applied voltage under 10^{-4} Pa vacuum.

4.3 Result and discussion

Figure 4.1a shows XRD patterns of differFent molar ratio Mg doped $MAPbI_3$ perovskite films (0.0 %, 0.5 %, 1.0 %, and 2.0 %). All the films were prepared on glass substrates using ethyl acetate as the anti-solvent by one-step spin-coating method at 30%~40% RH air atmosphere. Strong intensity peaks at 14.09°, 28.42°, 31.85°, 40.63° and 43.16° were observed, which are well-oriented in (110), (220), (222), (224) and (314) directions of the $MAPbI_3$ perovskite. This is consistent with previous researches.[36, 38, 87]

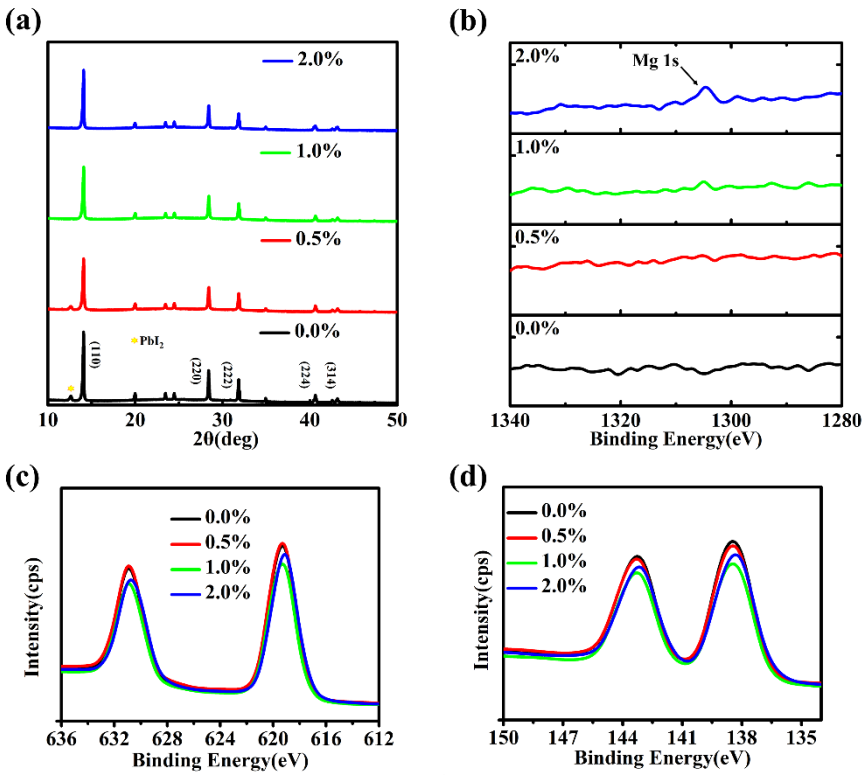

Figure 4.1. (a) XRD spectra of different molar ratio Mg doped $MAPbI_3$ perovskite layer on glass substrate. (b) XPS core level spectra of Mg 1s; (c) XPS core level spectra of Pb 4f; and (d) XPS core level spectra of I 3d. The XPS sample was prepared by spin-coating Mg doped $MAPbI_3$ perovskite precursor solution on 2×2 cm FTO substrates.

In addition, a weak diffraction peak appeared at 12.7° which is assigned to PbI_2, where the peak intensity decreased upon increasing Mg doping, and nearly no peak appeared when the doping ratio was more than 1.0 % which is exhibited in XRD patterns between 12.0° and 13.0° shown in Figure 4.2. Thelakkat et. al. proved that the rate of degradation of $CH_3NH_3PbI_3$ could be accelerated because of PbI_2 residue present in the perovskite film.[88] Moreover, researchers have proved that the surface defects and trap state density originating from uncoordinated Pb atoms of the residual PbI_2 limiting the performance of PSCs.[89] This

means Mg doping into $MAPbI_3$ perovskite layer enhanced the conversion from PbI_2 to complete $MAPbI_3$ perovskite. Additionally, it also indirectly indicates that Mg doping enhanced moisture resistance of the perovskite films as it is known that $MAPbI_3$ tend to degrade into PbI_2 in the presence of water.[47-48]

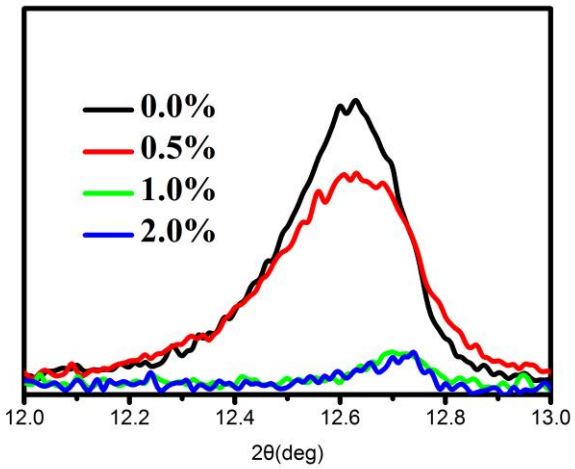

Figure 4.2. The Zoomed XRD peak of PbI_2 pattern.

Hydrophobicity is another factor to confirm moisture resistance of the perovskite films. Therefore, the contact angles of the pristine and 1.0% Mg doped $MAPbI_3$ perovskite were measured and shown in Figure 4.3. Contact angle of the 1.0 % Mg doped MAPbI3 film is calculated to be 69.9°, which is evidently larger than that of the pristine film with 50.3°. The increase of water contact angle suggests the enhancement on water-resistance of the 1.0% Mg doped perovskite film, which is beneficial for long-term stability of the solar cells. The wide scan of X-ray photoelectron spectroscopy (XPS) of different molar ratio Mg doped $MAPbI_3$ perovskite are exhibited in Figure 4.4. Figure 4.1b shows a peak position at 1304 eV which is assigned to Mg 1s peak, and the intensity increased when increasing the Mg doping suggesting that Mg is successfully doped into the $MAPbI_3$ structure.[90] Figure 4.1c, d

shows the Pb 4f and I 3d core levels which indicate the I/Pb surface atomic ratio are close to 3 in all the films. Moreover, the Pb 4f and I 3d peaks move to lower binding energy when increasing the Mg doping content, suggesting a change in the oxidation state of Pb and I with the addition of MgI_2.[91]

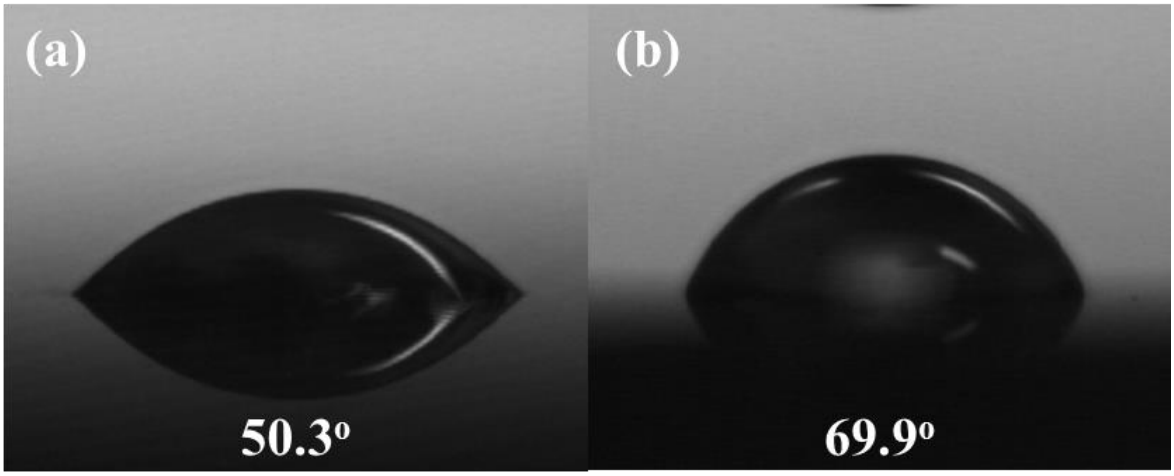

Figure 4.3. The contact angle between perovskite film and water droplet. (a) Pristine $MAPbI_3$ and (b) 1.0 % MgI_2-doped

Figure 4.5a shows the UV-vis absorption spectra of different molar ratio Mg doped $MAPbI_3$ perovskite layers. It is obviously that the absorbance of Mg doped perovskite layer increased compared to pristine $MAPbI_3$ film. The increased absorbance can be attributed to better surface coverage and pinhole-free morphology of the perovskite layer.[57] The band gaps are calculated from Tauc plot are shown in Figure 4.5b. The optical band gap decreased marginally from 1.571 eV for pure $MAPbI_3$ perovskite to 1.547 eV for 2.0% Mg doping. Photoelectron yield spectroscopy (PYS) was utilized to measure the valence band of the perovskite materials.[92-94] The valence band edge of the perovskite films showed a clear

decreasing trend after incorporation of Mg into $MAPbI_3$ perovskite, as determined by photoelectron spectroscopy in air, shown in Figure 4.5c. The valence band edge shifted from -5.56 eV of $MAPbI_3$ to more negative values of -5.60 eV, -5.62 eV and -5.65 eV for 0.5 %, 1.0 % and 2.0 % Mg doping, respectively. Based on the above results, the energy diagram upon Mg doping is given in Figure 4.5d. The valence electron of lead and magnesium is $5d^{10}/6s^2/6p^2$ and $2s^2/2p^6/3s^2$, respectively. When Mg was doping into the perovskite, the carrier transition was changed from Mg 1p—Mg 1s of the pristine MgI_2 to the Mg 1d—Mg 1s of the doped perovskite, which was shown in Figure S8. For the Mg doping $MAPbI_3$ perovskite, the valence bands are mostly occupied by the p orbitals of iodide atoms, and the conduction bands contain of a large proportion of the s orbitals of Magnesium atoms and the p orbitals of the lead atoms.[95] It is clear shown in Figure 4.5d that the electronic configuration of $MAPbI_3$ suffers only minor changes when incorporation of low content of MgI_2, which is critical in order to retain the high photovoltaic performance of $MAPbI_3$ perovskite materials.[96]

Figure 4.6 shows the top-view morphology of the different molar ratio Mg doped $MAPbI_3$ perovskite layers observed by scanning electron microscopy (SEM). It can be calculated that the average grain size is around 110 nm of pristine $MAPbI_3$ film, 190 nm for 0.5 %, 580 nm for 1.0 % and 600 nm of 2.0 % Mg doped sample. It is clear the grain size gradually increased when increasing the doping content from 0.0 % to 2.0 %. However, 2.0% Mg doped film showed cracks and especially significant for the 4.0% Mg doped as shown in Figure 4.7. The cracks have been reported to be mainly caused by the mechanical stress because of the fast growth rate of perovskite film during annealing step.[97] The grain size is one of the governing parameters for determining the diffusion length and the charge carrier

recombination rate.[98] Small grain size directly correlates to large number of grain boundaries in the perovskite layer. Not only these sites act as charge trap sites, but also they are prone to attack by water molecules and these will accelerate degradation of the perovskite.

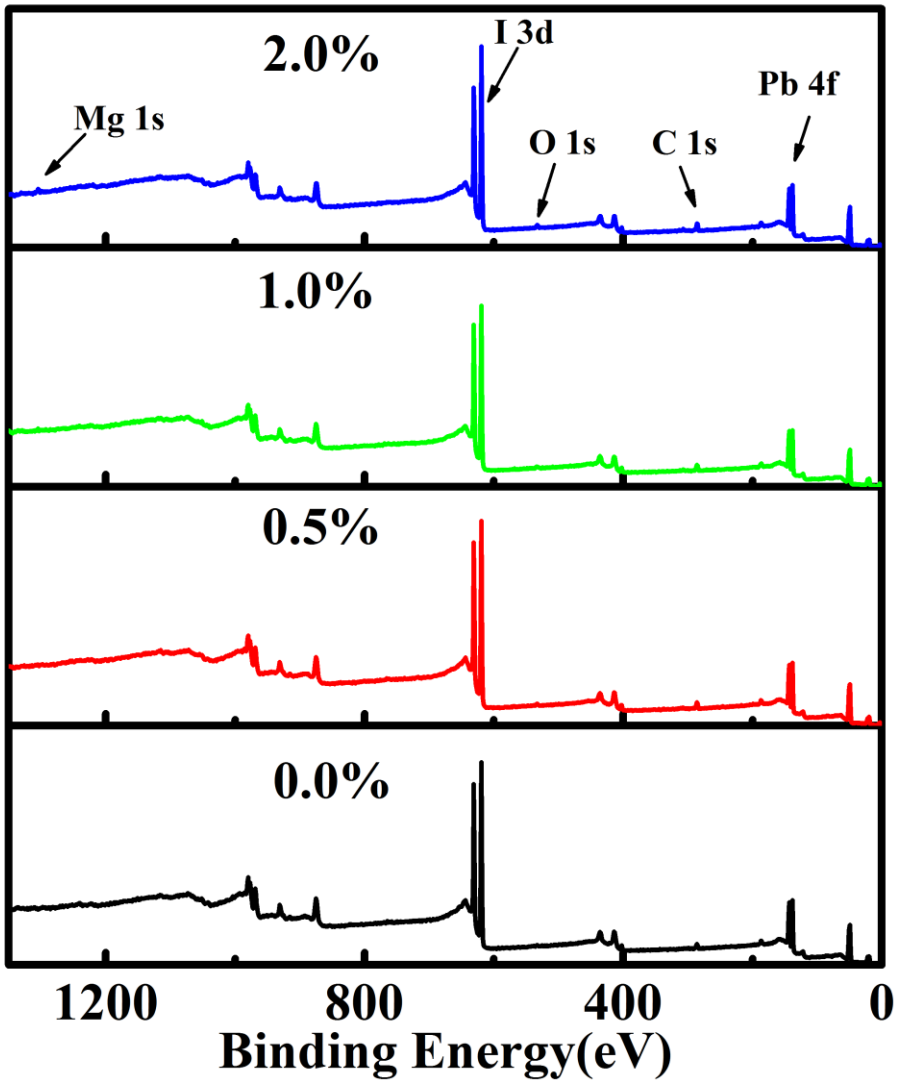

Figure 4.4. The surface-sensitive XPS spectra of different content MgI_2-doped $MAPbI_3$ perovskite film on FTO glass substrates.

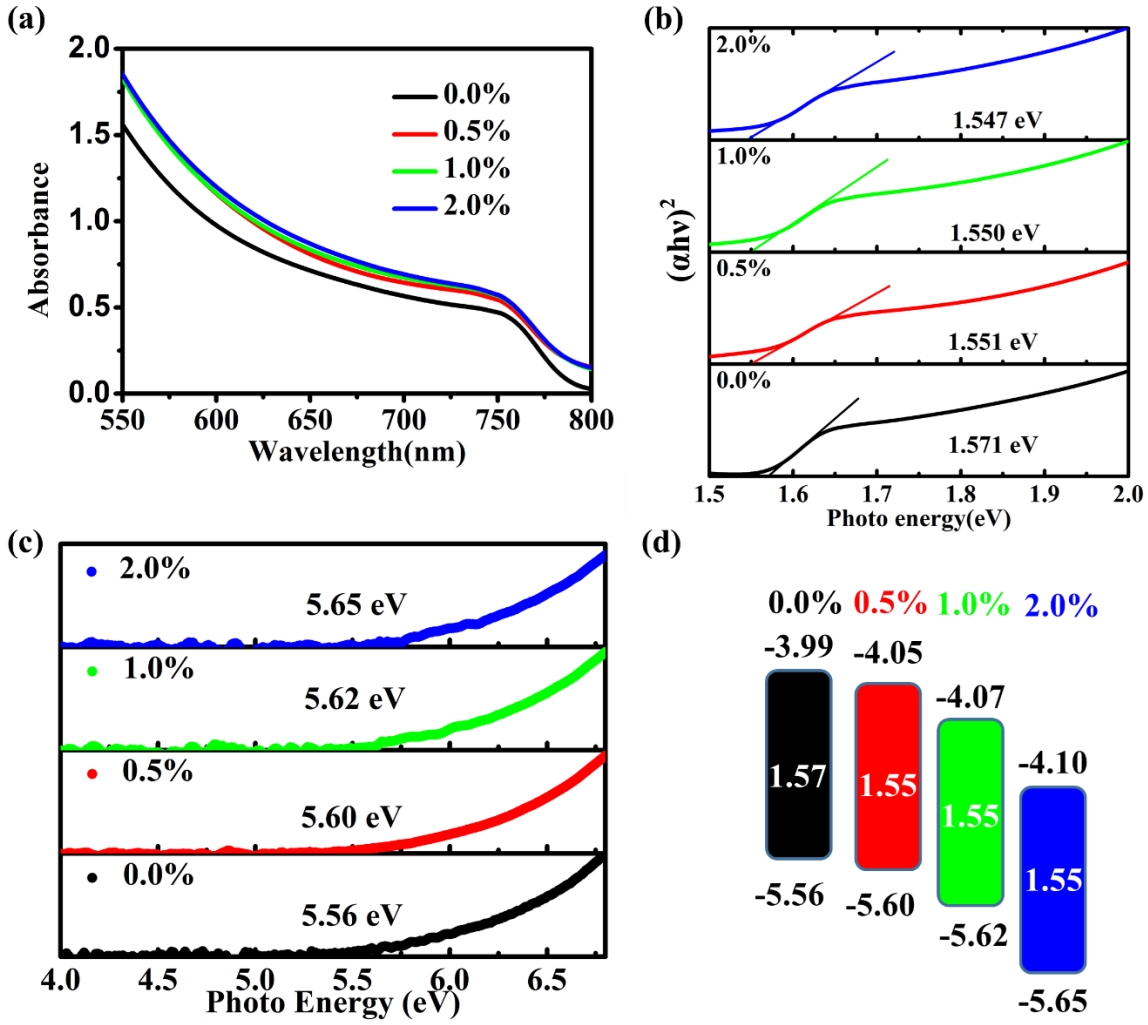

Figure 4.5. (a) UV-vis spectra of different Mg doped $MAPbI_3$ perovskite films on glass substrates. (b) $(ahv)^2$ versus energy. (c) PESA measurement of different Mg doped perovskite films on FTO glass substrates and (d) The corresponding energy diagram.

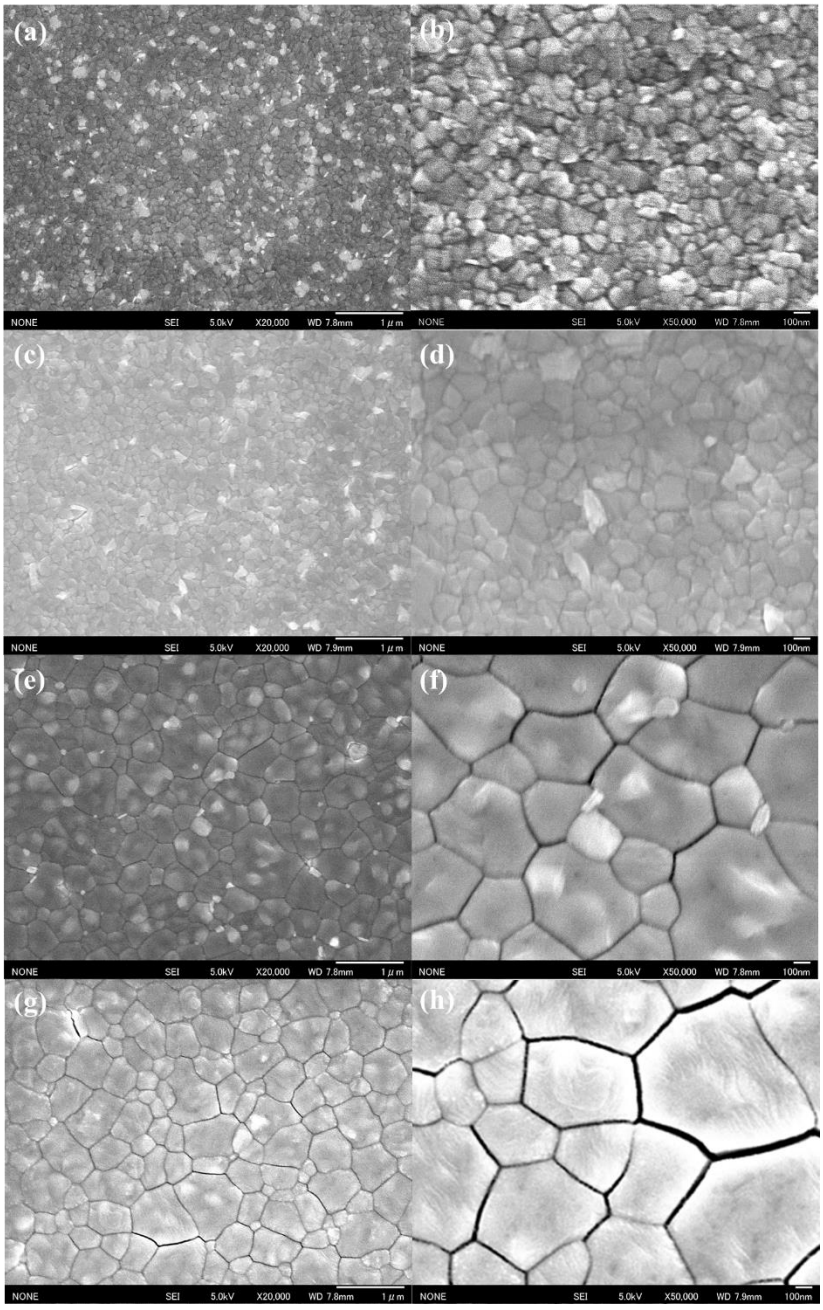

Figure 4.6. Top view SEM images of the different Mg doped MAPbI3 perovskite layers on FTO/compact TiO_2/Mesoporous TiO_2 substrates. (a) (b) 0.0%; (c) (d) 0.5%; (e) (f) 1.0%; (g) (h) 2.0%. Scale bar for (a) (c) (e) (g) is 1μm and (b) (d) (f) (h) is 100 nm.

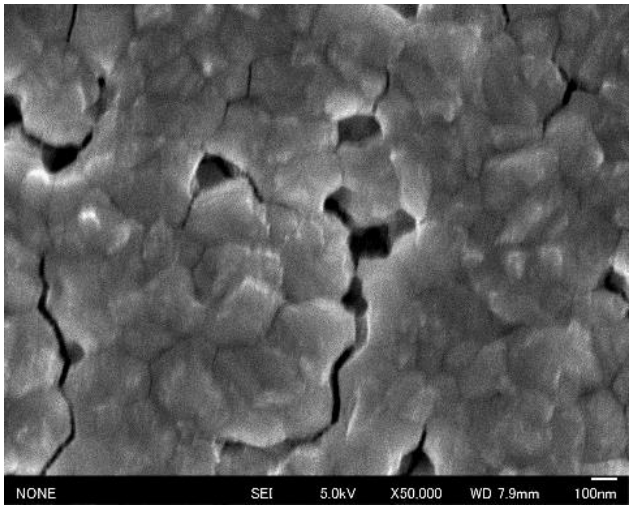

Figure 4.7 SEM images of the annealed 4% Mg-dopedMAPbI$_3$ perovskite layers on FTO/compact TiO2/mesoporous TiO2 substrate. Scan bar: 100 nm.

During the growth process of perovskite layer, the growth rate of crystal grain is determined by the Gibbs free energy. The relationship between the nucleus radius (r) and overall Gibbs free energy change (ΔG) can be derived from the equation[66]

$$\Delta G(r) = -\frac{4\pi r^3}{3V_M} RT \ln(S) + 4\pi r^2 \gamma$$

Where S, γ, R, T and V_M represent supersaturation ratio, energy of liquid-crystalline nucleus interface, gas constant, absolute temperature and nucleus` molar volume, respectively. Figure 4.8 a, b schematically depict the Gibbs free energy diagrams as a function of nuclei radius in case of MgI_2 doping. Doping Mg into the perovskite can increse the Gibbs free energy owning to the effect of chemical heterogeneity.[43, 87] As a result, less nucleis are formed, which lead to the bigger grain size. On the other hand, the coordination interaction between $CH_3NH_3^+$ and Mg^{2+} is higher than that of $CH_3NH_3^+$ and Pb^{2+}, which results in the electron cloud become more closer between $CH_3NH_3^+$ and Mg^{2+} metal ion, which also affects the crystallization of the perovskite film.[99-100] Therefore, the stronger

coordination function with organic groups, along with a higher chemical interaction between Mg^{2+} and anions, which could make the Mg doped perovskite layer prefer to grow bigger grain sizes.

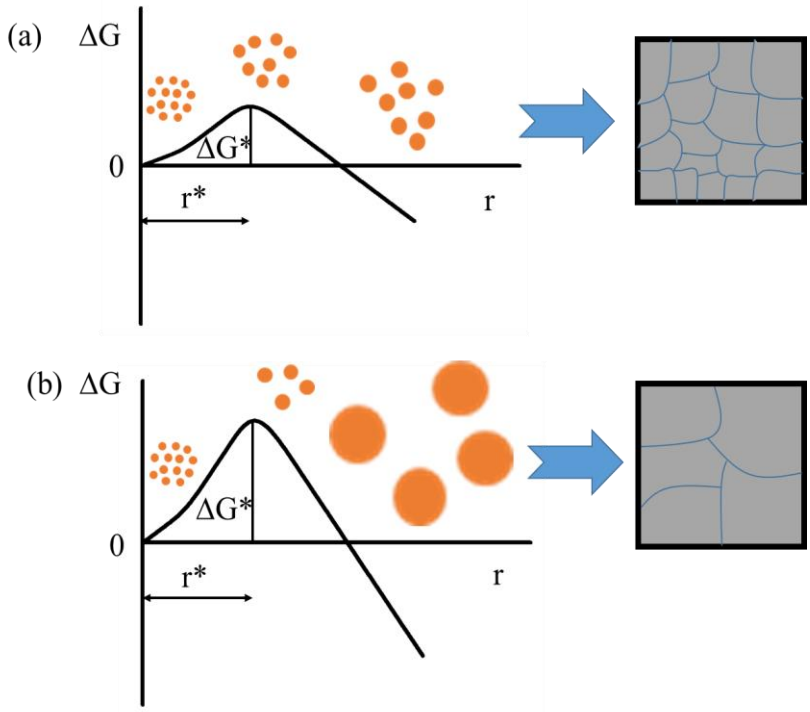

Figure 4.8. (a) Gibbs free energy diagram for nucleation and growth the pristine $MAPbI_3$ layer, (b) Gibbs free energy diagram for nucleation and growth the Mg doped $MAPbI_3$ layer.

The effect of different molar ratio Mg doped perovskite on solar cells performance was investigated with solar cells having the structure of FTO/Compact TiO_2/Mesoporous TiO_2/Perovskite/Spiro/Au. Devices were fabricated at 30~40% RH atmosphere. The pristine device measured on the reverse direction has PCE of 14.5 %, short-circuit current density (J_{sc}) of 21.56 mA/cm^2, open-circuit voltage (V_{oc}) of 1.05 V, and fill factor (FF) of 64.5 %. All the photovoltaic parameters increased upon doping with Mg as shown in Figure 4.9a. The 1.0% Mg doped device measured on the reverse scan has a PCE of 17.8 %, along with J_{sc} of

22.72 mA/cm^2, V_{oc} of 1.08 V and FF of 72.3 %. However, 2.0 % Mg doped device showed low performance with PCE of 12.8 % which could be explained by the obvious cracks on the perovskite film (Figure 4.6 g, h).

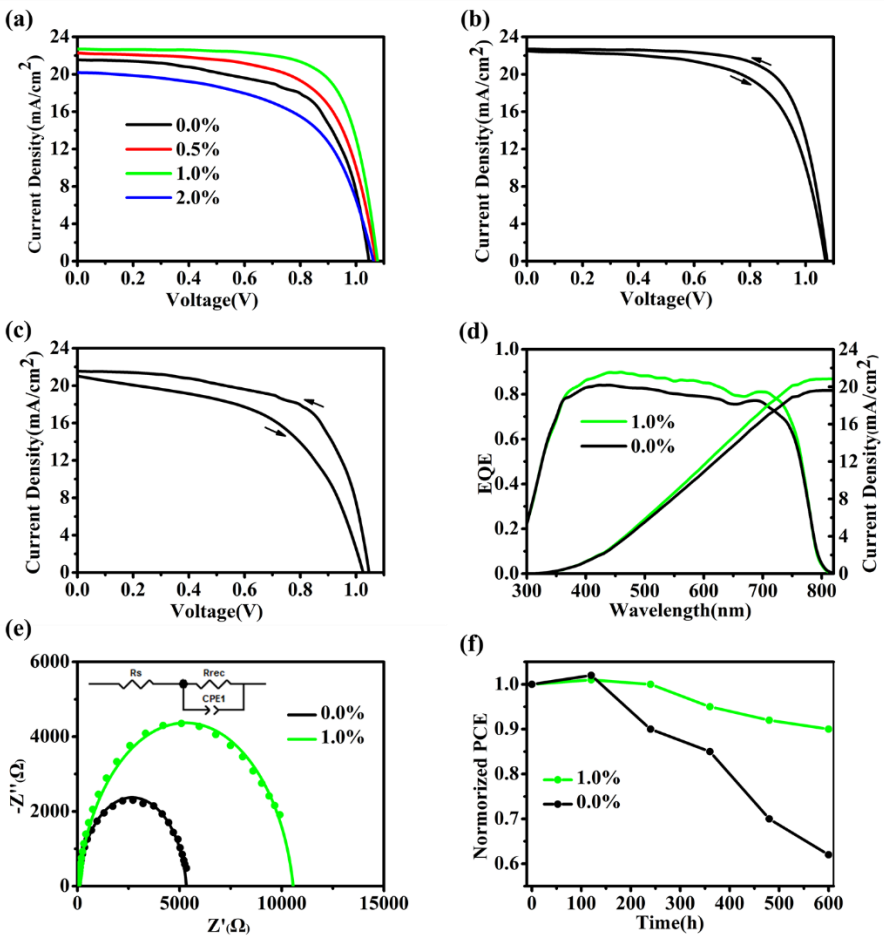

Figure 4.9. (a) The J−V curves of different molar ratio Mg doped $MAPbI_3$ perovskite solar cells measured under AM 1.5 solar illumination (100 mW•cm^{-2}) in air. The scanning direction is from open-circuit voltage to short-circuit current (reverse). (b) J−V curves of 1.0% Mg doped perovskite solar cell under reverse and forward voltage scans. (c) J−V curves of pristine $MAPbI_3$ perovskite solar cell under reverse and forward voltage scans. (d) EQE spectra of the pristine and 1.0% Mg doped perovskite solar cells measured in air. (e) Nyquist

plots along with the equivalent circuit diagram of pristine and 1.0 % Mg doped perovskite solar cells measured at 0.7 V applied bias under dark condition. Solid lines are the fitted curves and the experimental data are shown as points. (f) The stability of pristine and 1.0% Mg doped perovskite solar cells. Devices were prepared without sealing and were kept under dark at 30~40% RH atmosphere.

The defect states and band bending always affects the hysteresis of the J-V curves which is a significant problem for conforming the actual PCE. Hence, to compare the quality of the PSCs, the hysteresis index values are calculated from the measured current-density-voltage curves.[43] The hysteresis index value of 1.0 % Mg doped perovskite device is 0.11 which is lower than that of pristine device (0.27). The lower hysteresis index could be owning to the big grain size and uniform growth of the perovskite layer, effectively reducing the grain boundaries and make the charge transfer more efficiently between grains. Figure 4.9d shows the IPCE curve and the corresponding calculated short-circuit current. 1.0 % Mg doped perovskite device showed higher EQE curve than the pristine device which is attributed to higher absorbance intensity of the 1.0 % Mg doped perovskite film. Electrochemical impedance spectroscopy was performed to investigate the charge transfer mechanism on the interfaces. Figure 4.9e shows the Nyquist plots of the pristine and 1.0% Mg doped PSCs measured under dark condition with a bias of 0.7 V. Rs, Rrec and CPE are the sheet resistance, recombination resistance and constant phase element, respectively. As it is known that lower Rs suggests a better electro transport and larger Rrec implies the lower recombination rate.[44] From the fitting, Rrec increased from 5303 Ω to 10545 Ω after 1.0 % MgI_2 has been incorporated, suggesting the recombination rate is decreased.[24] Therefore, it can be concluded that the larger Rrec of 1.0 % Mg doped perovskite based device indicates that the

carrier mobility in correspondent device is improved thus leading to enhanced V_{oc} and FF. Furthermore, air stability of pristine and 1.0 % Mg doped PSCs were evaluated which was shown in Figure 4.9f. All the devices prepared without encapsulation was stored at room temperature at 30~40% RH atmosphere. After 600 h, the efficiency of pristine device decreased to 60 % of its initial value. However, the 1.0 % Mg doped device showed excellent stability in high humidity condition where 90 % of the original PCE was still retained. The more stable Mg doped perovskite device is possible reason for the stability of the Mg doped perovskite layer as proved by the perovskite film stability test shown in Figure 4.10. It is clear from Figure 4.10 that the 1.0 % Mg doped perovskite layer was stable as the UV absorbance showed nearly no decrease after two weeks while the pristine film showed significant decrease.

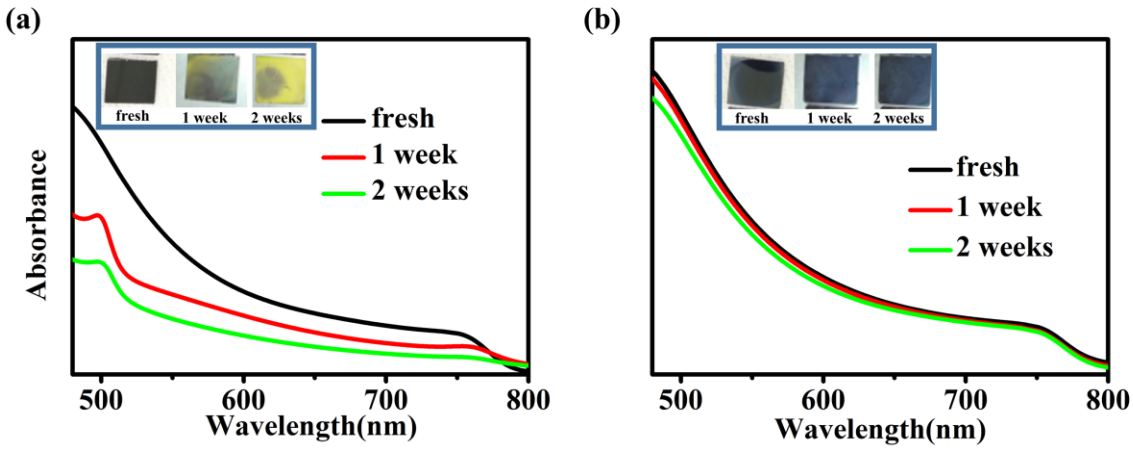

Figure 4.10 The stability of doping free and 1 % Mg doping perovskite film on the glass substrates. The films were prepared and kept at 30~40% RH atmosphere. The insert is the photograph of the corresponding perovskite films. (a) Doping free perovskite film. (b) 1.0 % Mg doping perovskite film.

4.4 Conclusion

In conclusion, we have successfully doped Mg into $MAPbI_3$ without altering the crystal structure. The MgI_2 doping resulted in lower conduction and valence band, perfectly matching with the conduction band of TiO_2 and valence band of spiro-OMeTAD. Higher quality perovskite films with bigger grain and pin-hole free was obtained upon Mg doping. For pristine device, the efficiency was 14.2 % compared to 17.8 % for 1 % Mg doped sample. Moreover, the PCE only dropped 10% after storage in 30~40 % relative humidity for 600 h. Our results suggest that doping Mg into perovskite layer is a good strategy to enhance stability and the photovoltaic performance of the perovskite solar cells.

Chapter 5. Pyreneammonium Iodide additive into $MAPbI_3$ perovskite layer in the humid air

5.1 Introduction

Methyl ammonium lead iodide ($MAPbI_3$) and other perovskite materials still showed poor performances against humidity, heat and light soaking.[101] Moreover, other additional degradation by UV irradiation, molecular oxygen also restrict the performances.[102-104] Therefore, research in the area for designing more stable PSCs is highly necessary. Recently, it has been reported that two-dimensional (2D) PSCs exhibited the high stability. These 2D perovskites are described as $(RNH_3)_2(MA)_{n-1}Pb_nI_{3n+1}$ (where RNH_3 usually is PEA= $C_6H_5(CH_2)_2NH^{3+}$, BA=n-butylammonium) as absorbers in PSCs.[105-108] Despite the high stability, the efficiency of 2D PSCs is still lower than 3D PSCs. To solve this problem, 2D/3D stacking structures, which have both advantage of 2D and 3D perovskite materials were reported.[109-115] Stabilities of PSCs was enhanced with notable efficiency by introducing a thin 2D perovskite layer because these 2D perovskites would wrap the grain boundary and surface of 3D perovskites. However, most exploited 2D/3D perovskites are based on PEAI and BA organic compound, which prevent the research progress of the 2D/3D perovskites. In addition, there are many organic compound with functional group which could be useful for introducing into the perovskite layer to make the perovskite layer functional. Therefore, it is challenging and meaningful for researchers to find novel functional organic materials for the 2D/3D perovskite materials.

Herein, we introduced a new organic compound, 1-(ammonium acetyl)pyrene (PEY) as the 2D cation for preparing a new 2D/3D hetero structure. The 2D/3D perovskite has the advantage of both the longtime stability of 2D perovskite and excellent carrier's transport of

the 3D perovskite, showed nearly no degradation after more than 6 months kept in ~60% RH air atmosphere. While the normal 3D $MAPbI_3$ perovskite layer quickly degraded within two weeks. Moreover, the $(PEY_2PbI_4)_{0.02}MAPbI_3$ 2D/3D perovskite film showed nearly no degradation upon 60 minutes UV-Ozone treatment, which indicated the high resistance of the UV light and molecular oxygen. Furthermore, the best planar solar cell of $(PEY_2PbI_4)_{0.02}MAPbI_3$ 2D/3D perovskite devices showed a high efficiency of 14.7 % with nearly no hysteresis, and ultra-stable PSCs with no efficiency loss than 3D PSCs after kept in ~60% RH air atmosphere for more than 400 hours.

5.2 Experimental section

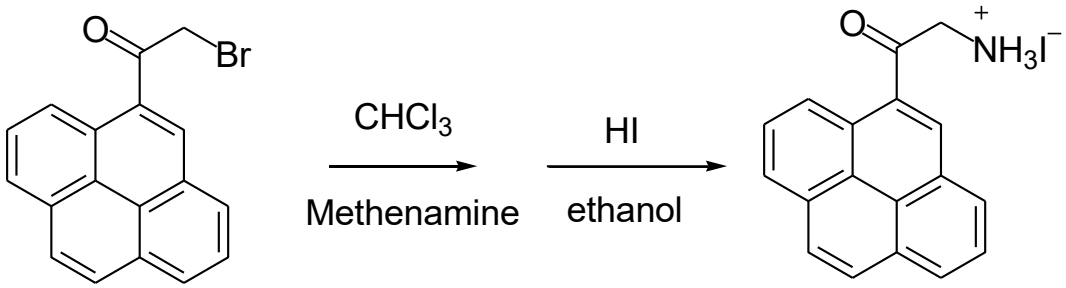

Scheme 5.1. Synthetic route of PYEHI

5.2.1 Synthesis of PYEHI

Scheme 5.1 shows the synthetic route of PYEHI. 4.0 g 1-(Bromoacetyl)pyrene (Aldrich, 97%) , 1.9 g hexamethylenetetramine(Aldrich, 99%) were added into 60 ml chloroform (Aldrich, 99%) in a round-bottom flask. The solution was stirred at room temperature for 12h. The precipitate was filtered and washed with chloroform 3 times to get the slight white solid. The solid was directly added into 100 ml ethanol (TCI, 99.5%). Then 6 ml hydriodic acid (Aldrich, 57 wt. % in water) was slowly added into the solution. The solution was stirred at 45 ºC for 4 h and then cooled at room temperature. The precipitate was filtered. After washing

with ethanol, acetone, and diethyl ether, compound PYEHI was obtained as a slight white solid. ESI-MS (m/z): calcd. [M^+] for $[C_{18}H_{14}NO]^+$ 260.11, found 260.11. Elemental analysis: calcd, C, 55.83, H, 3.64, N, 3.62. Found, C 56.87, H, 3.81, N, 3.66.

5.2.2 Preparation of perovskite solar cells

Fluorine-doped tin oxide (FTO glass, Nippon Sheet Glass Co. Ltd) substrates were etched with r hydrochloric acid solution and zinc powder. Tin (II) chloride (Aldrich, 98 %) was dissolved in ethanol (Wako, 99.8 %) to form 0.1 M $SnCl_2$ solution. Then the $SnCl_2$ solution was spin-coated on the cleaned FTO glass at 2000 rpm for 30 seconds. The substrate was annealed at 180 °C for 60 minutes on a hot plate to form a dense SnO_2 electron transport layer. The perovskite solution was prepared by dissolving 239 mg MAI (TCI, 98 %) and 692 mg PbI_2 (TCI, 99.99 %) into 0.2 mL dimethyl sulfoxide (DMSO, Aldrich, 99.8 %) and 0.8 mL dimethylformamide (DMF, Aldrich, 99.8 %) to achieve 1.5 M $MAPbI_3$ perovskite precursor solution. For preparing the 2D/3D perovskite precursor solution, keeping the PbI_2 at 1.5M and adding a proper PYEHI and MAI into 0.2 mL dimethyl sulfoxide (DMSO, Aldrich, 99.8 %) and 0.8 mL dimethylformamide. The Spiro-MeOTAD solution was prepared by mixing 72.3 mg Spiro-MeOTAD (Aldrich, 99 %), 28.8μL tert-butylpyridine (Aldrich, 96 %) , 17.5 μL Li-TFSI (Aldrich, 99.95 %) (520 mg/mL in acetonitrile) and 29 μL FK209 (Aldrich, 99 %) (300 mg/mL in acetonitrile) in 1 mL chlorobenzene solution. The perovskite layer was prepared on the Compact SnO_2 substrate by adding 0.1 mL perovskite precursor solution and spin-coated at 4000 rpm for 25 s. 0.5 mL ethyl acetate (99.8 %, Aldrich) antisolvent was dripped during the spin-coated progress.[86] The spin-coated perovskite film

was annealed at 100 °C for 10 min. The Spiro-MeOTAD layer spin-coated on the perovskite layer at 4000 rpm for 30 s. Finally, Au electrode with 80 nm thickness was deposited on the Spiro film by thermal evaporation.

5.2.3 Characterization

Solar cell performance was measured by a solar simulator (CEP-2000SRR, Bunkoukeiki Inc., AM 1.5G 100 $mWcm^{-2}$) and a mask with exposure area 0.10 cm^2 was used during the photovoltaic measurements with a 0.1 V/s scanning rate in reverse (from the open-circuit voltage (Voc) to the short-current density (Jsc)) and forward (from Jsc to Voc) modes under standard global AM 1.5 illumination. The IPCE spectra were recorded using a monochromatic Xenon lamp (Bunkouki CEP-2000SRR). X-ray Diffraction (XRD) Study. The surface morphology of the samples was observed through a scanning electron microscope (SEM) (JEOL, Neoscope, JCM-6000) and a Bruker Innova atomic force microscopy (AFM) (JSPM-5200). The XRD patterns were obtained by a Rigaku Smartlab X-ray diffractometer with monochromatic Cu-Kβ irradiation (45 kV/200 mA). The UV-Vis measurement was performed using a JASCO V-670. Spectrophotometer. Photoelectron yield spectroscopy (PYS) was used to determine the valence band using a Bunkoukeiki KV205-HK ionization energy measurement system with – 5.0 V of applied voltage under 10^{-4} Pa vacuum.

5.3 Results and discussion

In this chapter, the composition of $(PEY_2PbI_4)_xMAPbI_3$ (x: 0, 0.02, 0.05, and 0.10) is abbreviated as 2D/3D-X, i. e. $(PEY_2PbI_4)_{0.02}MAPbI_3$ is abbreviated as 2D/3D-0.02. Figure 5.1 shows the X-ray diffraction (XRD) patterns 2D/3D-X (x: 0 0.02, 0.05, and 0.10) perovskite films with different PEY content on glass substrates. All the films were prepared in an around 60% RH open air condition. In all 2D/3D-X, strong diffraction peaks located on 14.1°, 28.4° and 31.9° for the 2θ scan were absorbed and they correspond to the planes of (110), (220) and (222), which is in coincident to the previous reports.[21, 87, 116] The result conformed that all the films of 2D/3D-X contain highly crystalized perovskite phase.[35-36] Furthermore, a weak diffraction pattern of PbI_2 appeared at around 12.7 ° in 2D/3D-0 films and the intensity of the peak decreased with an increase in x from 0 to 0.1. The 2D peaks appeared at 6.6° and 9.2° were observed in 2D/3D-0.10. These peak intensities decreased as x decreases from 0.1 to 0 (Figure 5.2). It was noted that the increased concentration of PEY resulted in the completed PbI_2 transformation. This maybe owning to the enhanced humidity resistance of 2D layer, which prevent MAI and PbI_2 from the moisture in the spin-coating progress.

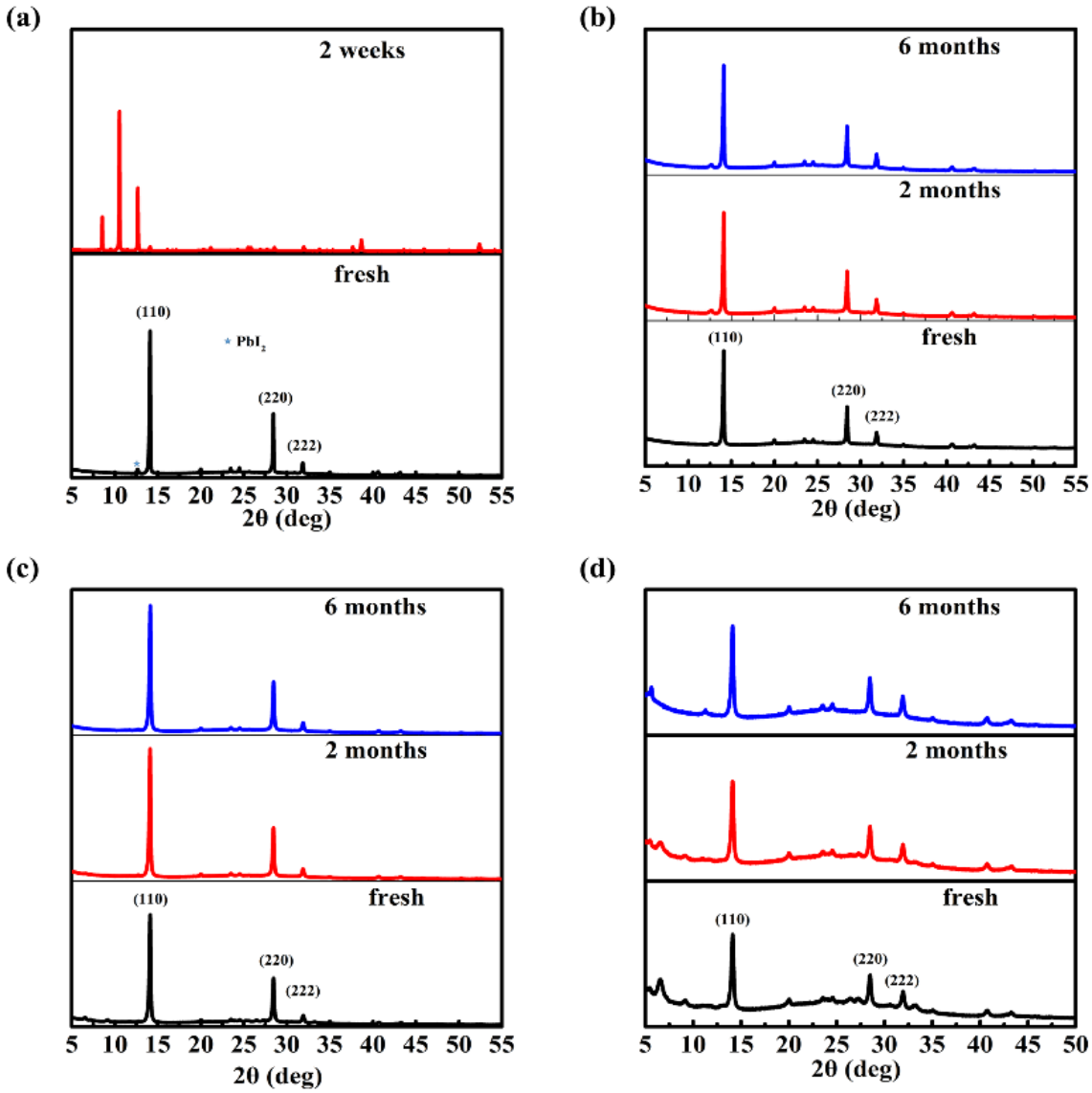

Figure 5.1. X-ray diffraction of 2D/3D-X (X: 0, 0.02, 0.05, 0.10) perovskite film on glass substrate. The samples was stored in ~60% RH humidity at ambient atmosphere in the dark condition without encapsulation. (a) 2D/3D-0 (b) 2D/3D-0.02 (c) 2D/3D-0.05 (d) 2D/3D-0.10.

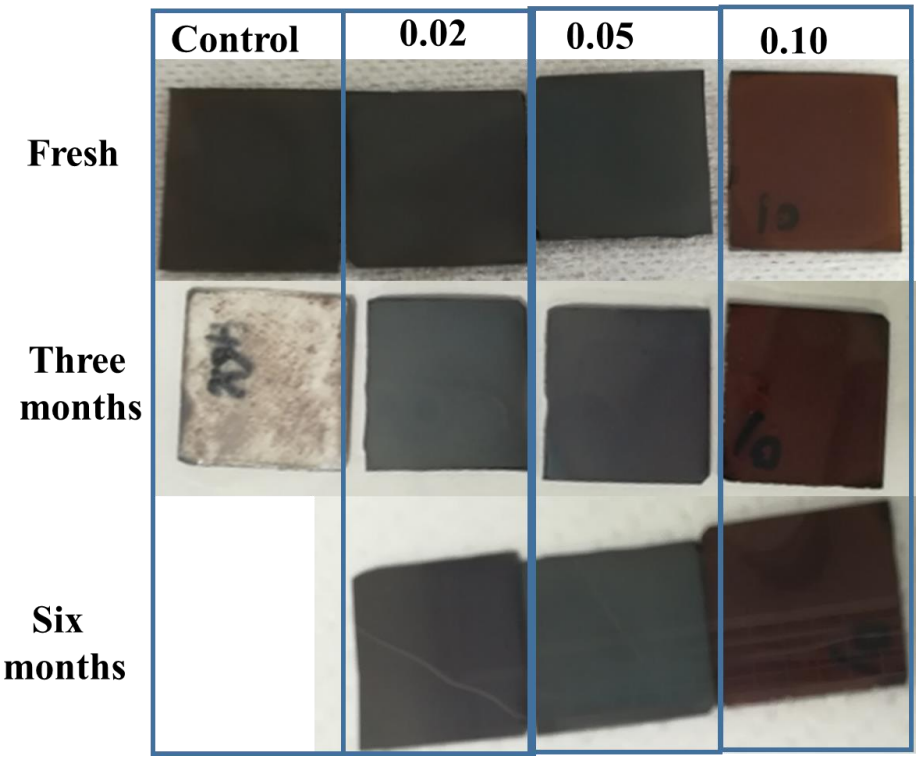

Figure 5.2. The perovskite films after kept at ambient atmosphere at different time.

The stability the 2D/3D-X films were tested by tracing the variation of the XRD patterns. Change of XRD patterns after storage in air atmosphere is also summarized in Figure 5.1. As shown in Figure 5.1a, for 2D/3D-0, peak at (110) of $MAPbI_3$ became very weak after the sample was stored in two weeks. In addition, several peaks appeared, one of which is 12.7 ^{o} assigned as PbI_2. This indicates the 3D $MAPbI_3$ perovskite started to decompose immediately after exposed to open air because of loss of MA. In contrast, as shown in Figure 5.1b, c, d, for 2D/3D-0.02, 2D/3D-0.05, 2D/3D-0.10, peak at (110) of 3D $MAPbI_3$ did not change after more than 6 months, leading to the conclusion that only 0.02 addition of PEY can greatly enhance the stability of these perovskite layers. The UV-vis spectra of the 2D/3D-X perovskite film tested by different time also clearly exhibits the enhanced stability of the perovskite layer by PEY incorporation. As shown in Figure 5.3, the UV absorption decreased

totally for $MAPbI_3$ perovskite film within two weeks. However, for keeping at about 60% RH atmosphere for more than 6 months, almost no difference of the absorption intensity can be detected for the 2D/3D-x (x= 0.02, 0.05, 0.1) perovskite films, which showed the excellent moisture stability of the materials. The insert optic figures of the perovskite films show 2D/3D-x (x= 0.02, 0.05, 0.1) perovskite films kept as a shining film after even more than 6 months.

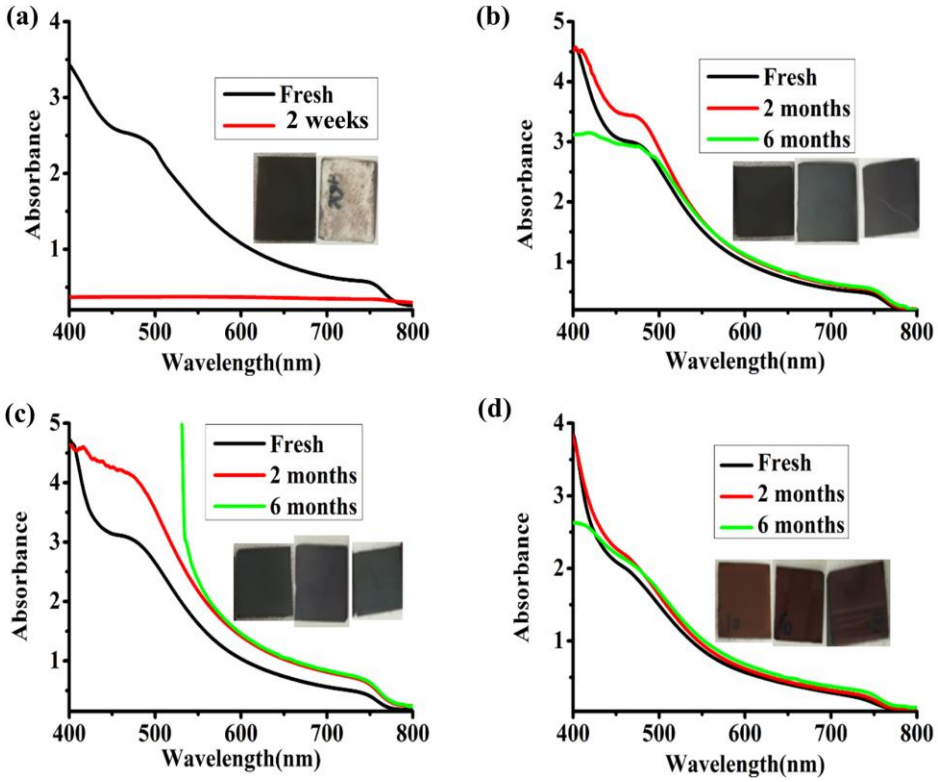

Figure 5.3. UV-vis spectra of 2D/3D-X (X: 0, 0.02, 0.05, 0.10) perovskite film on glass substrate. The samples was stored in ~60% RH humidity at ambient atmosphere in the dark condition without encapsulation. (a) 2D/3D-0 (b) 2D/3D-0.02 (c) 2D/3D-0.05 (d) 2D/3D-0.10.

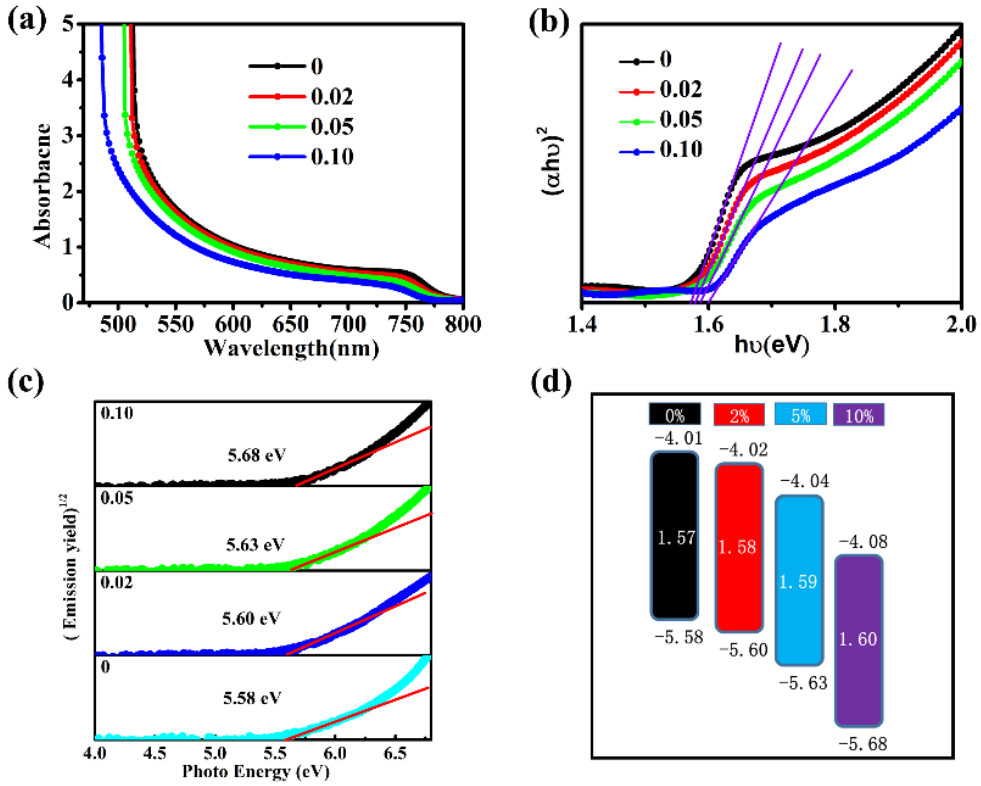

Figure 5.4. (a) The UV-vis absorption spectra for 2D/3D-X (b) (ahv)2 versus energy for 2D/3D-X (x, 0, 0.02, 0.05, 0.10) perovskite films on FTO glass substrates. (c) The PESA for the for 2D/3D-X (x, 0, 0.02, 0.05, 0.10) perovskite films on FTO glass substrates. (d) Corresponding electronic structure diagrams of for 2D/3D-X (x, 0, 0.02, 0.05, 0.10) perovskite.

Figure 5.4a showed the light absorption spectra for 2D/3D-X (x, 0, 0.02, 0.05, 0.10) perovskite films on FTO glass substrates. It was found that the absorbance intensity decreased and the absorption edge blue-shifted as x increased from 0 to 0.10. Meanwhile, Eg shifted from 752 nm (1.57 eV) for 2D/3D-0 to 735 nm (1.60 eV) for 2D/3D-0.10 as shown in Figure 5.4b. These results shows that 2D structure is created in the 3D structure. The valence band edge was shifted from -5.58 eV for 2D/3D-0 to more negative values of -5.60 eV, -5.63 eV, and -5.68 eV for 2D/3D-0.02, 2D/3D-0.05, and 2D/3D-0.10, respectively, as

determined by photoelectron spectroscopy (Figure 5.4c). The observation is in agreement of conventional consideration that predict destabilization of valence band.[117] Figure 5.4d summarizes shift of conduction band and valence band which were obtained from the valence band energy level and optical absorption edge. It is clear shown in Figure 5.4d that the electronic configuration of $MAPbI_3$ suffers only minor changes when 2D structure was introduced low content 2D, which is critical in terms of keeping high photovoltaic performance of the $MAPbI_3$ 3D perovskite materials.

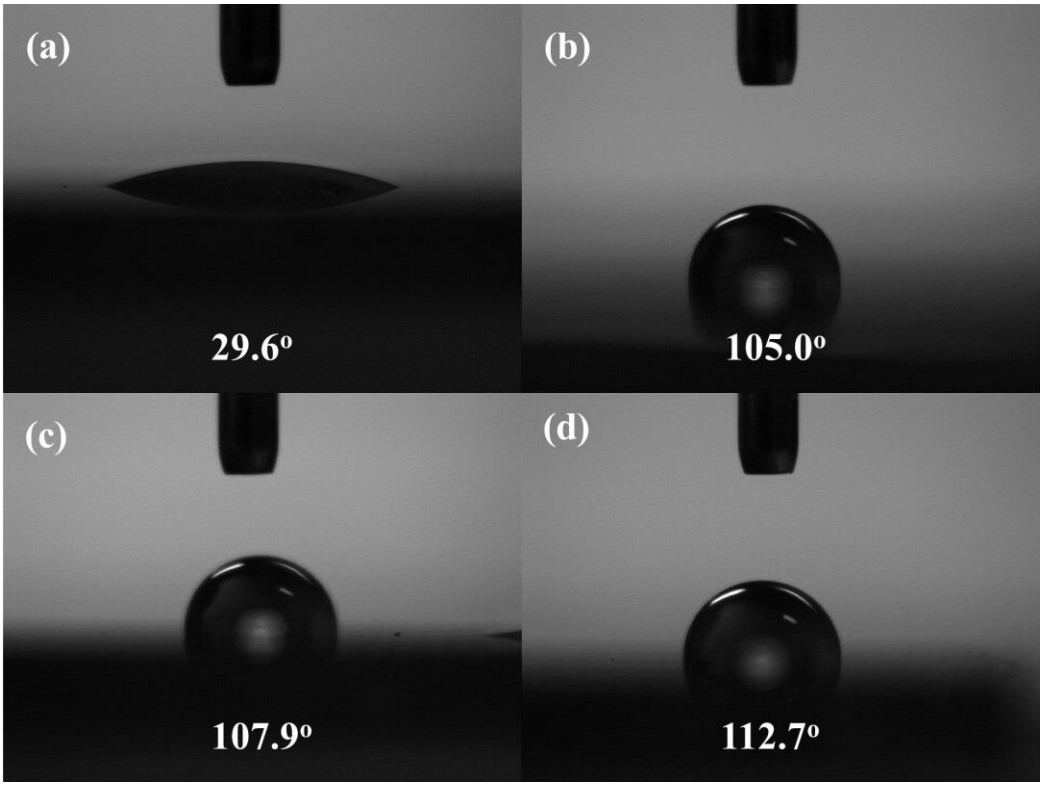

Figure 5.5. Contact-angle test for the $(PEY_2PbI_4)_xMAPbI_3$ (0, 0.02, 0.05, 0.10) perovskite film with water droplets. (a) $MAPbI_3$; (b) $(PEY_2PbI_4)_{0.02}MAPbI_3$; (c) $(PEY_2PbI_4)_{0.05}MAPbI_3$; (d) $(PEY_2PbI_4)_{0.10}MAPbI_3$.

Next, the contact angle tests were used to test the water resist ability of 2D/3D-X films. The water contact angle of 2D/3D-0 film was 29.6°. This contact angle was increased to 105°, 107.9°, and 112.7° for 2D/3D-0.02, 2D/3D-0.05, 2D/3D-0.10, respectively, as shown in Figure 5.5. These results would be explained by the water repelling behavior of PEY, which was introduced in the 3D perovskite. The high moisture resistance could be owing to the high hydrophobicity of the pyrene group.

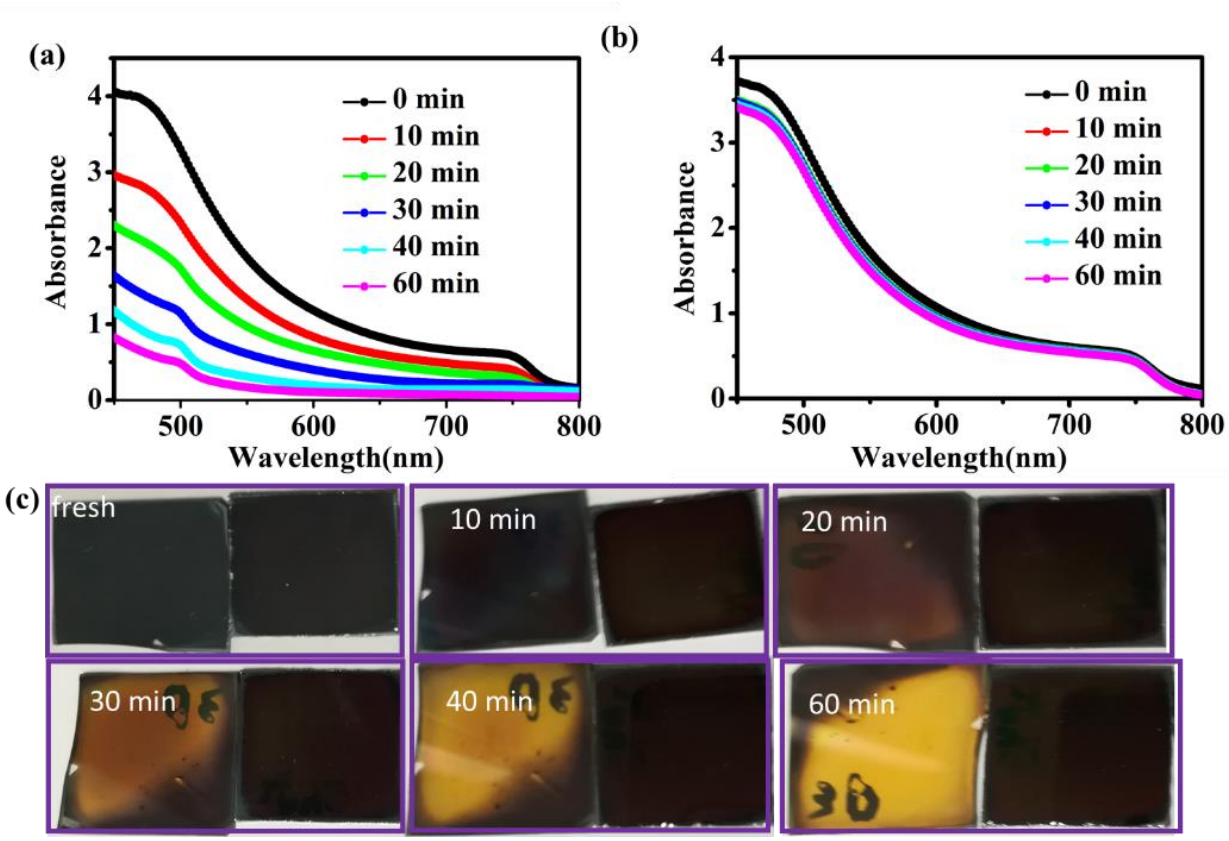

Figure 5.6. The UV-vis spectra of 2D/3D-0, (b) 2D/3D-0.02, (c) Color change of perovskite film after UV Ozone treatment. Left: 2D/3D-0, Right 2D/3D-0.02.

As perovskite can be easy degraded by UV irradiation and molecular oxygen. Therefore, UV Ozone machine was utilized to test the stability of the 2D/3D-X perovskite film which

shown in Figure 5.6. The UV-vis absorbance gradually decreased when 2D/3D-0 film was exposed to UV Ozone treatment as shown in Figure 5.6a. However, there was nearly no change of the UV-vis absorbance for 2D/3D-0.02 after the films was exposed to UV Ozone for more than 60 minutes as shown in Figure 5.6b. From the color of the perovskite film we can clear see that after 60 minutes, the 2D/3D-0 perovskite film change from dark to yellow slightly. While for the 2D/3D-0.02 perovskite, the film color showed nearly no change. The corresponding XRD of color changed perovskite films after UV Ozone treatment are shown in Figure 5.7. These results show the enhanced stability against light irradiation and oxidations for the film consisting of PEY.

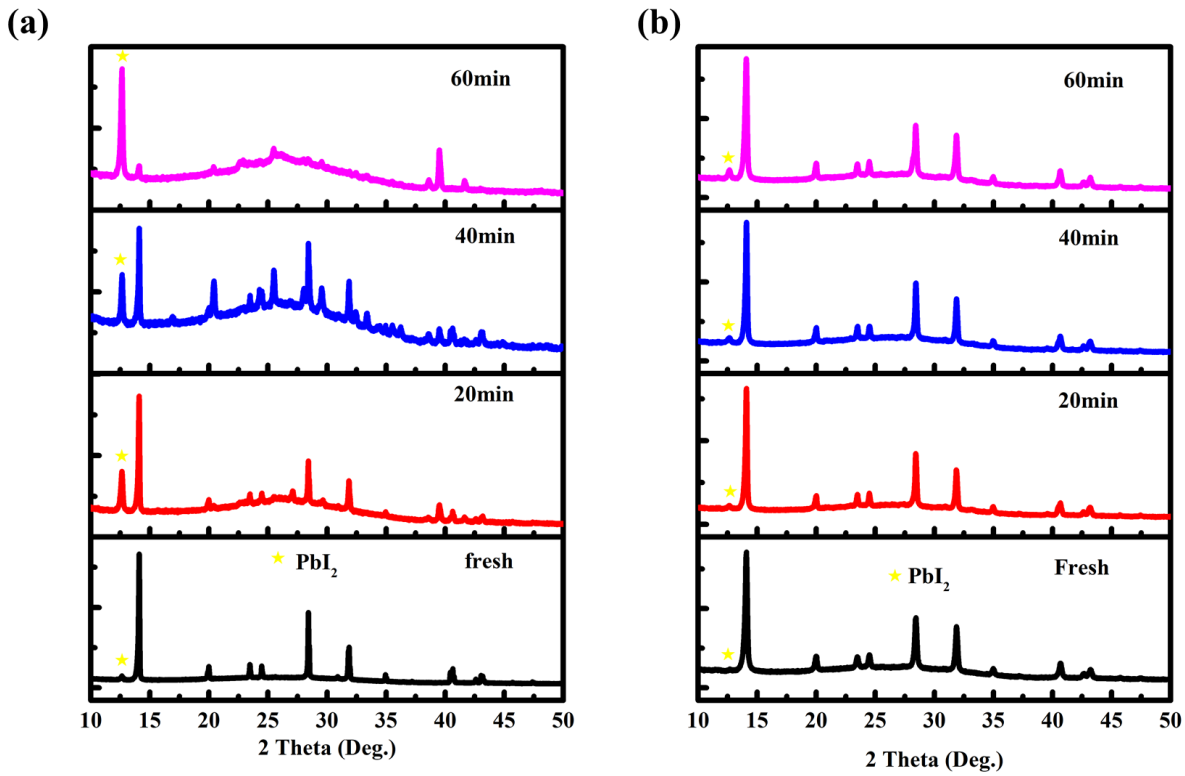

Figure 5.7. X-ray diffraction of (a) 2D/3D-0 and (b) 2D/3D-0.02 perovskite film under UV Ozone treatment for different time.

Figure 5.8 showed the surface morphology of 2D/3D-X (x= 0, 0.02, 0.05, 0.10) film on FTO/compact SnO_2 substrate. All the films showed a dense pinhole free morphology. However, there was a lot PbI_2 residue on surface of $MAPbI_3$ perovskite film, which was shown the white spot in Figure 5.8a.[118] Thelakkat and coworkers proved that the rate of degradation of $CH_3NH_3PbI_3$ could be accelerated because of PbI_2 residue present in the perovskite film.[88] Moreover, researchers have proved that the surface defects and trap state density originate from the uncoordinated Pb atoms of the residue PbI_2 which would limit the performances of PSCs.[89] As shown in Figure 5.8b, c and d, these residues were not observed in 2D/3D-X (x=0.02, 0.05, 0.10). These results were in consistent of the XRD date shown in Figure 1. The grain size was decreased gradually with the increase in X value of 2D/3D-X, as shown in Figure 5.8e-h. The statistical grain size for the perovskite films is shown in Figure 5.9.[57]

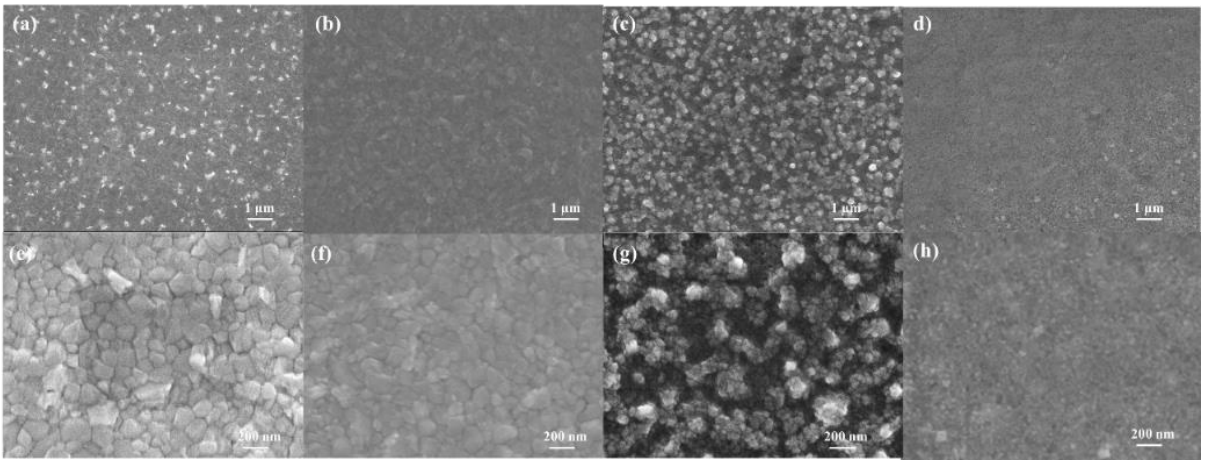

Figure 5.8. 2D/3D-X perovskite film on FTO substrates. (a)(e) 2D/3D-0; (b) (f) 2D/3D-0.02; (c) (g) 2D/3D-0.05; (d) (h) 2D/3D-0.10.

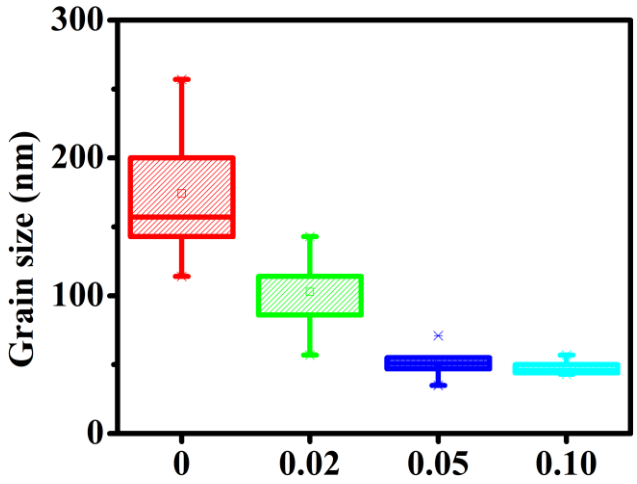

Figure 5.9. The statistical distribution of the particle size for **$(PEY_2PbI_4)_xMAPbI_3$** (0, 0.02, 0.05, 0.10) perovskite film.

To investigate the effect of 2D/3D perovskite on the photo voltaic performance, the planar PSCs using SnO_2 as the electron transport layer and 2,2`,7,7`-tetrakis (N,N-di-p-methoxyphenylamino)-9,9-spirobifluorene (spiro-OMeTAD) as the hole transport layer as shown in Figure 5.10a. These results are summarized in Figure 5.10b, c and d. The champion PCE of 2D/3D-0 devices was 15.0 % with J_{sc} of 21.85 mA/cm^2, V_{oc} of 1.01V and FF of 68.2 %. The performance of 2D/3D-0.02 showed equal compared with the 2D/3D-0 perovskite with a champion PCE of 14.7 %, with J_{sc} of 21.15 mA/cm^2, V_{oc} of 1.05 V and FF of 66.1 %. The Jsc and FF of the 2D/3D-0.02 devices were slightly lower than 2D/3D-0 devices which may be owing to the reduced charge mobility of the 2D perovskite.[119-121] The V_{oc} of 2D/3D-0.02 was higher than that of 2D/3D-0 maybe owing to the increased bandgap. Hysteresis index (HI) values were calculated from the J-V curves.[86] A modified hysteresis index (HI) values is defined. The HI value of 2D/3D-0.02 was 0.02, which was less than 2D/3D-0 (HI, 0.21). This result shows introduction of PEY was able to eliminate effectively hysteresis behaviors.

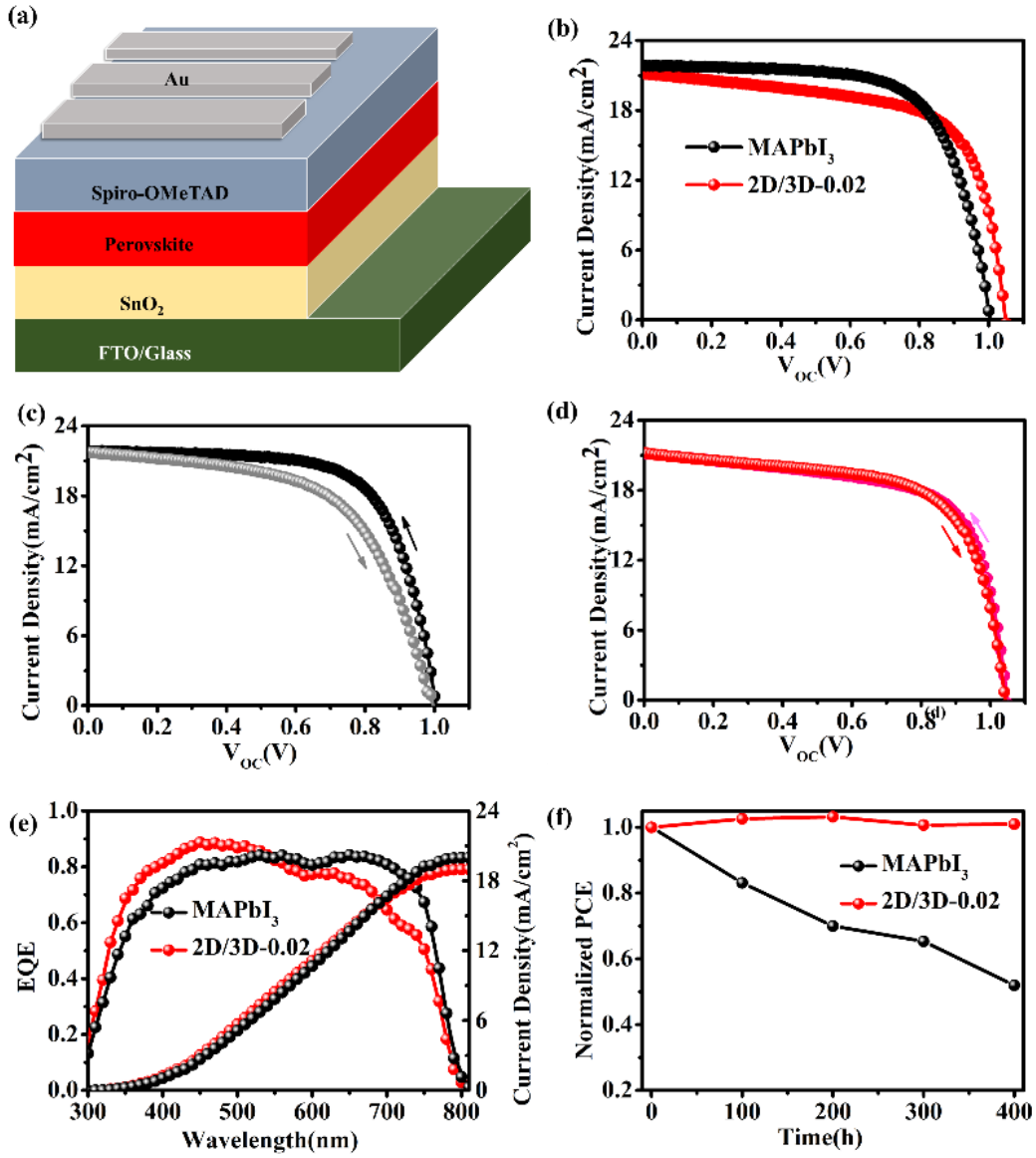

Figure 5.10. (a) Schematic structure of FTO/SnO_2/perovskite/Spiro-OMeTAD/Au planar perovskite solar cells. (b) J-V curves in reverse direction of 2D/3D-0 and 2D/3D-0.02 planar perovskite solar cells. (c) J−V curves of the champion 2D/3D-0 perovskite solar cell under reverse and forward voltage scans. (d) J−V curves of the champion 2D/3D-0.02 perovskite solar cell under reverse and forward voltage scans. (e) EQE spectra of 2D/3D-0 and2D/3D-0.02 planar perovskite solar cells. (f) Stability test for 400 h of the champion device under ambient atmosphere without sealing in dark condition under average humidity of around 60%.

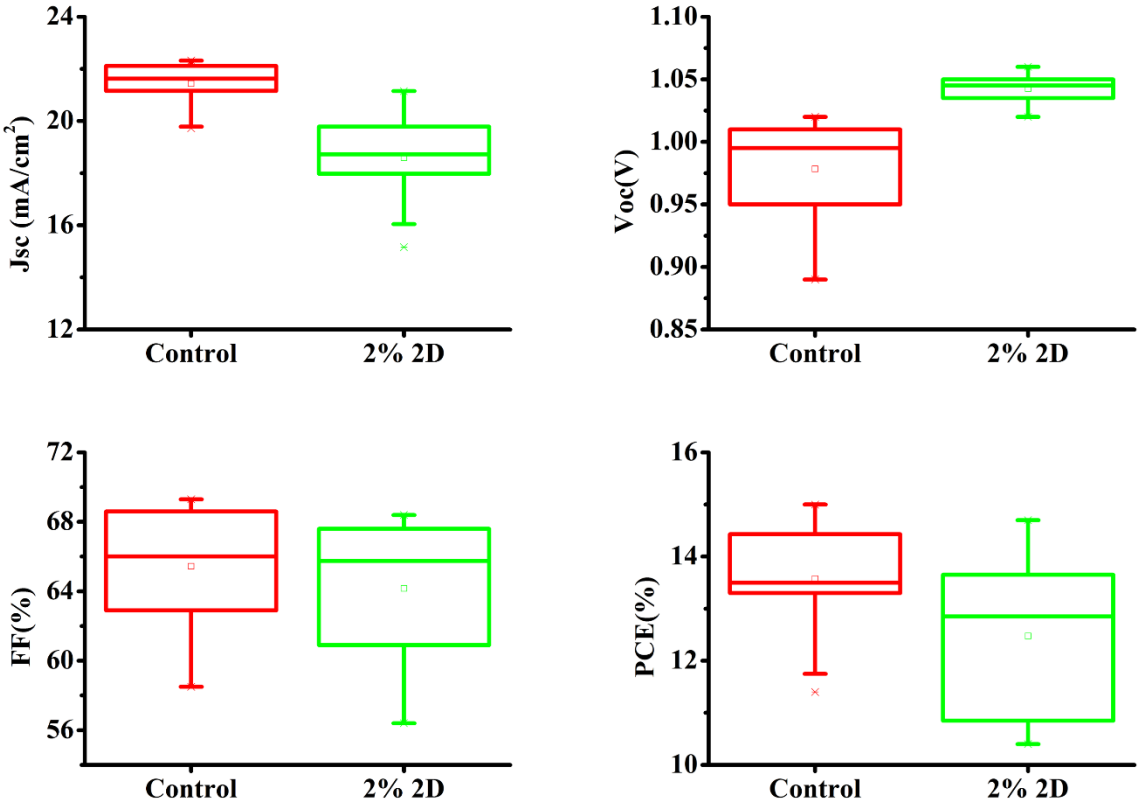

Figure 5.11. Photovoltaic statistics for the planar perovskite solar cells based on $MAPbI_3$ and $(PEY_2PbI_4)_{0.02}MAPbI_3$ materials. (a) J_{SC}, (b) V_{OC}, (c) Fill factor, (d) Efficiency. The boxes represent 40 data from the V_{OC}-to-J_{SC} scan direction.

Figure 5.10b, e show the J-V curves and the corresponding IPCE curves of the champion devices. The IPCE curve for 2D/3D-0.02 has higher value at short wavelength and lower at longer wavelength, compared with that for 2D/3D-0.02. This may be explained by the little lower absorption for 2D/3D-0.02 at 700-800 nm region, as shown in Figure 5.4a. The IPCE edge was about 800 nm, which is consistent to that of light absorption. Indoor environment stability for 2D/3D-0.02 and 2D/3D-0 were investigated as shown in Figure 5.10f. The

unsealed devices were stored in ~60% RH and dark air atmosphere. 2D/3D-0 device degraded to 51.6% of its initial efficiency after 400 hours. However, for 2D/3D-0.02 device, the PCE was still kept with no decline after 400 hours. From all the results, it was proved that 2D/3D-0.02 perovskite devices has enhanced stability with keeping the high efficiency of 2D/3D-0.

5.4 Conclusion

In conclusion, we have successfully introduced pyreneammonium iodide as the 2D layer for preparing the 2D/3D perovskite. The 2D/3D perovskite solar cell showed notable stability, which there is no degradation in ~60% RH humidity after 6 months. Moreover, the 2D/3D perovskite also showed a high UV stability which kept nearly no degradation after one hour in the UV Ozone treatment. The contact angel can reached beyond 100^{o} that is more 3.5 times than 2D/3D-0 perovskite layer (29.6^{o}). The champion efficiency of 2D/3D-0.02 perovskite solar cells is 14.7% which is almost equal to the performance of 2D/3D-0 devices (15.0%) with nearly no hysteresis. This work provides a novel concept for incorporating the functional organic compounds into the perovskite layer to enhance the solar cells` performance.

Chapter 6. All-Inorganic $CsPb_{1-x}Ge_xI_2Br$ Perovskite prepared in the humid air

6.1 Introduction

All the high performance organic-inorganic hybrid perovskite solar cells typically include the organic group (i. e. methylammonium (MA^+), formamidinium (FA^+)), which restrict the perovskite solar cells development as the poor stability of the organic cation under the thermal, moisture and oxygen influence.[122-124] All-inorganic perovskites can solve those problems on the instability of perovskite solar cells with organic cations.[125-127] Until now, all-inorganic perovskite based on cesium cation ($CsMX_3$) is the most exploited material with high thermal stability and good photovoltaic performance.[128-129] $CsPbI_3$, $CsPbI_2Br$, $CsPbIBr_2$, $CsPbBr_3$ (have ranged bandgaps from ~1.73 to ~2.3 eV) are the most studied materials for the photovoltaic application. $CsPbBr_3$ which shows a good phase stability but has a wide bandgap (~2.3eV) which is not appropriate for the solar cell.[130] On the other hand, $CsPbI_3$ and $CsPbI_2Br$ have narrower bandgap (~1.73eV and ~1.92eV), but they shows phase transition from α phase (cubic, black phase and active for photo-electric conversion) to δ phase (orthorhombic, yellow phase, inactive for photo-electric conversion) at room temperature.[131-134] Thus, inorganic perovskite with good phase stability and proper bandgap is desirable. Furthermore, the fabrication process of PSCs is usually performed in a glovebox filled with nitrogen/argon to avoid moisture, oxidation and other uncontrolled influence which restrict the commercial application of perovskite solar cells.[47-48] Thus, it is requested hopefully to prepare high-quality inorganic perovskite films in the humid ambient air in order to lower the cost of fabrication. Inorganic perovskite, $CsPbI_2Br$ that has a narrower bandgap

(~1.90 eV) than $CsPbBr_3$ and a better phase stability than $CsPbI_3$ is the most promising candidate material in the all-inorganic perovskite materials after balancing the bandgap and phase stability. However, the phase transition from cubic phase to orthorhombic phase occurs rapidly when kept in an uncontrolled air condition. Humidity has been proved to be the major issue for α phase stability of $CsPbI_2Br$.[135] Despite there are some reports on increasing the performance of $CsPbI_2Br$ based perovskite solar cells,[136-140] nearly none of them shows stability at high humidity condition. Furthermore, in most cases, the major component of the perovskite is still based on lead. Substitution of lead with less toxic material is significantly important as the use of lead is restricted in electronic devices according to the European regulations.[141] As far as we know there is no report regarding the preparation of $CsPbI_2Br$ based perovskite solar cells in ambient air condition at high humidity.

In this chapter, for the first time, we reports photovoltaic performances for $CsPb_{1-x}Ge_xI_2Br$ (x, 0, 0.1, 0.2, 0.3) prepared at low temperature (160 ^oC) in humid air condition. The cubic phase stability was greatly increased by the incorporation of germanium. When the inorganic perovskite film without germanium was stored under 50~60% relative humidity, cubic phase of perovskite was changed to yellow orthorhombic phase rapidly within 10 minutes. However, the cubic phase of the perovskite was still kept nearly no change after 120 h measurement for the $CsPb_{0.8}Ge_{0.2}I_2Br$ perovskite film. With the increasing germanium in the inorganic perovskite, the V_{OC} was greatly increased from 1.02 V of $CsPbI_2Br$, to 1.34 V of $CsPb_{0.7}Ge_{0.3}I_2Br$, which might be a record V_{OC} for $CsPbI_2Br$-based solar cells. In addition, the champion efficiency of 10.8% was obtained by the planar perovskite solar cell with a structure of FTO/SnO_2/$CsPb_{0.8}Ge_{0.2}I_2Br$/P3HT/Spiro/Au along with a high V_{OC} of 1.27 V. The stability of the solar cells was greatly increased with the parameters including short

circuit current, V_{OC}, fill factor and efficiency of $CsPb_{0.8}Ge_{0.2}I_2Br$ perovskite solar cells showed nearly no decay after measured for more than 7 hours in 50-60% RH humid air without encapsulation.

6.2 Experimental Section

6.2.1 Preparation of perovskite solar cells

All reagents including ethyl acetate (Aldrich, 99.8 %) and chlorobenzene (Aldrich, 99.8%) were used without further purification. F-doped SnO_2 (FTO glass, Nippon Sheet Glass Co. Ltd) substrates were first patterned and cleaned using zinc powder and 6 N hydrochloric acid solution. Tin (II) chloride (Aldrich, 98 %) was dissolved in ethanol (Wako, 99.8 %) to form 0.1 M $SnCl_2$ solution. Then the $SnCl_2$ solution was spin-coated on the cleaned FTO glass in turn at 2000 rpm for 30 seconds and 6000rpm 30s. The substrate was annealed at 180 °C for 60 minutes on a hot plate to form a dense SnO_2 electron transport layer. Proper molar ratio of CsBr (TCI, 98 %) and PbI_2 (TCI, 99.99 %) and GeI_2 (Aldrich, 99%) were dissolved in anhydrous dimethylformamide (DMF, Aldrich, 99.8 %) and anhydrous dimethyl sulfoxide (DMSO, Aldrich, 99.8 %) (DMF: DMSO, 3:7) to prepare 1.4 M $CsPb_{1-x}Ge_xI_2Br$ precursor solution. The perovskite precursor solution was spin-coated on SnO_2-coated substrate at 3000 rpm for 25 seconds and ethyl acetate (0.5 ml) was dripped on the substrate 15 seconds after starting the spin-coating process, followed by heating at 160 °C for 10 minutes. Then 5mg/mL P3HT(TCI, 99%) chlorobenzene solution was spin-coating at 4000rpm for 25 seconds and annealed at 160 °C for 10 minutes. The Spiro-MeOTAD layer was then prepared by spin-coating a chlorobenzene solution containing 180 mM Spiro-MeOTAD (Aldrich, 99 %), 60 mM tert-butylpyridine (Aldrich, 96 %), 30 mM Li-TFSI (Aldrich, 99.95 %) (520 mg/mL in acetonitrile) and 33 mM FK209 (Aldrich, 99 %) (300

mg/mL in acetonitrile) at 4000 rpm for 30 seconds. Finally, 80 nm-thick Au counter electrode was deposited by thermal evaporation. All procedures were performed at around 50%-60% relative humidity in ambient air condition (Relative humidity was recorded using a hygrometer accurate to ± 5 % RH between 25 % and 69.9 % RH, ±10 % RH between 70 % and 90 % RH) (A&D Company, AD-5681)).

6.2.2 Characterization

Solar cell performance was measured by a solar simulator (CEP-2000SRR, Bunkoukeiki Inc., AM 1.5G 100 $mWcm^{-2}$) and a mask with exposure area 0.10 cm^2 was used during the photovoltaic measurements with a 0.1 V/s scanning rate in reverse (from the open-circuit voltage (V_{OC}) to the short-current density (J_{SC})) and forward (from J_{SC} to V_{OC}) modes under standard global AM 1.5 illumination. The IPCE spectra were recorded using a monochromatic Xenon lamp (Bunkouki CEP-2000SRR). X-ray Diffraction (XRD) Study. The surface morphology of the samples was observed through a scanning electron microscope (SEM) (JEOL, Neoscope, JCM-6000). The XRD patterns were obtained by a Rigaku Smartlab X-ray diffractometer with monochromatic Cu-Kβ irradiation (45 kV/200 mA). The UV-Vis measurement was performed using a JASCO V-670. Spectrophotometer. Electrochemical impedance spectroscopic (EIS) measurements were performed in the dark using an electrochemical workstation with a frequency range from 1 Hz to 1 MHz at 0.7 V applied bias. Photoelectron yield spectroscopy (PYS) was used to determine the valence band using a Bunkoukeiki KV205-HK ionization energy measurement system with – 5.0 V of applied voltage under 10^{-4} Pa vacuum.

6.3 Result and discussion

Figure 6.1a shows XRD patterns of $CsPb_{1-x}Ge_xI_2Br$ with different Ge content (x, 0, 0.1, 0.2, 0.3). All the films were prepared on the glass substrates by one-step anti-solvent spin-coating method in ambient air condition with high humidity.[116] The film preparation process is illustrated in Figure 6.2. Strong diffraction peaks located at 14.6°, 20.8° and 29.5° were observed corresponding to the (100), (110) and (200) planes of cubic phase of $CsPbI_2Br$, which are in good agreement with previous reports.[142-144] These results indicate that all the $CsPb_{1-x}Ge_xI_2Br$ perovskite films are all highly crystallized perovskite phase. Meanwhile, a typical orthorhombic phase at 10.0° was found in the $CsPbI_2Br$ perovskite film.[135] In contrast, no peak assigned to the orthorhombic phase was observed upon incorporation of germanium into the perovskite, which is clearly shown in the zoomed image in Figure 6.3a. These results showed that the germanium addition directly increase the cubic phase stability of $CsPbI_2Br$. With addition of Ge, crystallite size calculated from XRD is decreased from 69.7 nm for x=0 to 35.3 nm for x= 0.1, 32.6 nm for x= 0.2, and 23.8 nm for x= 0.3. Top view scanning electron microscopy (SEM) images of the $CsPb_{1-x}Ge_xI_2Br$ films shown in Figure 6.4 exhibit obvious decreased crystal grain size which is in agreement with the XRD data. The reduced crystal size could induce lattice strain to stabilize the α phase of $CsPbI_2Br$.[128, 136] Atomic force microscopy (AFM) images in Figure S13 clearly show the smoother perovskite film for the $CsPb_{0.8}Ge_{0.2}I_2Br$ (Rq=3.0) compared to the pristine $CsPbI_2Br$ (Rq=15.2), which could enhance the performance of perovskite devices by providing better interfacial contact with the hole transport layer.

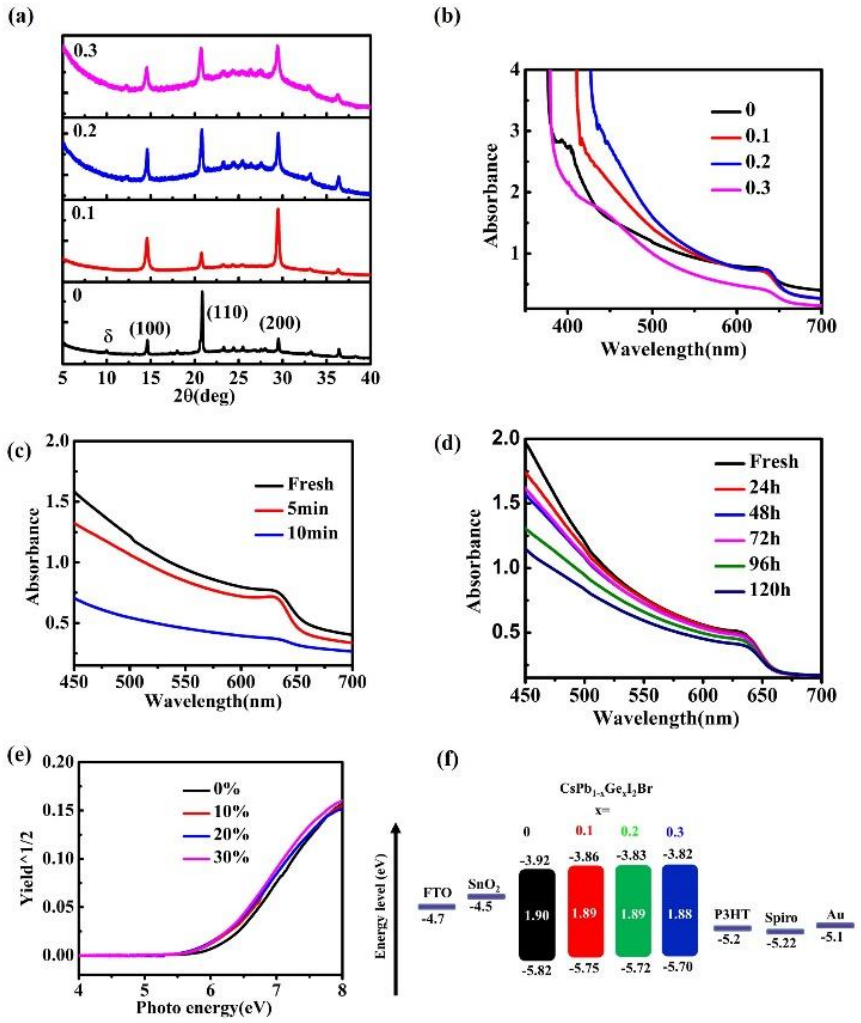

Figure 1. (a) XRD spectra of fresh $CsPb_{1-x}Ge_xI_2Br$ perovskite films on glass substrates(x, 0, 0.1, 0.2, 0.3) and the corresponding (b) UV-vis spectra. (c) UV-vis spectra of $CsPbI_2Br$ perovskite film measured in ambient air at 50~60% RH over a period of time. (d) UV-vis spectra of $CsPb_{0.8}Ge_{0.2}I_2Br$ perovskite film measured in ambient air at 50~60% RH over a period of time. (e) Photoelectron yield spectroscopy (PYS) measurement for $CsPb_{1-x}Ge_xI_2Br$ perovskite film (x, 0, 0.1, 0.2, 0.3) measured on FTO substrates. (f) Energy band diagram constructed from Uv-vis and PYS measurement.

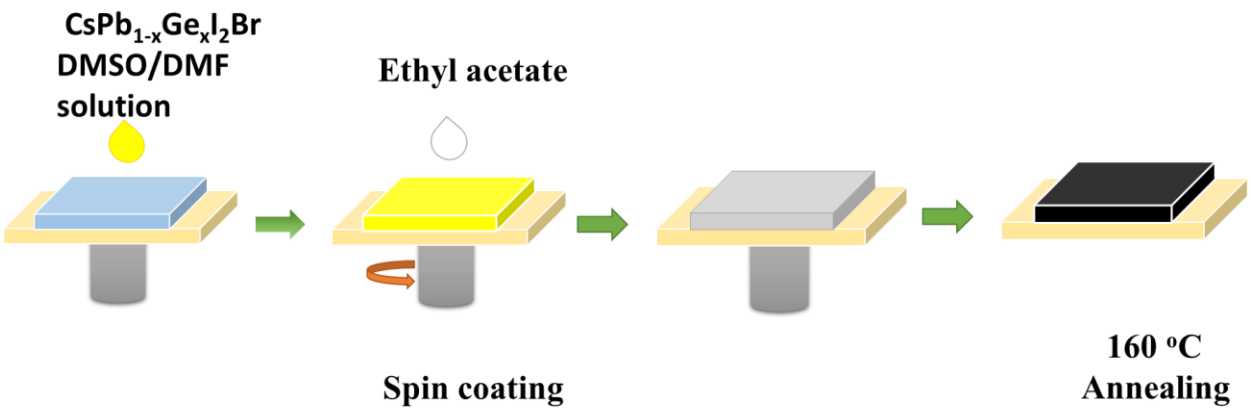

Figure 6.2. Schematic illustration of the one-step process using anti-solvent for fabricating perovskite films.

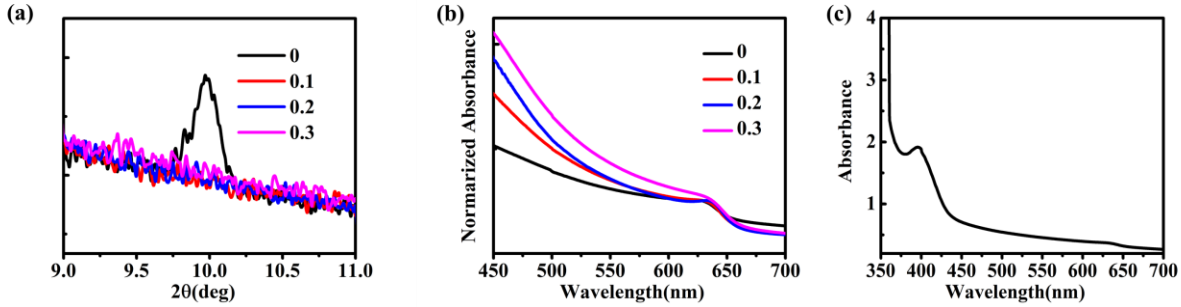

Figure 6.3. (a) Narrow scale for the δ phase from the XRD of the $CsPb_{1-x}Ge_xI_2Br$ perovskite film (x, 0, 0.1, 0.2, 0.3). (b) Namarized absoebance of $CsPb_{1-x}Ge_xI_2Br$ perovskite film. (c) UV-vis absorbance of $CsPbI_2Br$ perovskite film after kept in 50-60% RH humid air atmosphere for 10 minutes.

The optical properties of the $CsPb_{1-x}Ge_xI_2Br$ perovskite materials were evaluated by the UV-vis measurement, shown in Figure 6.1b. The absorption edges shifted to a slight longer wavelength as the germanium content increases which clearly shown in Figure 6.3b. The absorption intensity was increased as Ge content increased from 0, 0.1, to 0.2 and decreased at the Ge content of 0.3. The film stability of the perovskite film in 50-60% RH humid air atmosphere was measured and the results are shown in Figure 6.1c, d. For the $CsPbI_2Br$, the cubic phase absorption edge at around 630 nm decreased rapidly within 10 minutes. However,

for the $CsPb_{0.8}Ge_{0.2}I_2Br$ perovskite, the cubic phase absorption edge showed no change even after 120 hours.

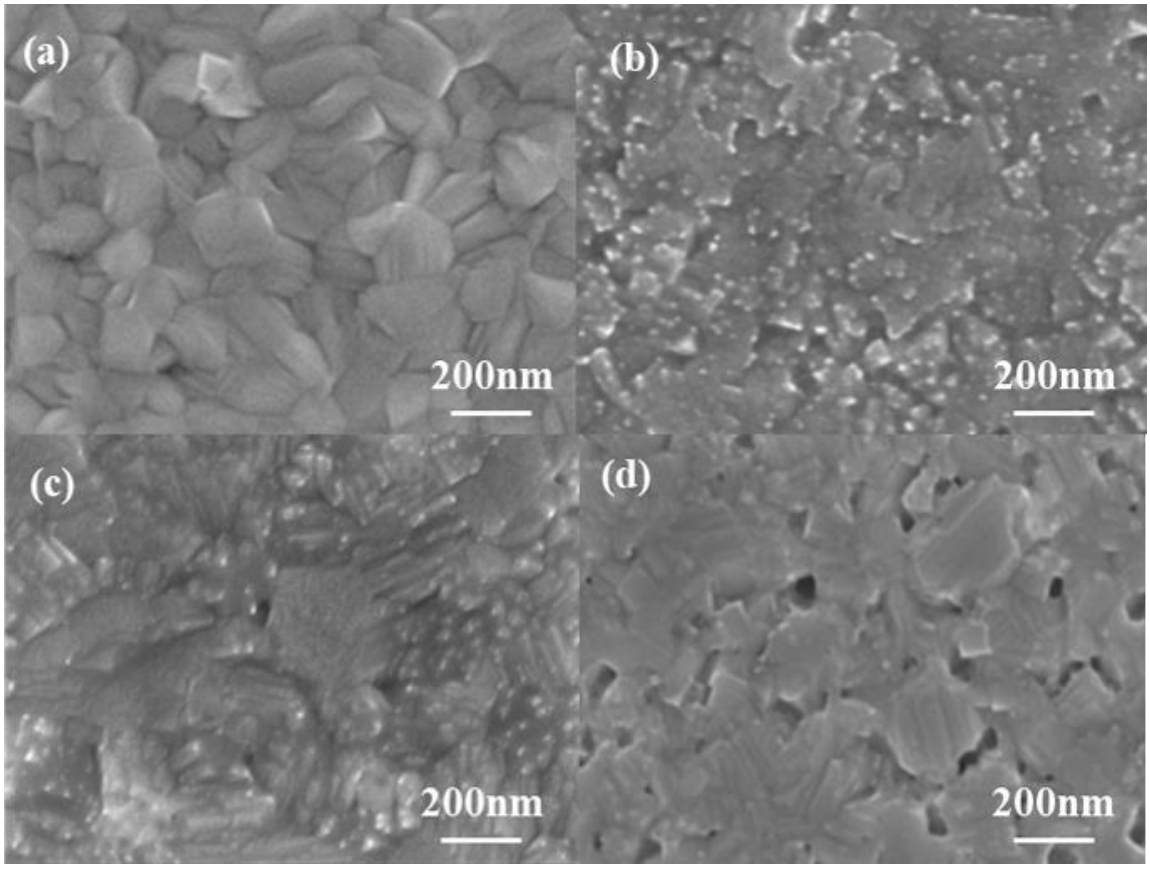

Figure 6.4. SEM images of $CsPb_{1-x}Ge_xI_2Br$ perovskite film (x, 0, 0.1, 0.2, 0.3) on FTO/SnO_2 substrates. a) $CsPbI_2Br$ perovskite, (b) $CsPb_{0.9}Ge_{0.1}I_2Br$ perovskite, (c) $CsPb_{0.8}Ge_{0.2}I_2Br$ perovskite, (d) $CsPb_{0.7}Ge_{0.3}I_2Br$ perovskite.

The XRD pattern change of the $CsPb_{1-x}Ge_xI_2Br$ perovskite materials kept in ambient air for different time is shown Figure 6.6. Similar to the results obtained from UV-Vis measurement, the cubic phase stability is enhanced upon addition of germanium as evidenced from the XRD spectra. The band gaps, Eg for the perovskite materials are calculated form the Tauc plot shown in Figure 6.7, where the E_g was 1.901, 1.894, 1.889, and 1.881 eV for x = 0, 0.1, 0.2 and 0.3, respectively. Valence band of the perovskite materials was determined from photoelectron yield spectroscopy (PYS), shown in Figure 6.1e. Valence band edge

slightly shifted from -5.82 of x= 0 to negative values of -5.75, -5.72 and -5.70 eV for x= 0.1, 0.2 and 0.3, respectively. The energy band diagram was constructed using Eg and valence band values shown in Figure 6.1f. Upon increasing the Ge content, both the balance band and conduction band of $CsPbI_2Br$ were upshifted which is similar to our previous reports. [116]

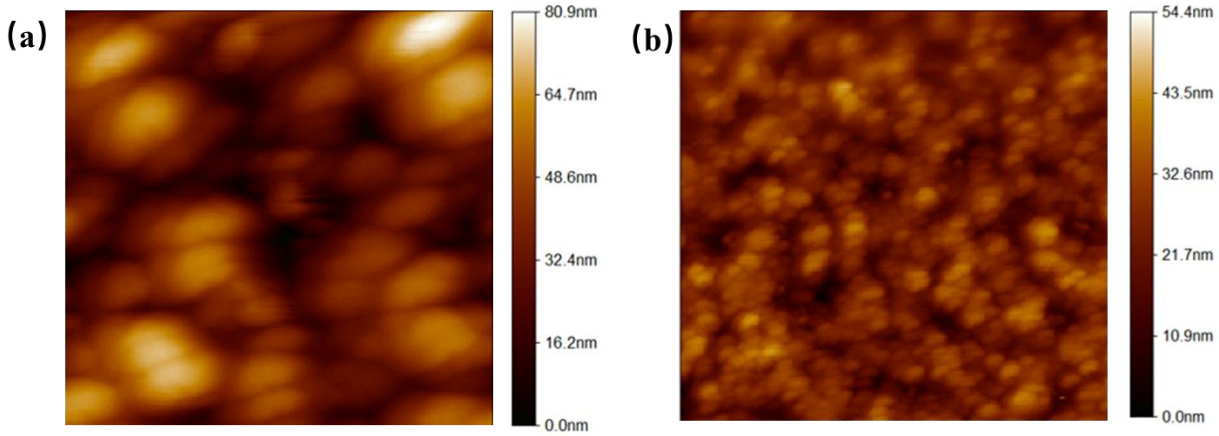

Figure 6.5. AFM images of $CsPbI_2Br$ (a) and $CsPb_{0.8}Ge_{0.2}I_2Br$ perovskite film.

Figure 6.8 shows the wide scan spectra of X-ray photoelectron spectra (XPS) for the perovskite films. The binding energy peak at 32.7 eV corresponding to the Ge 3d core levels significantly increased with the increasing content of Ge content, indicating that the Ge has been successfully incorporated into the perovskite film (Figure 6.9a). Figure 6.9b, c, d and e, show the Cs 3d, Pb 4f, I 3d and Br 3d core levels. Notably, in the Ge-incorporated $CsPbI_2Br$ films, the peaks of Cs 3d and Pb 4f are slightly shifted to higher binding energy, which is consistent with the previous reports on metal-substituted $CsPbI_2Br$ perovskite.[139-140] It has been reported that the binding energy of Pb cation and halides are not changed by a little fluctuating on ratio of I/Br in mixed-halide perovskites, nor simple physical mixing.[145-146] Therefore, the origin of the shifts comes from the changes in the chemical bonding between Cs and Pb cation, which are associated with the influence of Ge. In addition, the Br 3d peaks of $CsPbI_2Br$ decreased slightly when Ge is added. The Ge/Pb and (Pb+Ge)/Cs ratios are

calculated from the XPS spectra as shown in Figure 6.9f. The ratio of (Pb+Ge)/Cs is calculated to be close to 1.0, suggesting that Ge is substituting the Pb atoms.

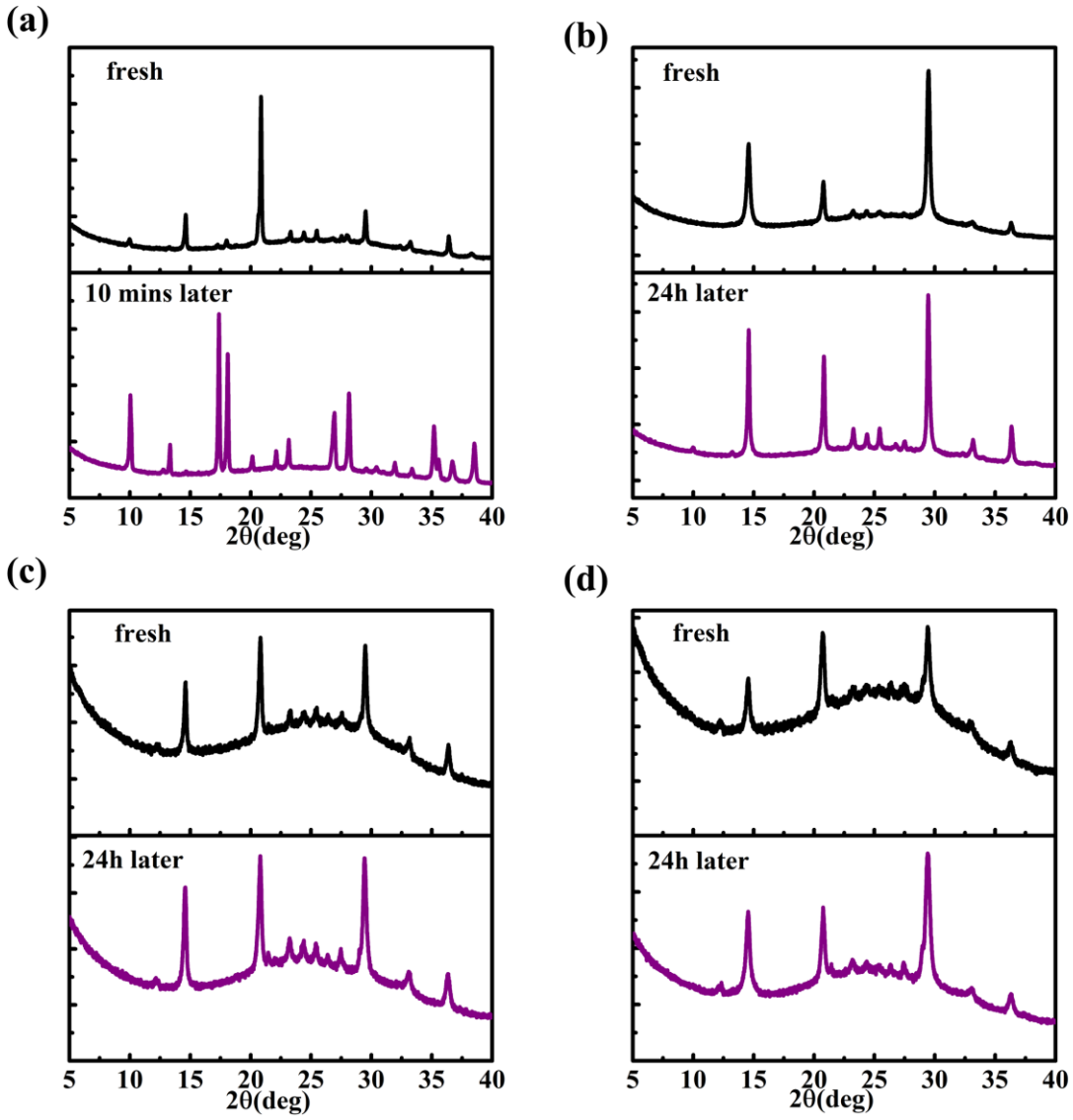

Figure 6.6. XRD spectra of the $CsPb_{1-x}Ge_xI_2Br$ perovskite film (x, 0, 0.1, 0.2, 0.3) measure at different time. (a) $CsPbI_2Br$ perovskite, (b) $CsPb_{0.9}Ge_{0.1}I_2Br$ perovskite, (c) $CsPb_{0.8}Ge_{0.2}I_2Br$ perovskite, (b) $CsPb_{0.7}Ge_{0.3}I_2Br$ perovskite.

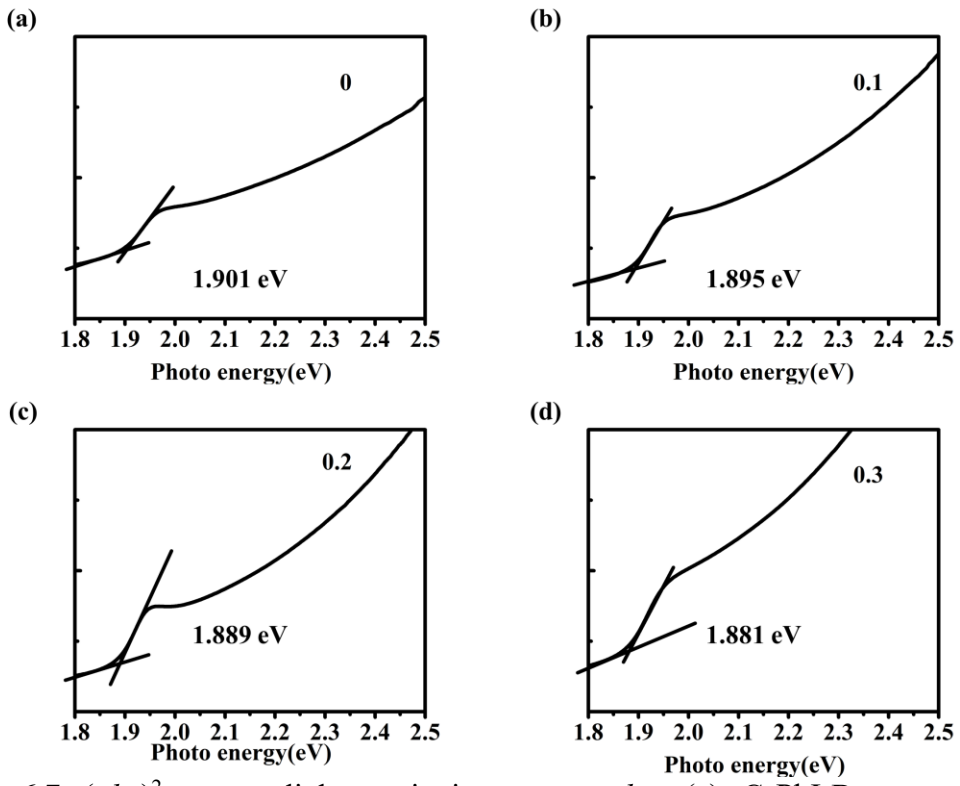

Figure 6.7 $(\alpha h\nu)^2$ versus light excitation energy $h\nu$. (a) $CsPbI_2Br$ perovskite, (b) $CsPb_{0.9}Ge_{0.1}I_2Br$ perovskite, (c) $CsPb_{0.8}Ge_{0.2}I_2Br$ perovskite, (b) $CsPb_{0.7}Ge_{0.3}I_2Br$ perovskite.

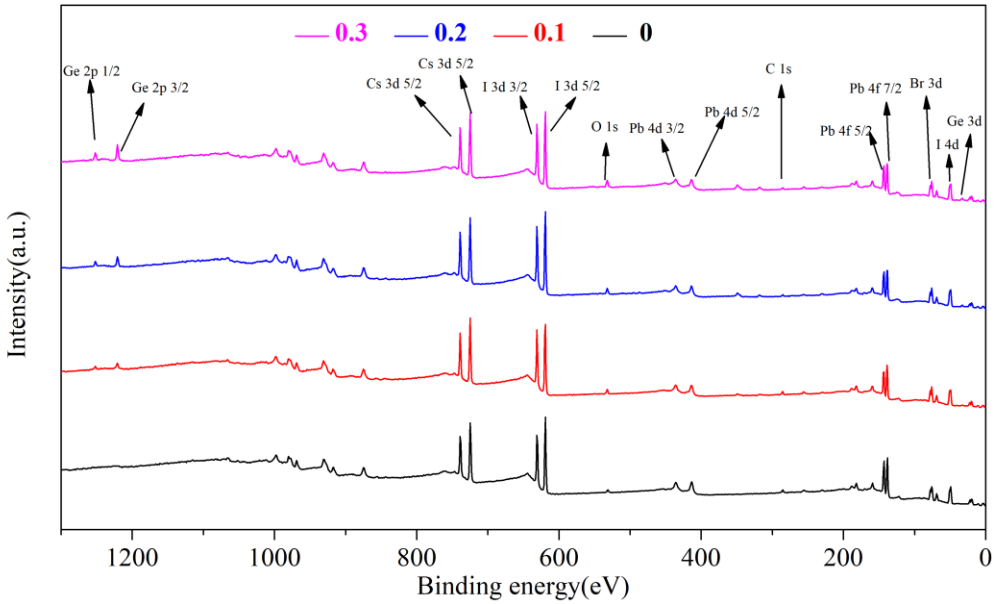

Figure 6.8. Wide scan XPS spectra $CsPb_{1-x}Ge_xI_2Br$ perovskite film (x, 0, 0.1, 0.2, 0.3)

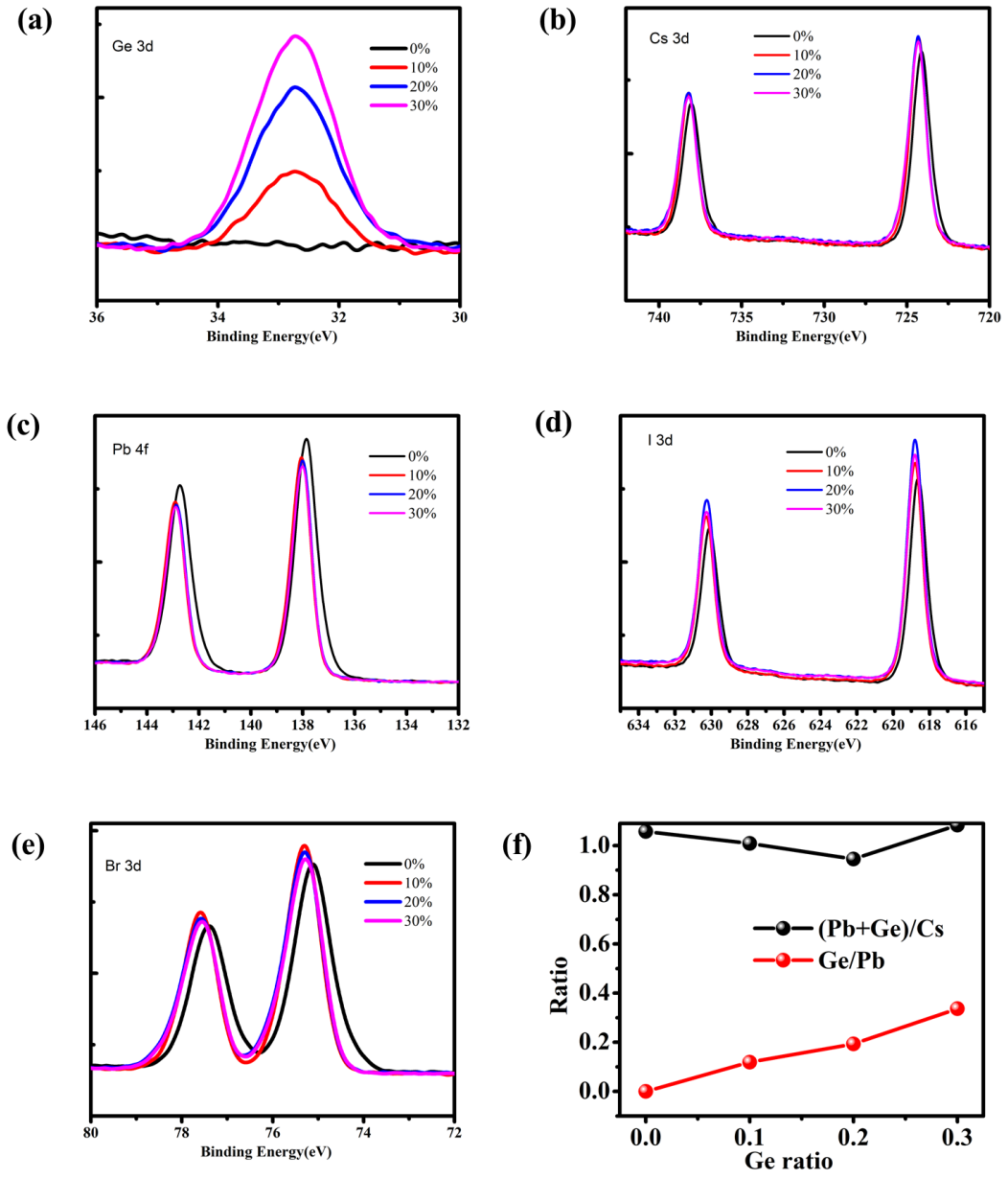

Figure 6.9. XPS core level spectra for $CsPb_{1-x}Ge_xI_2Br$ (X, 0, 0.1, 0.2, 0.3). (a) Ge 3d, (b) Cs 3d, (c) Pb 4f, (d) I 3d, (e) Br 3d. (f) The ratio of GeI_2 added initially (Horizontal line) vs. Molar ratio of Ge/Pb and (Pb+Ge)/ Cs in the film from the XPS spectra (Vertical line).

Figure 6.10a, b show the steady state photoluminescence (PL) and time-resolved PL (TRPL) of the $CsPb_{1-x}Ge_xI_2Br$ perovskite film on glass substrates. As shown in Figure 6.10a, the PL peaks centers of $CsPb_{1-x}Ge_xI_2Br$ perovskite showed a redshift with the increasing Ge

content. The TRPL curves were fitted by the double exponential decay function. The presence of fast decay component τ_1 was attributed to indicate the bimolecular recombination, and the slow decay component τ_2 was assigned to effective recombination lifetime. The detail parameters of PL lifetime are summarized in table 6.1. The calculated τ_2 of the $CsPbI_2Br$, $CsPb_{0.9}Ge_{0.1}I_2Br$, $CsPb_{0.8}Ge_{0.2}I_2Br$, and $CsPb_{0.7}Ge_{0.3}I_2Br$ films was 2.40, 3.02, 20.62 and 8.56 ns, respectively. The increased τ_2 suggesting a better effective recombination lifetime, when incorporating Ge in the $CsPbI_2Br$ perovskite, especially for the $CsPb_{0.8}Ge_{0.2}I_2Br$ perovskite.

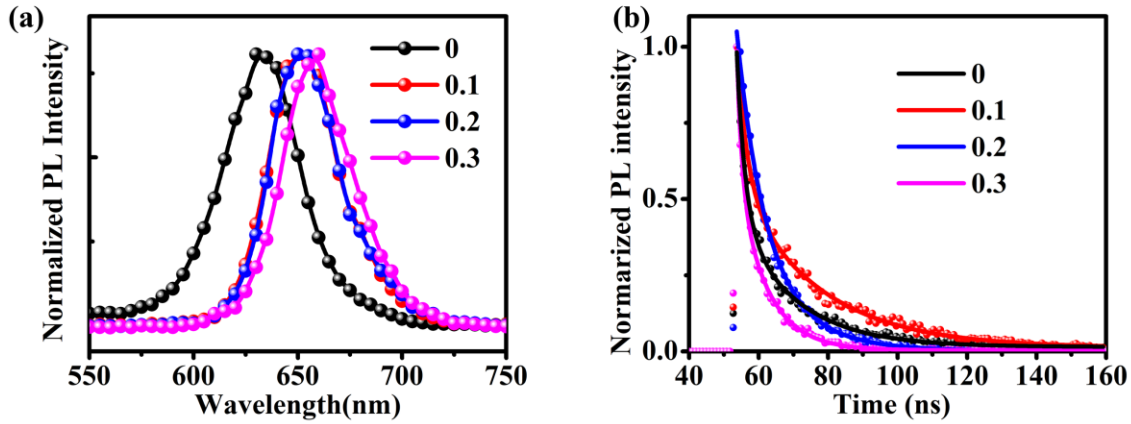

Figure 6.10 (a) Steady state PL spectra and (b) time-resolved PL spectra of annealed $CsPb_{1-x}Ge_xI_2Br$ perovskite film (x, 0, 0.1, 0.2, 0.3) Solid lines in (b) are the fitting curves using the double exponential decay model.

x ratio	τ_1	A1	τ_2	A2
0	16.66	0.440	2.40	0.649
0.1	23.47	0.487	3.02	0.545
0.2	8.38	0.814	20.62	0.143
0.3	1.47	0.472	8.56	0.577

Table 6.1. Summary of the parameters fitted from the time-resolved PL spectra. The fitting function of the double-exponential equation was $y = y_0 + A_1 e^{-\frac{x}{\tau 1}} + A_2 e^{-\frac{x}{\tau 2}}$.

The effect of Ge substitution on the PSCs performance is investigated with the planar PSC structure of FTO/SnO_2/Perovskite/P3HT/Spiro/Au. All the process of PSCs are performed in ambient air condition at high humidity. Figure 6.11a, b show the schematic structure and cross-sectional SEM image of the device. The photovoltaic parameters are listed in Table 6.2 and the current density-voltage (J-V) curves of the PSCs are shown Figure 6.11c. The solar cell based on $CsPbI_2Br$ showed the lowest power conversion efficiency (PCE) with 5.3% with a low open-circuit potential (V_{OC}) of 1.02 V. Upon Ge incorporation, the V_{OC} was increased gradually to 1.11V for $CsPb_{0.9}Ge_{0.1}I_2Br$, 1.27 V for $CsPb_{0.8}Ge_{0.2}I_2Br$ and 1.32 V for $CsPb_{0.7}Ge_{0.3}I_2Br$. The champion V_{OC} for $CsPb_{0.7}Ge_{0.3}I_2Br$ was up to 1.34 V which is the highest ever reported for the $CsPbI_2Br$ based perovskite devices. Moreover, the J_{SC} was increased from 9.06 mA/cm^2 to 11.39 mA/cm^2 for $CsPb_{0.9}Ge_{0.1}I_2Br$ and 12.15 mA/cm^2 for $CsPb_{0.8}Ge_{0.2}I_2Br$. However, the J_{SC} decreased to 10.58 mA/cm^2 for $CsPb_{0.7}Ge_{0.3}I_2Br$, which is consistent with the absorbance spectra. In addition, the fill factor (FF) also showed a greatly improved when Ge was incorporated as evidenced from Table 6.2. The highest efficiency was achieved by $CsPb_{0.8}Ge_{0.2}I_2Br$ with the PCE of 10.8%, which could be a world record for this type of perovskite prepared in ambient atmosphere at high humidity. In addition, Ge incorporated perovskite with a broad band gap of ~1.9 V and a comparable V_{OC} around 1.3 V could be a good candidate applying in perovskite/silicon and perovskite/perovskite tandem solar cells.[147-151] Next, The electrochemical impedance spectroscopy measurements were performed to study the charge-transfer mechanism at the interfaces of the PSC devices. The Nyquist plots of $CsPbI_2Br$, $CsPb_{0.8}Ge_{0.2}I_2Br$ perovskite based solar cell devices are shown in Figure 6.12. As it is known that lower Rs suggests a better electro transport and larger R_{rec} implies the lower recombination rate. According to

Figure 6.12, the solar cell device based on $CsPb_{0.8}Ge_{0.2}I_2Br$ has a much higher R_{rec} than that of $CsPbI_2Br$ which determined from the width of the semicircle, suggesting the recombination rate is decreased by Ge incorporation.[152] Therefore, it can be concluded that the larger Rrec of Ge incorporated perovskite device indicates that the carrier mobility in correspondent device is improved thus leading to enhanced V_{oc} and FF.

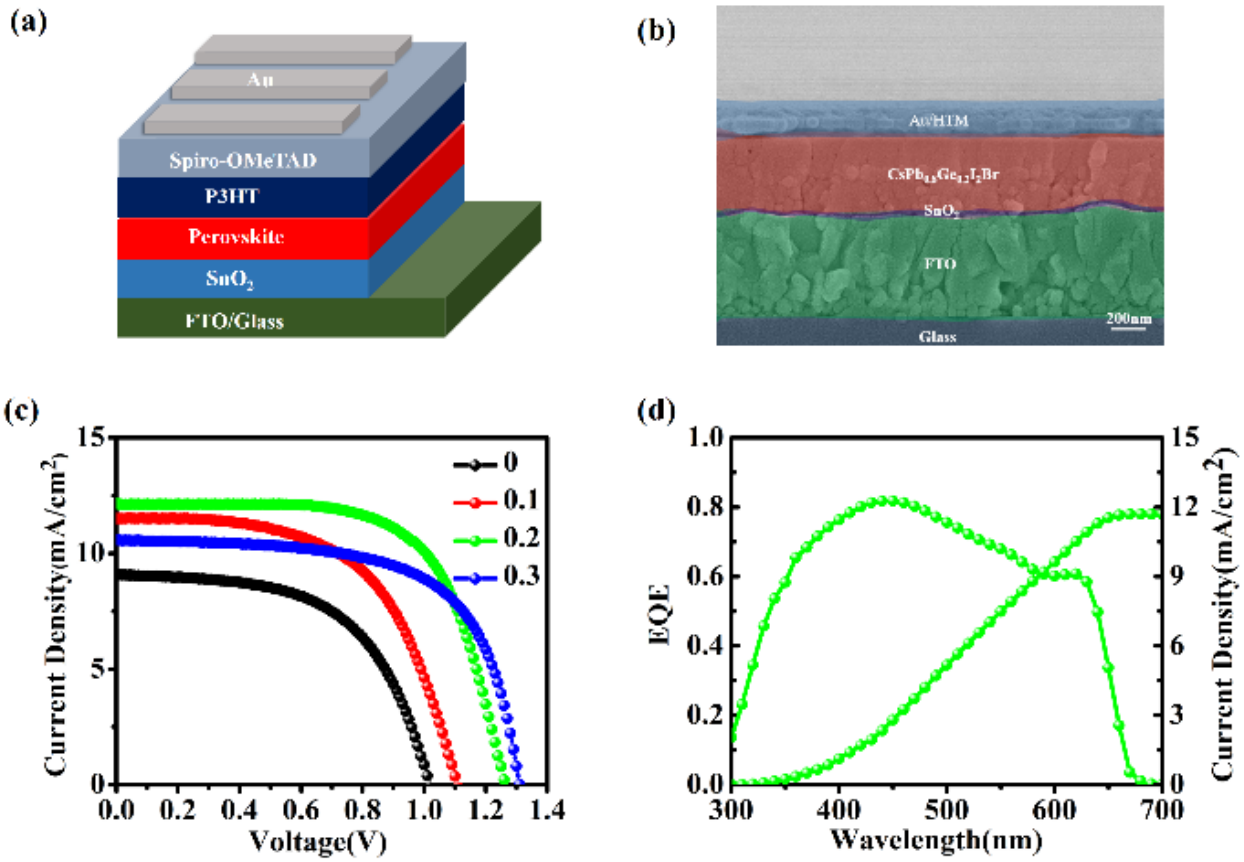

Figure 6.11. (a) Schematic structure and (b) cross sectional SEM image of planar perovskite device. (c) J-V curve in reverse scan for champion $CsPb_{1-x}Ge_xI_2Br$ perovskite solar cell. (d) IPCE spectra and the corresponding integrated current density of $CsPb_{0.8}Ge_{0.2}I_2Br$ PSC.

Table 6.2. Photovoltaic parameters of champion planar PSCs devices.

Materials	V_{OC}(V)	J_{sc}(mA/cm^2)	FF(%)	PCE(%)
$CsPbI_2Br$	1.02	9.06	57.2	5.3
$CsPb_{0.9}Ge_{0.1}I_2Br$	1.11	11.39	59.3	7.6
$CsPb_{0.8}Ge_{0.2}I_2Br$	1.27	12.15	70.1	10.8
$CsPb_{0.7}Ge_{0.3}I_2Br$	1.32	10.58	64.5	9.0

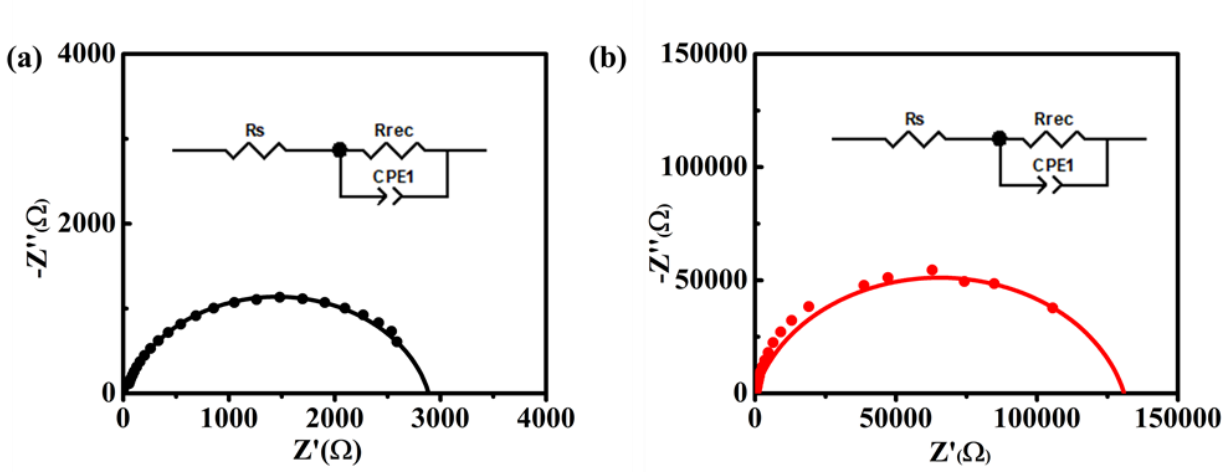

Figure 6.12. The Nyquist plots based planar perovskite devices measured in the dark under 0.7 V applied bias and the equivalent circuit diagram; the fitted curves and the experimental data are shown as solid lines corresponding points, respectively. (a) $CsPbI_2Br$, (b) $CsPb_{0.8}Ge_{0.2}I_2Br$.

Stability of $CsPbI_2Br$ and $CsPb_{0.8}Ge_{0.2}I_2Br$ PSCs is investigated and the result is shown in Figure 6.13. As shown in Figure 6.13d, the PCE of $CsPbI_2Br$ deceased rapidly to nearly 0 within 2 hours along with the rapid decreasing of V_{OC}, J_{SC} and FF. However, the PCE of $CsPb_{0.8}Ge_{0.2}I_2Br$ kept no decline over 7 hours. In addition, all the parameters including V_{OC}, J_{SC} and FF kept nearly no dropping over 7 hours measurement. The above results shows that incorporation of Ge into the $CsPbI_2Br$

perovskite enhanced the photovoltaic performances and gave stability against the phase transition for all-inorganic perovskite.

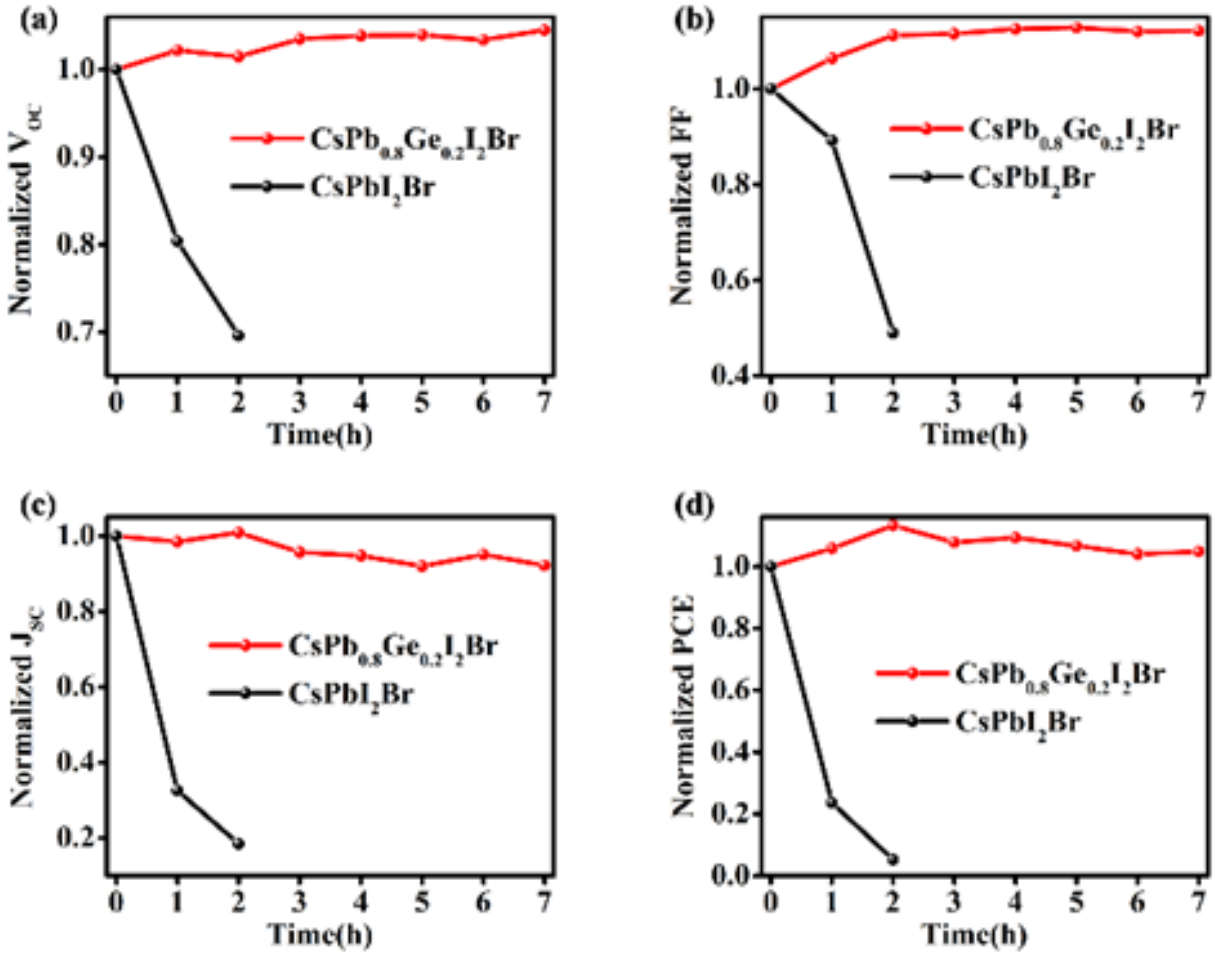

Figure 6.13. Stability test of $CsPbI_2Br$ and $CsPb_{0.8}Ge_{0.2}I_2Br$ PSCs without sealing in 50-60% RH ambient atmosphere. (a) Voc. (b) FF. (c) $J_{SC.}$ (d) PCE.

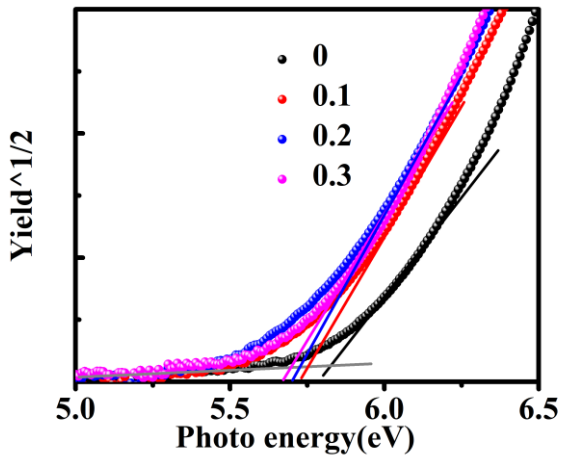

Figure 6.14 Valence band calculation for $CsPb_{1-x}Ge_xI_2Br$ perovskite film (x, 0, 0.1, 0.2, 0.3) measured by PYS.

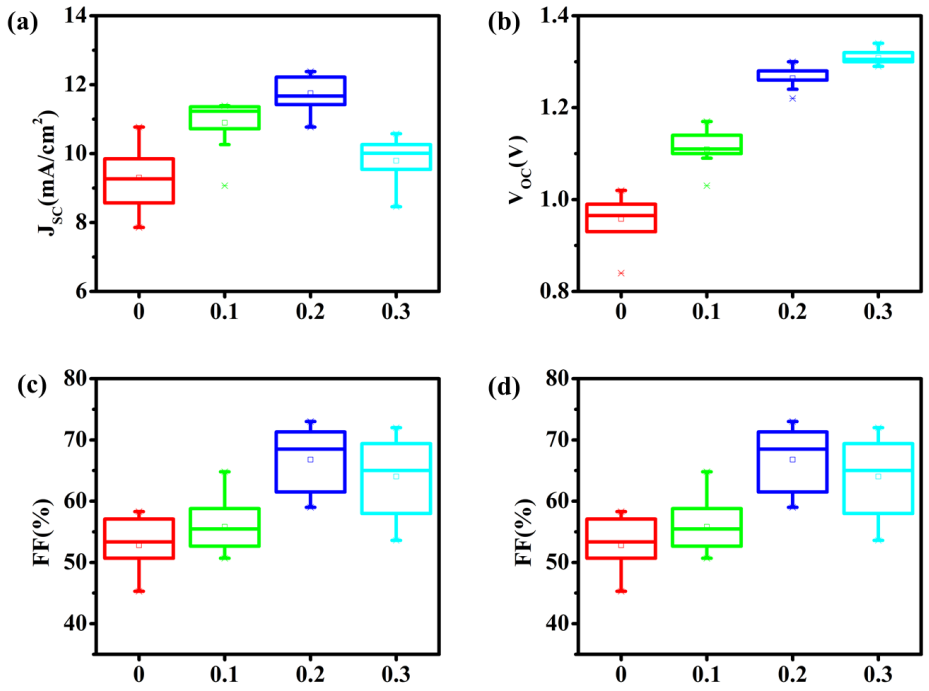

Figure 6.15 Photovoltaic statistics for the planar PSCs processed by $CsPb_{1-x}Ge_xI_2Br$ (x, 0, 0.1, 0.2, 0.3). (a) Short-circuit current, (b) Open circuit voltage, (c) FF, and (d) Efficiency. The boxes represent 80 data from the Voc-to-Jsc scan direction.

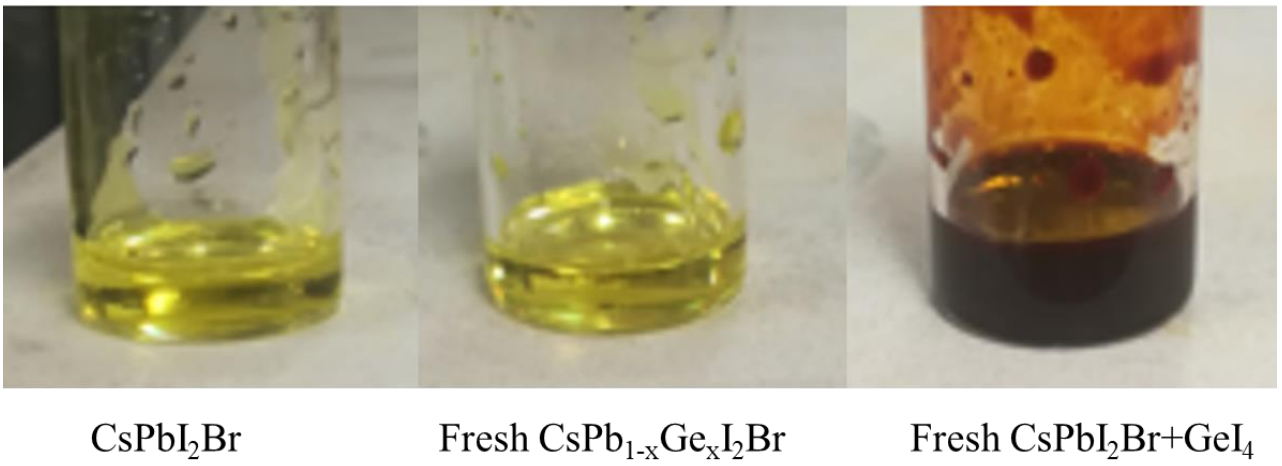

Figure 6.16. Optical images of perovskite precusor solution.

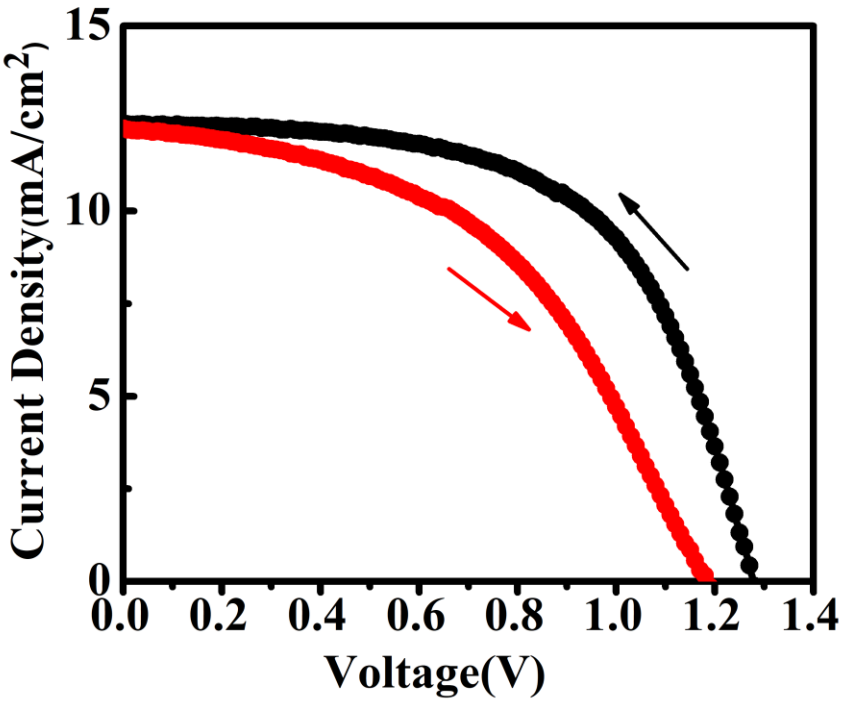

Figure 6.17. J-V curve of $CsPb_{0.8}Ge_{0.2}I_2Br$ perovskite film with reverse scan and forward scan direction.

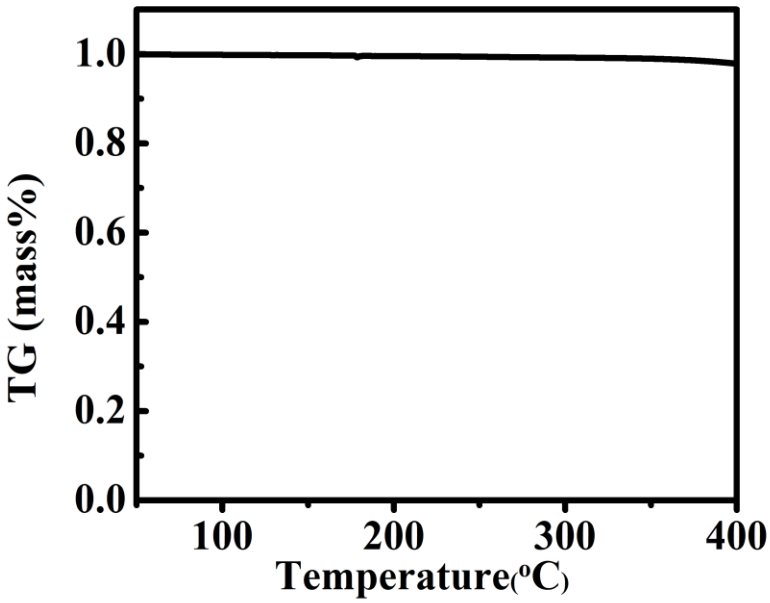

Figure 6.18. Thermogravimetric analysis (TGA) curve of $CsPb_{0.8}Ge_{0.2}I_2Br$ perovskite.

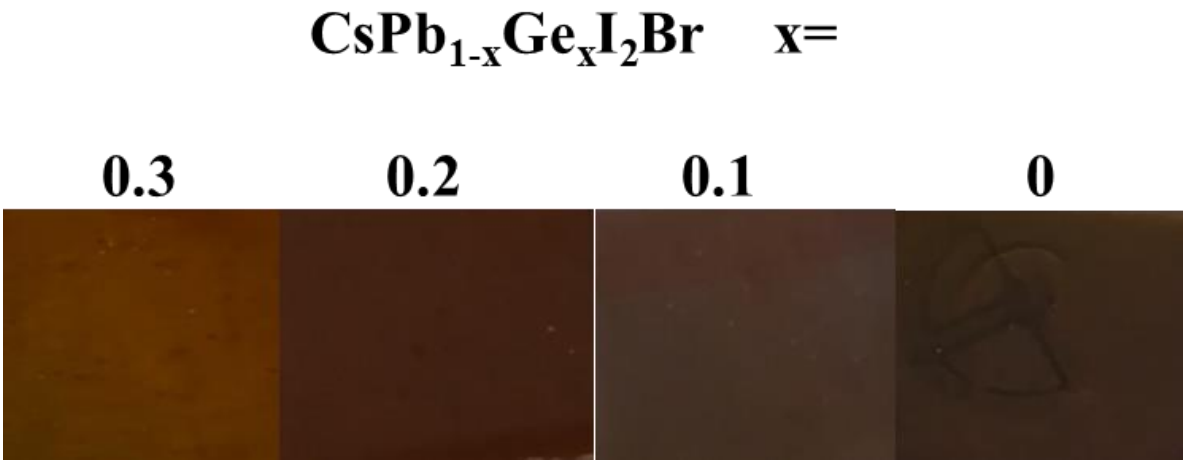

Figure 6.19. Optical images of $CsPb_{1-x}Ge_xI_2Br$ perovskite films.

6.4 Conclusion

In conclusion, novel all-inorganic $CsPb_{1-x}Ge_xI_2Br$ (x, 0, 0.1, 0.2, 0.3) perovskites is successfully prepared in ambient temperature at high humidity. The cubic phase stability of the all-inorganic perovskite with germanium was effectively enhanced. The all-inorganic perovskite with Ge shows a better effective recombination lifetime and low trap densities. Moreover, incorporation of Ge increased the V_{OC}, leading to the highest V_{OC} of up to 1.34 V for $CsPb_{0.7}Ge_{0.3}I_2Br$ perovskite solar cells. The highest power conversion efficiency of 10.8 % with high open-circuit voltage (V_{OC}) of 1.27 V in planar solar cell based on $CsPb_{0.8}Ge_{0.2}I_2Br$ perovskite was achieved. At last, all the parameters including short circuit current, V_{OC}, fill factor and efficiency of $CsPb_{0.8}Ge_{0.2}I_2Br$ perovskite solar cells was kept after the samples were measured for more than 7 hour in 50-60% relative humidity humid air without encapsulation. This research gives a good direction for preparing stable all-inorganic perovskite devices in ambient condition and has the prospect to be used in tandem solar cells due to the high V_{OC}.

General Conclusions

High efficiency perovskite solar cells (PSCs) need to be fabricated in the nitrogen-filled glove box by atmosphere-controlled crystallization process to avoid the moisture, as organometallic halide perovskite is easily dissolved in water. However, the use of glove box process is of great concern for mass level production of PSCs. Despite the high efficiency of perovskite solar cells, the long term stability and degradation in humid atmosphere are issues that still needed to be addressed.

In chapter 2, notable efficient $CH_3NH_3PbI_3$ solar cells can be obtained in high humidity ambient atmosphere (60%-70% relative humidity) by using acetate as anti-solvent, in which dependence of methyl, ethyl, propyl, and butyl acetate on the crystal growth mechanism are discussed. It is explored that acetate screens the sensitive perovskite intermediate phases from water molecules during perovskite film formation and annealing. It is revealed that relatively high vapor pressure and high water solubility of methyl acetate (MA) leads to the formation of highly dense and pinhole free perovskite films guiding to the best power conversion efficiency of 16.3% with a reduced hysteresis. The devices prepared using MA showed remarkable shelf life stability of more than 80% for 360 hours in ambient air condition, when compared to the devices fabricated using other anti-solvents with low vapor pressure and low water solubility. Moreover, the PCE still kept at 15.6% even though 2 v% deionized water was added in the MA for preparing the perovskite layer.

In chapter 3, we propose one-step fabrication of high-quality $MAPbI_3$ perovskite films in around 50 % RH humid ambient air by using diethyl ether as an anti-solvent and methanol

as an additive into this anti-solvent. Because of the existence of methanol, the water molecules can be efficiently removed from the gaps of perovskite precursors and the perovskite film formation can be slightly controlled leading to pinhole-free and low roughness film. Concurrently, methanol can modify a proper DMSO ratio in the intermediate perovskite phase to regulate perovskite formation. Planar solar cells fabricated by using this method exhibited the best efficiency of 16.4 % with a reduced current density-voltage hysteresis. This efficiency value is approximately 160 % higher than the devices fabrication by using only diethyl ether treatment. From the impedance measurement, it is also found that the recombination reaction has been suppressed when the device prepared with additive anti-solvent way. This method presents a new path for controlling the growth and morphology of perovskite films in the humid climates and uncontrolled laboratories.

In chapter 4, magnesium iodide (MgI_2) was first successfully used as a dopant into $MAPbI_3$ perovskite prepared in humid air atmosphere. Mg doping decreased the valence band level which was determined from photoelectron yield spectroscopy. Compared to the pristine $MAPbI_3$ perovskite film, the 1.0 % Mg doped perovskite film showed increased crystal grain size and formation of pinhole-free perovskite film. Performance of the solar cell was increased from 14.2 % of the doping-free solar cell to 17.8 % of 1.0 % Mg doped device. Moreover, 90 % of the original PCE was still retained after storage in 30~40% relative humidity for 600 h.

In chapter 5, a novel functional organic compound 1-(ammonium acetyl)pyrene (PEYI) has successfully introduced for preparing the 2D/3D Hetero structured $MAPbI_3$ perovskite. Because of the functional organic pyrene group with high humidity resistance and strong

absorption in the ultraviolet region, the 2D/3D perovskite film showed notable stability with no degradation in ~60% relative humidity after even 6 months and exhibited a high ultraviolet irradiation stability which kept nearly no degradation after one hour in the UV Ozone treatment. Planar PSCs were fabricated in the ~60% relative humidity air outside glovebox. The champion efficiency of $(PEY_2PbI_4)_{0.02}MAPbI_3$ perovskite solar cells was 14.7 % with nearly no hysteresis which is equal performance of 3D $MAPbI_3$ devices (15.0%). This work presents a new direction for enhancing the solar cells` performance and stability by incorporating a functional organic aromatic compound into the perovskite layer.

In chapter 6, novel inorganic $CsPb_{1-x}Ge_xI_2Br$ perovskites were prepared in humid ambient atmosphere without glovebox. The phase stability of the inorganic perovskite was effectively enhanced after germanium addition. In addition, highest power conversion efficiency of 10.8% with high open-circuit voltage (V_{OC}) of 1.27 V in planar solar cell based on $CsPb_{0.8}Ge_{0.2}I_2Br$ perovskite was achieved. Furthermore, highest V_{OC} up to 1.34 V was obtained by $CsPb_{0.7}Ge_{0.3}I_2Br$ perovskite which is a remarkable record in the field of inorganic perovskite solar cells. More importantly, all the photovoltaic parameters of $CsPb_{0.8}Ge_{0.2}I_2Br$ perovskite solar cells shows nearly no decay after 7 hours measurement in 50-60% relative humidity humid air without encapsulation.

References

(1) Liu, M.; Johnston, M. B.; Snaith, H. J. Efficient planar heterojunction perovskite solar cells by vapour deposition. *Nature* **2013,** *501* (7467), 395.

(2) Zhou, H.; Chen, Q.; Li, G.; Luo, S.; Song, T.-b.; Duan, H.-S.; Hong, Z.; You, J.; Liu, Y.; Yang, Y. Interface engineering of highly efficient perovskite solar cells. *Science* **2014,** *345* (6196), 542-546.

(3) Lee, M. M.; Teuscher, J.; Miyasaka, T.; Murakami, T. N.; Snaith, H. J. Efficient hybrid solar cells based on meso-superstructured organometal halide perovskites. *Science* **2012,** *338* (6107), 643-647.

(4) Kim, H.-S.; Lee, C.-R.; Im, J.-H.; Lee, K.-B.; Moehl, T.; Marchioro, A.; Moon, S.-J.; Humphry-Baker, R.; Yum, J.-H.; Moser, J. E.; Grätzel, M.; Park, N.-G. Lead Iodide Perovskite Sensitized All-Solid-State Submicron Thin Film Mesoscopic Solar Cell with Efficiency Exceeding 9%. *Scientific Reports* **2012,** *2*, 591, DOI: 10.1038/srep00591 https://www.nature.com/articles/srep00591#supplementary-information.

(5) Stranks, S. D.; Eperon, G. E.; Grancini, G.; Menelaou, C.; Alcocer, M. J.; Leijtens, T.; Herz, L. M.; Petrozza, A.; Snaith, H. J. Electron-hole diffusion lengths exceeding 1 micrometer in an organometal trihalide perovskite absorber. *Science* **2013,** *342* (6156), 341-344.

(6) Lee, M. M.; Teuscher, J.; Miyasaka, T.; Murakami, T. N.; Snaith, H. J. Efficient hybrid solar cells based on meso-superstructured organometal halide perovskites. *Science* **2012**, 1228604.

(7) Etgar, L.; Gao, P.; Xue, Z.; Peng, Q.; Chandiran, A. K.; Liu, B.; Nazeeruddin, M. K.; Grätzel, M. Mesoscopic CH3NH3PbI3/TiO2 heterojunction solar cells. *Journal of the American Chemical Society* **2012,** *134* (42), 17396-17399.

(8) Burschka, J.; Pellet, N.; Moon, S.-J.; Humphry-Baker, R.; Gao, P.; Nazeeruddin, M. K.; Grätzel, M. Sequential deposition as a route to high-performance perovskite-sensitized solar cells. *Nature* **2013,** *499* (7458), 316.

(9) Li, G.; Shrotriya, V.; Huang, J.; Yao, Y.; Moriarty, T.; Emery, K.; Yang, Y. High-efficiency solution processable polymer photovoltaic cells by self-organization of polymer blends. In *Materials For Sustainable Energy: A Collection of Peer-Reviewed Research and Review Articles from Nature Publishing Group*; World Scientific: 2011; pp 80-84.

(10) Yang, W. S.; Park, B.-W.; Jung, E. H.; Jeon, N. J.; Kim, Y. C.; Lee, D. U.; Shin, S. S.; Seo, J.; Kim, E. K.; Noh, J. H. Iodide management in formamidinium-lead-halide–based perovskite layers for efficient solar cells. *Science* **2017,** *356* (6345), 1376-1379.

(11) Leijtens, T.; Eperon, G. E.; Pathak, S.; Abate, A.; Lee, M. M.; Snaith, H. J. Overcoming ultraviolet light instability of sensitized TiO 2 with meso-superstructured organometal tri-halide perovskite solar cells. *Nature communications* **2013,** *4*, 2885.

(12) Liu, M.; Johnston, M. B.; Snaith, H. J. Efficient planar heterojunction perovskite solar cells by vapour deposition. *Nature* **2013,** *501* (7467), 395-398.

(13) Domanski, K.; Alharbi, E. A.; Hagfeldt, A.; Grätzel, M.; Tress, W. Systematic investigation of the impact of operation conditions on the degradation behaviour of perovskite solar cells. *Nature Energy* **2018**, 1.

(14) Kojima, A.; Teshima, K.; Shirai, Y.; Miyasaka, T. Organometal halide perovskites as visible-light sensitizers for photovoltaic cells. *Journal of the American Chemical Society* **2009,** *131* (17), 6050-6051.

(15) Xiao, M.; Huang, F.; Huang, W.; Dkhissi, Y.; Zhu, Y.; Etheridge, J.; Gray-Weale, A.; Bach, U.; Cheng, Y. B.; Spiccia, L. A fast deposition-crystallization procedure for highly efficient lead iodide perovskite thin-film solar cells. *Angewandte Chemie* **2014,** *126* (37), 10056-10061.

(16) Park, N.-G.; Grätzel, M.; Miyasaka, T.; Zhu, K.; Emery, K. Towards stable and commercially available perovskite solar cells. *Nature Energy* **2016,** *1*, 16152.

(17) Konstantakou, M.; Perganti, D.; Falaras, P.; Stergiopoulos, T. Anti-solvent crystallization strategies for highly efficient perovskite solar cells. *Crystals* **2017,** *7* (10), 291.

(18) Malinkiewicz, O.; Yella, A.; Lee, Y. H.; Espallargas, G. M.; Graetzel, M.; Nazeeruddin, M. K.; Bolink, H. J. Perovskite solar cells employing organic charge-transport layers. *Nature Photonics* **2014,** *8* (2), 128-132.

(19) Green, M. A.; Ho-Baillie, A.; Snaith, H. J. The emergence of perovskite solar cells. *Nature Photonics* **2014,** *8* (7), 506-514.

(20) Eperon, G. E.; Burlakov, V. M.; Docampo, P.; Goriely, A.; Snaith, H. J. Morphological control for high performance, solution-processed planar heterojunction perovskite solar cells. *Advanced Functional Materials* **2014,** *24* (1), 151-157.

(21) Chen, Q.; Zhou, H.; Hong, Z.; Luo, S.; Duan, H.-S.; Wang, H.-H.; Liu, Y.; Li, G.; Yang, Y. Planar heterojunction perovskite solar cells via vapor-assisted solution process. *Journal of the American Chemical Society* **2013,** *136* (2), 622-625.

(22) Ahn, N.; Son, D.-Y.; Jang, I.-H.; Kang, S. M.; Choi, M.; Park, N.-G. Highly reproducible perovskite solar cells with average efficiency of 18.3% and best efficiency of 19.7% fabricated via Lewis base adduct of lead (II) iodide. *Journal of the American Chemical Society* **2015,** *137* (27), 8696-8699.

(23) Noh, J. H.; Im, S. H.; Heo, J. H.; Mandal, T. N.; Seok, S. I. Chemical management for colorful, efficient, and stable inorganic–organic hybrid nanostructured solar cells. *Nano letters* **2013,** *13* (4), 1764-1769.

(24) Song, Z.; Abate, A.; Watthage, S. C.; Liyanage, G. K.; Phillips, A. B.; Steiner, U.; Graetzel, M.; Heben, M. J. Perovskite Solar Cell Stability in Humid Air: Partially Reversible Phase Transitions in the PbI2-CH3NH3I-H2O System. *Advanced Energy Materials* **2016,** *6* (19).

(25) Yang, J.; Siempelkamp, B. D.; Liu, D.; Kelly, T. L. Investigation of CH3NH3PbI3 degradation rates and mechanisms in controlled humidity environments using in situ techniques. *ACS nano* **2015,** *9* (2), 1955-1963.

(26) Tai, Q.; You, P.; Sang, H.; Liu, Z.; Hu, C.; Chan, H. L.; Yan, F. Efficient and stable perovskite solar cells prepared in ambient air irrespective of the humidity. *Nature communications* **2016,** *7*.

(27) Li, G.; Zhang, T.; Zhao, Y. Hydrochloric acid accelerated formation of planar CH 3 NH 3 PbI 3 perovskite with high humidity tolerance. *Journal of Materials Chemistry A* **2015,** *3* (39), 19674-19678.

(28) Troughton, J.; Hooper, K.; Watson, T. M. Humidity resistant fabrication of CH3NH3PbI3 perovskite solar cells and modules. *Nano Energy* **2017,** *39*, 60-68.

(29) Ke, W.; Fang, G.; Liu, Q.; Xiong, L.; Qin, P.; Tao, H.; Wang, J.; Lei, H.; Li, B.; Wan, J. Low-temperature solution-processed tin oxide as an alternative electron transporting layer for efficient perovskite solar cells. *Journal of the American Chemical Society* **2015,** *137* (21), 6730-6733.

(30) Lin, N.; Qiao, J.; Dong, H.; Ma, F.; Wang, L. Morphology-controlled CH 3 NH 3 PbI 3 films by hexane-assisted one-step solution deposition for hybrid perovskite mesoscopic solar cells with high reproductivity. *Journal of Materials Chemistry A* **2015,** *3* (45), 22839-22845.

(31) Atkins, P.; De Paula, J.; Keeler, J. *Atkins' physical chemistry*, Oxford university press: 2018.

(32) Jeon, N. J.; Noh, J. H.; Kim, Y. C.; Yang, W. S.; Ryu, S.; Seok, S. I. Solvent engineering for high-performance inorganic–organic hybrid perovskite solar cells. *Nature materials* **2014,** *13* (9), 897-903.

(33) Yin, M.; Xie, F.; Chen, H.; Yang, X.; Ye, F.; Bi, E.; Wu, Y.; Cai, M.; Han, L. Annealing-free perovskite films by instant crystallization for efficient solar cells. *Journal of Materials Chemistry A* **2016,** *4* (22), 8548-8553.

(34) Bai, Y.; Xiao, S.; Hu, C.; Zhang, T.; Meng, X.; Li, Q.; Yang, Y.; Wong, K. S.; Chen, H.; Yang, S. A pure and stable intermediate phase is key to growing aligned and vertically monolithic perovskite crystals for efficient PIN planar perovskite solar cells with high processibility and stability. *Nano Energy* **2017,** *34*, 58-68.

(35) Burschka, J.; Pellet, N.; Moon, S.-J.; Humphry-Baker, R.; Gao, P.; Nazeeruddin, M. K.; Grätzel, M. Sequential deposition as a route to high-performance perovskite-sensitized solar cells. *Nature* **2013,** *499* (7458), 316-319.

(36) Sun, S.; Salim, T.; Mathews, N.; Duchamp, M.; Boothroyd, C.; Xing, G.; Sum, T. C.; Lam, Y. M. The origin of high efficiency in low-temperature solution-processable bilayer organometal halide hybrid solar cells. *Energy & Environmental Science* **2014,** *7* (1), 399-407.

(37) Im, J.-H.; Lee, C.-R.; Lee, J.-W.; Park, S.-W.; Park, N.-G. 6.5% efficient perovskite quantum-dot-sensitized solar cell. *Nanoscale* **2011,** *3* (10), 4088-4093.

(38) Baikie, T.; Fang, Y.; Kadro, J. M.; Schreyer, M.; Wei, F.; Mhaisalkar, S. G.; Graetzel, M.; White, T. J. Synthesis and crystal chemistry of the hybrid perovskite (CH 3 NH 3) PbI 3 for solid-state sensitised solar cell applications. *Journal of Materials Chemistry A* **2013,** *1* (18), 5628-5641.

(39) Wang, Y.; Wu, J.; Zhang, P.; Liu, D.; Zhang, T.; Ji, L.; Gu, X.; Chen, Z. D.; Li, S. Stitching triple cation perovskite by a mixed anti-solvent process for high performance perovskite solar cells. *Nano Energy* **2017,** *39*, 616-625.

(40) Salim, T.; Sun, S.; Abe, Y.; Krishna, A.; Grimsdale, A. C.; Lam, Y. M. Perovskite-based solar cells: impact of morphology and device architecture on device performance. *Journal of Materials Chemistry A* **2015,** *3* (17), 8943-8969.

(41) Xiao, Z.; Dong, Q.; Bi, C.; Shao, Y.; Yuan, Y.; Huang, J. Solvent annealing of perovskite‐induced crystal growth for photovoltaic‐device efficiency enhancement. *Advanced Materials* **2014,** *26* (37), 6503-6509.

(42) Ma, Y.; Liu, Y.; Shin, I.; Hwang, I.-W.; Jung, Y. K.; Jeong, J. H.; Park, S. H.; Kim, K. H. Understanding and tailoring grain growth of lead-halide perovskite for solar cell application. *ACS applied materials & interfaces* **2017,** *9* (39), 33925-33933.

(43) Wang, K.; Shi, Y.; Li, B.; Zhao, L.; Wang, W.; Wang, X.; Bai, X.; Wang, S.; Hao, C.; Ma, T. Amorphous Inorganic Electron-Selective Layers for Efficient Perovskite Solar Cells: Feasible Strategy Towards Room-Temperature Fabrication. *Advanced Materials* **2016,** *28* (9), 1891-1897.

(44) Liu, C.; Yang, Y.; Ding, Y.; Xu, J.; Liu, X.; Zhang, B.; Yao, J.; Hayat, T.; Alsaedi, A.; Dai, S. High-efficiency and UV-stable Planar Perovskite Solar Cells Using Low-temperature Solution-processed Li-TFSI Doping C60 as Electron Transport Layers. *ChemSusChem* **2018**.

(45) Dong, J.; Jia, J.; Fan, L.; Huang, M.; Lin, J.; He, X.; Lan, Z. Annealing-Free Cr2O3 Electron-Selective Layer for Efficient Hybrid Perovskite Solar Cells. *ChemSusChem* **2017**.

(46) Bu, T.; Wu, L.; Liu, X.; Yang, X.; Zhou, P.; Yu, X.; Qin, T.; Shi, J.; Wang, S.; Li, S. Synergic Interface Optimization with Green Solvent Engineering in Mixed Perovskite Solar Cells. *Advanced Energy Materials* **2017,** *7* (20).

(47) Kim, B. J.; Kim, D. H.; Lee, Y.-Y.; Shin, H.-W.; Han, G. S.; Hong, J. S.; Mahmood, K.; Ahn, T. K.; Joo, Y.-C.; Hong, K. S. Highly efficient and bending durable perovskite solar cells: toward a wearable power source. *Energy & Environmental Science* **2015,** *8* (3), 916-921.

(48) Habisreutinger, S. N.; Leijtens, T.; Eperon, G. E.; Stranks, S. D.; Nicholas, R. J.; Snaith, H. J. Carbon nanotube/polymer composites as a highly stable hole collection layer in perovskite solar cells. *Nano letters* **2014,** *14* (10), 5561-5568.

(49) Jeng, J. Y.; Chiang, Y. F.; Lee, M. H.; Peng, S. R.; Guo, T. F.; Chen, P.; Wen, T. C. CH3NH3PbI3 perovskite/fullerene planar-heterojunction hybrid solar cells. *Advanced Materials* **2013,** *25* (27), 3727-3732.

(50) He, T.; Liu, Z.; Zhou, Y.; Ma, H. The stable perovskite solar cell prepared by rapidly annealing perovskite film with water additive in ambient air. *Solar Energy Materials and Solar Cells* **2018,** *176*, 280-287.

(51) Tsai, H.; Nie, W.; Cheruku, P.; Mack, N. H.; Xu, P.; Gupta, G.; Mohite, A. D.; Wang, H.-L. Optimizing composition and morphology for large-grain perovskite solar cells via chemical control. *Chemistry of Materials* **2015,** *27* (16), 5570-5576.

(52) Liao, W.; Zhao, D.; Yu, Y.; Grice, C. R.; Wang, C.; Cimaroli, A. J.; Schulz, P.; Meng, W.; Zhu, K.; Xiong, R. G. Lead-Free Inverted Planar Formamidinium Tin Triiodide Perovskite Solar Cells Achieving Power Conversion Efficiencies up to 6.22%. *Advanced Materials* **2016,** *28* (42), 9333-9340.

(53) Watthage, S. C.; Song, Z.; Shrestha, N.; Phillips, A. B.; Liyanage, G. K.; Roland, P. J.; Ellingson, R. J.; Heben, M. J. Enhanced Grain Size, Photoluminescence, and Photoconversion Efficiency with Cadmium Addition during the Two-Step Growth of CH3NH3PbI3. *ACS applied materials & interfaces* **2017,** *9* (3), 2334-2341.

(54) Lee, K.-M.; Lin, C.-J.; Liou, B.-Y.; Yu, S.-M.; Hsu, C.-C.; Suryanarayanan, V.; Wu, M.-C. Selection of anti-solvent and optimization of dropping volume for the preparation of large area sub-module perovskite solar cells. *Solar Energy Materials and Solar Cells* **2017,** *172*, 368-375.

(55) Williamson, G.; Hall, W. X-ray line broadening from filed aluminium and wolfram. *Acta metallurgica* **1953,** *1* (1), 22-31.

(56) Li, B.; Fei, C.; Zheng, K.; Qu, X.; Pullerits, T.; Cao, G.; Tian, J. Constructing water-resistant CH 3 NH 3 PbI 3 perovskite films via coordination interaction. *Journal of Materials Chemistry A* **2016,** *4* (43), 17018-17024.

(57) Ren, Y.-K.; Ding, X.-H.; Wu, Y.-H.; Zhu, J.; Hayat, T.; Alsaedi, A.; Xu, Y.-F.; Li, Z.-Q.; Yang, S.-F.; Dai, S.-Y. Temperature-assisted rapid nucleation: a facile method to optimize the film morphology for perovskite solar cells. *Journal of Materials Chemistry A* **2017,** *5* (38), 20327-20333.

(58) Szostak, R.; Castro, J. A.; Marques, A. S.; Nogueira, A. F. Understanding perovskite formation through the intramolecular exchange method in ambient conditions. *Journal of Photonics for Energy* **2017,** *7* (2), 022002.

(59) Zhu, Z.; Hadjiev, V. G.; Rong, Y.; Guo, R.; Cao, B.; Tang, Z.; Qin, F.; Li, Y.; Wang, Y.; Hao, F. Interaction of organic cation with water molecule in perovskite MAPbI3: From dynamic orientational disorder to hydrogen bonding. *Chemistry of Materials* **2016,** *28* (20), 7385-7393.

(60) Guo, X.; McCleese, C.; Kolodziej, C.; Samia, A. C.; Zhao, Y.; Burda, C. Identification and characterization of the intermediate phase in hybrid organic–inorganic MAPbI 3 perovskite. *Dalton Transactions* **2016,** *45* (9), 3806-3813.

(61) Sidhik, S.; Esparza, D.; Martínez-Benítez, A.; López-Luke, T.; Carriles, R.; De la Rosa, E. Improved performance of mesoscopic perovskite solar cell using an accelerated crystalline formation method. *Journal of Power Sources* **2017,** *365*, 169-178.

(62) Rowley, H.; Reed, W. R. Solubility of Water in Diethyl Ether at 25°. *Journal of the American Chemical Society* **1951,** *73* (6), 2960-2960.

(63) Paek, S.; Schouwink, P.; Athanasopoulou, E. N.; Cho, K.; Grancini, G.; Lee, Y.; Zhang, Y.; Stellacci, F.; Nazeeruddin, M. K.; Gao, P. From Nano-to Micrometer Scale: The Role of Antisolvent Treatment on High Performance Perovskite Solar Cells. *Chemistry of Materials* **2017,** *29* (8), 3490-3498.

(64) Rong, Y.; Venkatesan, S.; Guo, R.; Wang, Y.; Bao, J.; Li, W.; Fan, Z.; Yao, Y. Critical kinetic control of non-stoichiometric intermediate phase transformation for efficient perovskite solar cells. *Nanoscale* **2016,** *8* (26), 12892-12899.

(65) Acik, M.; Alam, T. M.; Guo, F.; Ren, Y.; Lee, B.; Rosenberg, R. A.; Mitchell, J. F.; Park, I. K.; Lee, G.; Darling, S. B. Substitutional Growth of Methylammonium Lead Iodide Perovskites in Alcohols. *Advanced Energy Materials* **2018,** *8* (5).

(66) Zhou, Y.; Game, O. S.; Pang, S.; Padture, N. P. Microstructures of organometal trihalide perovskites for solar cells: their evolution from solutions and characterization. *The journal of physical chemistry letters* **2015,** *6* (23), 4827-4839.

(67) Kim, M. K.; Jeon, T.; Park, H. I.; Lee, J. M.; Nam, S. A.; Kim, S. O. Effective control of crystal grain size in CH 3 NH 3 PbI 3 perovskite solar cells with a pseudohalide Pb (SCN) 2 additive. *CrystEngComm* **2016,** *18* (32), 6090-6095.

(68) Zhou, W.; Zhou, P.; Lei, X.; Fang, Z.; Zhang, M.; Liu, Q.; Chen, T.; Zeng, H.; Ding, L.; Zhu, J. Phase Engineering of Perovskite Materials for High-efficiency Solar Cells: Rapid Conversion of CH3NH3PbI3 to Phase-pure CH3NH3PbCl3 via Hydrochloric Acid Vapor Annealing Post-treatment. *ACS applied materials & interfaces* **2018,** *10* (2), 1897-1908.

(69) Tai, Q.; You, P.; Sang, H.; Liu, Z.; Hu, C.; Chan, H. L.; Yan, F. Efficient and stable perovskite solar cells prepared in ambient air irrespective of the humidity. *Nature communications* **2016,** *7*, 11105.

(70) Han, Y.; Meyer, S.; Dkhissi, Y.; Weber, K.; Pringle, J. M.; Bach, U.; Spiccia, L.; Cheng, Y.-B. Degradation observations of encapsulated planar CH 3 NH 3 PbI 3 perovskite solar cells at high temperatures and humidity. *Journal of Materials Chemistry A* **2015,** *3* (15), 8139-8147.

(71) Saliba, M.; Matsui, T.; Domanski, K.; Seo, J.-Y.; Ummadisingu, A.; Zakeeruddin, S. M.; Correa-Baena, J.-P.; Tress, W. R.; Abate, A.; Hagfeldt, A. Incorporation of rubidium cations into perovskite solar cells improves photovoltaic performance. *Science* **2016,** *354* (6309), 206-209.

(72) Conings, B.; Drijkoningen, J.; Gauquelin, N.; Babayigit, A.; D'Haen, J.; D'Olieslaeger, L.; Ethirajan, A.; Verbeeck, J.; Manca, J.; Mosconi, E. Intrinsic thermal instability of methylammonium lead trihalide perovskite. *Advanced Energy Materials* **2015,** *5* (15).

(73) Gottesman, R.; Zaban, A. Perovskites for Photovoltaics in the Spotlight: Photoinduced Physical Changes and Their Implications. *Accounts of Chemical Research* **2016,** *49* (2), 320-329, DOI: 10.1021/acs.accounts.5b00446.

(74) Klug, M. T.; Osherov, A.; Haghighirad, A. A.; Stranks, S. D.; Brown, P. R.; Bai, S.; Wang, J. T.-W.; Dang, X.; Bulović, V.; Snaith, H. J. Tailoring metal halide perovskites through metal substitution: influence on photovoltaic and material properties. *Energy & Environmental Science* **2017,** *10* (1), 236-246.

(75) Lu, K.; Lei, Y.; Qi, R.; Liu, J.; Yang, X.; Jia, Z.; Liu, R.; Xiang, Y.; Zheng, Z. Fermi level alignment by copper doping for efficient ITO/perovskite junction solar cells. *Journal of Materials Chemistry A* **2017,** *5* (48), 25211-25219.

(76) Jahandar, M.; Heo, J. H.; Song, C. E.; Kong, K.-J.; Shin, W. S.; Lee, J.-C.; Im, S. H.; Moon, S.-J. Highly efficient metal halide substituted CH3NH3I (PbI2) 1− X (CuBr2) X planar perovskite solar cells. *Nano Energy* **2016,** *27*, 330-339.

(77) Zhao, W.; Yao, Z.; Yu, F.; Yang, D.; Liu, S. F. Alkali Metal Doping for Improved CH3NH3PbI3 Perovskite Solar Cells. *Advanced Science* **2018,** *5* (2).

(78) Jin, J.; Li, H.; Chen, C.; Zhang, B.; Xu, L.; Dong, B.; Song, H.; Dai, Q. Enhanced Performance of Perovskite Solar Cells with Zinc Chloride Additives. *ACS applied materials & interfaces* **2017,** *9* (49), 42875-42882.

(79) Zhang, J.; Shang, M.-h.; Wang, P.; Huang, X.; Xu, J.; Hu, Z.; Zhu, Y.; Han, L. n-Type Doping and Energy States Tuning in CH3NH3Pb1–x Sb2 x/3I3 Perovskite Solar Cells. *ACS Energy Letters* **2016,** *1* (3), 535-541.

(80) Shai, X.; Zuo, L.; Sun, P.; Liao, P.; Huang, W.; Yao, E.-P.; Li, H.; Liu, S.; Shen, Y.; Yang, Y. Efficient planar perovskite solar cells using halide Sr-substituted Pb perovskite. *Nano Energy* **2017,** *36*, 213-222.

(81) Chen, Q.; Chen, L.; Ye, F.; Zhao, T.; Tang, F.; Rajagopal, A.; Jiang, Z.; Jiang, S.; Jen, A. K.-Y.; Xie, Y. Ag-incorporated organic–inorganic perovskite films and planar heterojunction solar cells. *Nano letters* **2017,** *17* (5), 3231-3237.

(82) Lu, C.; Zhang, J.; Hou, D.; Gan, X.; Sun, H.; Zeng, Z.; Chen, R.; Tian, H.; Xiong, Q.; Zhang, Y. Calcium doped MAPbI3 with better energy state alignment in perovskite solar cells. *Applied Physics Letters* **2018,** *112* (19), 193901.

(83) Zhang, H.; Shang, M.-h.; Zheng, X.; Zeng, Z.; Chen, R.; Zhang, Y.; Zhang, J.; Zhu, Y. Ba2+ Doped CH3NH3PbI3 to Tune the Energy State and Improve the Performance of Perovskite Solar Cells. *Electrochimica Acta* **2017,** *254*, 165-171.

(84) Pérez-del-Rey, D.; Forgács, D.; Hutter, E. M.; Savenije, T. J.; Nordlund, D.; Schulz, P.; Berry, J. J.; Sessolo, M.; Bolink, H. J. Strontium Insertion in Methylammonium Lead Iodide: Long Charge Carrier Lifetime and High Fill-Factor Solar Cells. *Advanced Materials* **2016,** *28* (44), 9839-9845.

(85) Ali, R.; Hou, G.-J.; Zhu, Z.-G.; Yan, Q.-B.; Zheng, Q.-R.; Su, G. Predicted Lead-Free Perovskites for Solar Cells. *Chemistry of Materials* **2018**.

(86) Yang, F.; Kapil, G.; Zhang, P.; Hu, Z.; Kamarudin, M. A.; Ma, T.; Hayase, S. Dependence of Acetate-Based Antisolvents for High Humidity Fabrication of CH3NH3PbI3 Perovskite Devices in Ambient Atmosphere. *ACS Applied Materials & Interfaces* **2018,** *10* (19), 16482-16489, DOI: 10.1021/acsami.8b02554.

(87) Fu, Y.; Akmal, K. M.; PuTao, Z.; Gaurav, K.; Tingli, M.; Shuzi, H. Enhanced Crystallization by Methanol Additive in Anti-solvent for Achieving High-quality MAPbI3 Perovskite Films in Humid Atmosphere. *ChemSusChem 0* (ja), DOI: doi:10.1002/cssc.201800625.

(88) Gujar, T. P.; Unger, T.; Schönleber, A.; Fried, M.; Panzer, F.; van Smaalen, S.; Köhler, A.; Thelakkat, M. The role of PbI 2 in CH 3 NH 3 PbI 3 perovskite stability, solar cell parameters and device degradation. *Physical Chemistry Chemical Physics* **2018,** *20* (1), 605-614.

(89) Zheng, X.; Chen, B.; Dai, J.; Fang, Y.; Bai, Y.; Lin, Y.; Wei, H.; Zeng, X. C.; Huang, J. Defect passivation in hybrid perovskite solar cells using quaternary ammonium halide anions and cations. *Nature Energy* **2017,** *2* (7), 17102.

(90) Yamada, Y.; Miura, M.; Tajima, K.; Okada, M.; Yoshimura, K. Pd distribution of switchable mirrors based on Mg–Y alloy thin films. *Solar Energy Materials and Solar Cells* **2014,** *120*, 631-634.

(91) Cai, Q.; Li, H.; Jiang, Y.; Tu, L.; Ma, L.; Wu, X.; Yang, S.-e.; Shi, Z.; Zang, J.; Chen, Y. High-efficiency perovskite solar cells based on MAI(PbI2)1−x(FeCl2)x absorber layers. *Solar Energy* **2018,** *159*, 786-793, DOI: https://doi.org/10.1016/j.solener.2017.11.063.

(92) Ito, N.; Kamarudin, M. A.; Hirotani, D.; Zhang, Y.; Shen, Q.; Ogomi, Y.; Iikubo, S.; Minemoto, T.; Yoshino, K.; Hayase, S. Mixed Sn–Ge Perovskite for Enhanced Perovskite Solar Cell Performance in Air. *The journal of physical chemistry letters* **2018,** *9* (7), 1682-1688.

(93) Ristein, J.; Stein, W.; Ley, L. Defect spectroscopy and determination of the electron diffusion length in single crystal diamond by total photoelectron yield spectroscopy. *Physical review letters* **1997,** *78* (9), 1803.

(94) Guo, Y.; Liu, C.; Inoue, K.; Harano, K.; Tanaka, H.; Nakamura, E. Enhancement in the efficiency of an organic–inorganic hybrid solar cell with a doped P3HT hole-transporting layer on a void-free perovskite active layer. *Journal of Materials Chemistry A* **2014,** *2* (34), 13827-13830.

(95) Zhang, Y.; Feng, J. CH3NH3Pb1− x Mg x I3 perovskites as environmentally friendly photovoltaic materials. *AIP Advances* **2018,** *8* (1), 015218.

(96) Lu, J.; Jiang, L.; Li, W.; Li, F.; Pai, N. K.; Scully, A. D.; Tsai, C. M.; Bach, U.; Simonov, A. N.; Cheng, Y. B. Diammonium and Monoammonium Mixed-Organic-Cation Perovskites for High Performance Solar Cells with Improved Stability. *Advanced Energy Materials* **2017,** *7* (18).

(97) Qiu, W.; Merckx, T.; Jaysankar, M.; de la Huerta, C. M.; Rakocevic, L.; Zhang, W.; Paetzold, U.; Gehlhaar, R.; Froyen, L.; Poortmans, J. Pinhole-free perovskite films for efficient solar modules. *Energy & Environmental Science* **2016,** *9* (2), 484-489.

(98) Kim, H. D.; Ohkita, H.; Benten, H.; Ito, S. Photovoltaic performance of perovskite solar cells with different grain sizes. *Advanced materials* **2016,** *28* (5), 917-922.

(99) Chen, R.; Hou, D.; Lu, C.; Zhang, J.; Liu, P.; Tian, H.; Zeng, Z.; Xiong, Q.; Hu, Z.; Zhu, Y. Zinc ion as effective film morphology controller in perovskite solar cells. *Sustainable Energy & Fuels* **2018,** *2* (5), 1093-1100.

(100) Chan, S.-H.; Wu, M.-C.; Lee, K.-M.; Chen, W.-C.; Lin, T.-H.; Su, W.-F. Enhancing perovskite solar cell performance and stability by doping barium in methylammonium lead halide. *Journal of Materials Chemistry A* **2017,** *5* (34), 18044-18052.

(101) Kim, H.-S.; Jang, I.-H.; Ahn, N.; Choi, M.; Guerrero, A.; Bisquert, J.; Park, N.-G. Control of I–V hysteresis in CH3NH3PbI3 perovskite solar cell. *The journal of physical chemistry letters* **2015,** *6* (22), 4633-4639.

(102) Aristidou, N.; Eames, C.; Sanchez-Molina, I.; Bu, X.; Kosco, J.; Islam, M. S.; Haque, S. A. Fast oxygen diffusion and iodide defects mediate oxygen-induced degradation of perovskite solar cells. *Nature Communications* **2017,** *8*, 15218.

(103) Christians, J. A.; Schulz, P.; Tinkham, J. S.; Schloemer, T. H.; Harvey, S. P.; de Villers, B. J. T.; Sellinger, A.; Berry, J. J.; Luther, J. M. Tailored interfaces of

unencapsulated perovskite solar cells for> 1,000 hour operational stability. *Nature Energy* **2018,** *3* (1), 68.

(104) Sun, Q.; Fassl, P.; Becker‐Koch, D.; Bausch, A.; Rivkin, B.; Bai, S.; Hopkinson, P. E.; Snaith, H. J.; Vaynzof, Y. Role of Microstructure in Oxygen Induced Photodegradation of Methylammonium Lead Triiodide Perovskite Films. *Advanced Energy Materials* **2017,** *7* (20).

(105) Chen, Y.; Sun, Y.; Peng, J.; Tang, J.; Zheng, K.; Liang, Z. 2D Ruddlesden–Popper Perovskites for Optoelectronics. *Advanced Materials* **2018,** *30* (2), 1703487.

(106) Kamminga, M. E.; Fang, H.-H.; Filip, M. R.; Giustino, F.; Baas, J.; Blake, G. R.; Loi, M. A.; Palstra, T. T. Confinement Effects in Low-Dimensional Lead Iodide Perovskite Hybrids. *Chemistry of Materials* **2016,** *28* (13), 4554-4562.

(107) K Misra, R.; Cohen, B.-E.; Iagher, L.; Etgar, L. Low dimensional organic‐inorganic halide perovskite: structure, properties, and applications. *ChemSusChem* **2017**.

(108) Qing, J.; Liu, X. K.; Li, M.; Liu, F.; Yuan, Z.; Tiukalova, E.; Yan, Z.; Duchamp, M.; Chen, S.; Wang, Y. Aligned and Graded Type‐II Ruddlesden–Popper Perovskite Films for Efficient Solar Cells. *Advanced Energy Materials* **2018**, 1800185.

(109) Rodríguez-Romero, J.; Hames, B. C.; Mora-Sero, I.; Barea, E. M. Conjugated Organic Cations to Improve the Optoelectronic Properties of 2D/3D Perovskites. *ACS Energy Letters* **2017,** *2* (9), 1969-1970.

(110) Grancini, G.; Roldán-Carmona, C.; Zimmermann, I.; Mosconi, E.; Lee, X.; Martineau, D.; Narbey, S.; Oswald, F.; De Angelis, F.; Graetzel, M. One-Year stable perovskite solar cells by 2D/3D interface engineering. *Nature communications* **2017,** *8*, 15684.

(111) Yan, J.; Qiu, W.; Wu, G.; Heremans, P.; Chen, H. Recent progress on 2D/quasi-2D layered metal halide perovskites for solar cells. *Journal of Materials Chemistry A* **2018**.

(112) Yongyoon, C.; Mahboubi, S. A.; Sung, Y. J.; Jincheol, K.; Seul, L. D.; Jan, S.; Xiaofan, D.; A., G. M.; Shujuan, H.; Y., H. B. A. W. Mixed 3D–2D Passivation Treatment for Mixed‐Cation Lead Mixed‐Halide Perovskite Solar Cells for Higher Efficiency and Better Stability. *Advanced Energy Materials 0* (0), 1703392, DOI: doi:10.1002/aenm.201703392.

(113) Blancon, J.-C.; Tsai, H.; Nie, W.; Stoumpos, C. C.; Pedesseau, L.; Katan, C.; Kepenekian, M.; Soe, C. M. M.; Appavoo, K.; Sfeir, M. Y.; Tretiak, S.; Ajayan, P. M.; Kanatzidis, M. G.; Even, J.; Crochet, J. J.; Mohite, A. D. Extremely efficient internal exciton dissociation through edge states in layered 2D perovskites. *Science* **2017**, DOI: 10.1126/science.aal4211.

(114) Zhang, T.; Xie, L.; Chen, L.; Guo, N.; Li, G.; Tian, Z.; Mao, B.; Zhao, Y. In situ fabrication of highly luminescent bifunctional amino acid crosslinked 2D/3D NH3C4H9COO (CH3NH3PbBr3) n perovskite films. *Advanced Functional Materials* **2017,** *27* (1), 1603568.

(115) Zhang, T.; Dar, M. I.; Li, G.; Xu, F.; Guo, N.; Grätzel, M.; Zhao, Y. Bication lead iodide 2D perovskite component to stabilize inorganic α-CsPbI₃ perovskite phase for high-efficiency solar cells. *Science Advances* **2017,** *3* (9).

(116) Yang, F.; Kapil, G.; Zhang, P.; Hu, Z.; Kamarudin, M. A.; Ma, T.; Hayase, S. Dependence of Acetate-Based Antisolvents for High Humidity Fabrication of CH3NH3PbI3 Perovskite Devices in Ambient Atmosphere. *ACS applied materials & interfaces* **2018**.

(117) Jianfeng, L.; Liangcong, J.; Wei, L.; Feng, L.; K., P. N.; D., S. A.; Cheng-Min, T.; Udo, B.; N., S. A.; Yi-Bing, C.; Leone, S. Diammonium and Monoammonium Mixed-Organic-Cation Perovskites for High Performance Solar Cells with Improved Stability. *Advanced Energy Materials* **2017,** *7* (18), 1700444, DOI: doi:10.1002/aenm.201700444.

(118) Chen, C.; Xu, Y.; Wu, S.; Zhang, S.; Yang, Z.; Zhang, W.; Zhu, H.; Xiong, Z.; Chen, W.; Chen, W. CaI 2: a more effective passivator of perovskite films than PbI 2 for high efficiency and long-term stability of perovskite solar cells. *Journal of Materials Chemistry A* **2018,** *6* (17), 7903-7912.

(119) Cohen, B. E.; Wierzbowska, M.; Etgar, L. High Efficiency and High Open Circuit Voltage in Quasi 2D Perovskite Based Solar Cells. *Advanced Functional Materials* **2017,** *27* (5).

(120) Cao, D. H.; Stoumpos, C. C.; Farha, O. K.; Hupp, J. T.; Kanatzidis, M. G. 2D homologous perovskites as light-absorbing materials for solar cell applications. *Journal of the American Chemical Society* **2015,** *137* (24), 7843-7850.

(121) Milot, R. L.; Sutton, R. J.; Eperon, G. E.; Haghighirad, A. A.; Martinez Hardigree, J.; Miranda, L.; Snaith, H. J.; Johnston, M. B.; Herz, L. M. Charge-carrier dynamics in 2D hybrid metal–halide perovskites. *Nano letters* **2016,** *16* (11), 7001-7007.

(122) Manser, J. S.; Saidaminov, M. I.; Christians, J. A.; Bakr, O. M.; Kamat, P. V. Making and breaking of lead halide perovskites. *Accounts of chemical research* **2016,** *49* (2), 330-338.

(123) Wang, S.; Jiang, Y.; Juarez-Perez, E. J.; Ono, L. K.; Qi, Y. Accelerated degradation of methylammonium lead iodide perovskites induced by exposure to iodine vapour. *Nature Energy* **2017,** *2* (1), 16195.

(124) Tsai, H.; Nie, W.; Blancon, J.-C.; Stoumpos, C. C.; Asadpour, R.; Harutyunyan, B.; Neukirch, A. J.; Verduzco, R.; Crochet, J. J.; Tretiak, S. High-efficiency two-dimensional Ruddlesden–Popper perovskite solar cells. *Nature* **2016,** *536* (7616), 312.

(125) Jialong, D.; Tianyu, H.; Yuanyuan, Z.; Benlin, H.; Qunwei, T. Carbon-Electrode-Tailored All-Inorganic Perovskite Solar Cells To Harvest Solar and Water-Vapor Energy. *Angewandte Chemie International Edition* **2018,** *57* (20), 5746-5749, DOI: doi:10.1002/anie.201801837.

(126) Liang, J.; Zhao, P.; Wang, C.; Wang, Y.; Hu, Y.; Zhu, G.; Ma, L.; Liu, J.; Jin, Z. CsPb0. 9Sn0. 1IBr2 Based All-Inorganic Perovskite Solar Cells with Exceptional Efficiency and Stability. *Journal of the American Chemical Society* **2017,** *139* (40), 14009-14012.

(127) Li, N.; Zhu, Z.; Li, J.; Jen, A. K. Y.; Wang, L. Inorganic CsPb1− xSnxIBr2 for Efficient Wide-Bandgap Perovskite Solar Cells. *Advanced Energy Materials* **2018**, 1800525.

(128) Eperon, G. E.; Paterno, G. M.; Sutton, R. J.; Zampetti, A.; Haghighirad, A. A.; Cacialli, F.; Snaith, H. J. Inorganic caesium lead iodide perovskite solar cells. *Journal of Materials Chemistry A* **2015,** *3* (39), 19688-19695.

(129) Protesescu, L.; Yakunin, S.; Bodnarchuk, M. I.; Krieg, F.; Caputo, R.; Hendon, C. H.; Yang, R. X.; Walsh, A.; Kovalenko, M. V. Nanocrystals of cesium lead halide perovskites (CsPbX3, X= Cl, Br, and I): novel optoelectronic materials showing bright emission with wide color gamut. *Nano letters* **2015,** *15* (6), 3692-3696.

(130) Duan, J.; Zhao, Y.; He, B.; Tang, Q. High-Purity Inorganic Perovskite Films for Solar Cells with 9.72% Efficiency. *Angewandte Chemie* **2018,** *130* (14), 3849-3853.

(131) Liu, C.; Li, W.; Zhang, C.; Ma, Y.; Fan, J.; Mai, Y. All-inorganic CsPbI2Br perovskite solar cells with high efficiency exceeding 13%. *Journal of the American Chemical Society* **2018,** *140* (11), 3825-3828.

(132) Jeon, N. J.; Noh, J. H.; Kim, Y. C.; Yang, W. S.; Ryu, S.; Seok, S. I. Solvent engineering for high-performance inorganic–organic hybrid perovskite solar cells. *Nature materials* **2014,** *13* (9), 897.

(133) Swarnkar, A.; Marshall, A. R.; Sanehira, E. M.; Chernomordik, B. D.; Moore, D. T.; Christians, J. A.; Chakrabarti, T.; Luther, J. M. Quantum dot–induced phase stabilization of α-CsPbI3 perovskite for high-efficiency photovoltaics. *Science* **2016,** *354* (6308), 92-95.

(134) Sharma, S.; Weiden, N.; Weiss, A. Phase diagrams of quasibinary systems of the type: ABX3—A′ BX3; ABX3—AB′ X3, and ABX3—ABX′ 3; X= halogen. *Zeitschrift für Physikalische Chemie* **1992,** *175* (1), 63-80.

(135) Mariotti, S.; Hutter, O. S.; Phillips, L. J.; Yates, P. J.; Kundu, B.; Durose, K. Stability and Performance of CsPbI2Br Thin Films and Solar Cell Devices. *ACS Applied Materials & Interfaces* **2018,** *10* (4), 3750-3760, DOI: 10.1021/acsami.7b14039.

(136) Zeng, Z.; Zhang, J.; Gan, X.; Sun, H.; Shang, M.; Hou, D.; Lu, C.; Chen, R.; Zhu, Y.; Han, L. In Situ Grain Boundary Functionalization for Stable and Efficient Inorganic CsPbI2Br Perovskite Solar Cells. *Advanced Energy Materials* **2018**, 1801050.

(137) Yan, L.; Xue, Q.; Liu, M.; Zhu, Z.; Tian, J.; Li, Z.; Chen, Z.; Chen, Z.; Yan, H.; Yip, H. L. Interface Engineering for All‐Inorganic CsPbI2Br Perovskite Solar Cells with Efficiency over 14%. *Advanced Materials* **2018**, 1802509.

(138) Bai, D.; Zhang, J.; Jin, Z.; Bian, H.; Wang, K.; Wang, H.; Liang, L.; Wang, Q.; Liu, S. F. Interstitial Mn2+-driven high-aspect-ratio grain growth for low-trap-density

microcrystalline films for record efficiency CsPbI2Br solar cells. *ACS Energy Letters* **2018,** *3* (4), 970-978.

(139) Nam, J. K.; Chai, S. U.; Cha, W.; Choi, Y. J.; Kim, W.; Jung, M. S.; Kwon, J.; Kim, D.; Park, J. H. Potassium incorporation for enhanced performance and stability of fully inorganic cesium lead halide perovskite solar cells. *Nano letters* **2017,** *17* (3), 2028-2033.

(140) Lau, C. F. J.; Zhang, M.; Deng, X.; Zheng, J.; Bing, J.; Ma, Q.; Kim, J.; Hu, L.; Green, M. A.; Huang, S.; Ho-Baillie, A. Strontium-Doped Low-Temperature-Processed CsPbI2Br Perovskite Solar Cells. *ACS Energy Letters* **2017,** *2* (10), 2319-2325, DOI: 10.1021/acsenergylett.7b00751.

(141) Rödel, J.; Jo, W.; Seifert, K. T.; Anton, E. M.; Granzow, T.; Damjanovic, D. Perspective on the development of lead-free piezoceramics. *Journal of the American Ceramic Society* **2009,** *92* (6), 1153-1177.

(142) Sutton, R. J.; Eperon, G. E.; Miranda, L.; Parrott, E. S.; Kamino, B. A.; Patel, J. B.; Hörantner, M. T.; Johnston, M. B.; Haghighirad, A. A.; Moore, D. T. Bandgap-tunable cesium lead halide perovskites with high thermal stability for efficient solar cells. *Advanced Energy Materials* **2016,** *6* (8).

(143) Chen, C. Y.; Lin, H. Y.; Chiang, K. M.; Tsai, W. L.; Huang, Y. C.; Tsao, C. S.; Lin, H. W. All-Vacuum-Deposited Stoichiometrically Balanced Inorganic Cesium Lead Halide Perovskite Solar Cells with Stabilized Efficiency Exceeding 11%. *Advanced materials* **2017,** *29* (12), 1605290.

(144) Li, W.; Rothmann, M. U.; Liu, A.; Wang, Z.; Zhang, Y.; Pascoe, A. R.; Lu, J.; Jiang, L.; Chen, Y.; Huang, F. Phase Segregation Enhanced Ion Movement in Efficient Inorganic CsPbIBr2 Solar Cells. *Advanced Energy Materials* **2017,** *7* (20).

(145) Saliba, M.; Matsui, T.; Seo, J.-Y.; Domanski, K.; Correa-Baena, J.-P.; Nazeeruddin, M. K.; Zakeeruddin, S. M.; Tress, W.; Abate, A.; Hagfeldt, A. Cesium-containing triple cation perovskite solar cells: improved stability, reproducibility and high efficiency. *Energy & Environmental Science* **2016,** *9* (6), 1989-1997.

(146) Xu, W.; Zheng, L.; Zhang, X.; Cao, Y.; Meng, T.; Wu, D.; Liu, L.; Hu, W.; Gong, X. Efficient Perovskite Solar Cells Fabricated by Co Partially Substituted Hybrid Perovskite. *Advanced Energy Materials* **2018,** *8* (14), 1703178.

(147) Shen, H.; Duong, T.; Wu, Y.; Peng, J.; Jacobs, D.; Wu, N.; Weber, K.; White, T.; Catchpole, K. Metal halide perovskite: a game-changer for photovoltaics and solar devices via a tandem design. *Science and Technology of Advanced Materials* **2018,** *19* (1), 53-75, DOI: 10.1080/14686996.2017.1422365.

(148) Fan, R.; Zhou, N.; Zhang, L.; Yang, R.; Meng, Y.; Li, L.; Guo, T.; Chen, Y.; Xu, Z.; Zheng, G. Toward full solution processed perovskite/Si monolithic tandem solar device with PCE exceeding 20%. *Solar RRL* **2017,** *1* (11), 1700149.

(149) Leijtens, T.; Bush, K. A.; Prasanna, R.; McGehee, M. D. Opportunities and challenges for tandem solar cells using metal halide perovskite semiconductors. *Nature Energy* **2018**, DOI: 10.1038/s41560-018-0190-4.

(150) Lal, N. N.; Dkhissi, Y.; Li, W.; Hou, Q.; Cheng, Y. B.; Bach, U. Perovskite tandem solar cells. *Advanced Energy Materials* **2017,** *7* (18), 1602761.

(151) Eperon, G. E.; Leijtens, T.; Bush, K. A.; Prasanna, R.; Green, T.; Wang, J. T.-W.; McMeekin, D. P.; Volonakis, G.; Milot, R. L.; May, R. Perovskite-perovskite tandem photovoltaics with optimized band gaps. *Science* **2016,** *354* (6314), 861-865.

(152) Fu, Y.; Akmal, K. M.; Putao, Z.; Gaurav, K.; Tingli, M.; Shuzi, H. Enhanced Crystallization by Methanol Additive in Antisolvent for Achieving High-Quality MAPbI3 Perovskite Films in Humid Atmosphere. *ChemSusChem* **2018,** *11* (14), 2348-2357, DOI: doi:10.1002/cssc.201800625.

Achievements

Publication

(1) Yang, F, D. Hirotani, G. Kapil, M. A. Kamarudin, C. H. Ng, Y. H. Zhang, Q. Shen, S. Hayase* All-Inorganic $CsPb_{1-x}Ge_xI_2Br$ Perovskite with Enhanced Phase Stability and Photovoltaic Performance. **Angewandte chemie**, **2018,** 57 (39), 12745-12749, DOI: doi:10.1002/anie.201807270. **(IF=12.102)**

(2) Yang, F. , Zhang, P. , Kamarudin, M. A., Kapil, G. , Ma, T. and Hayase, S. (2018), Addition Effect of Pyreneammonium Iodide to Methylammonium Lead Halide Perovskite-2D/3D Hetero Structured Perovskite with Enhanced Stability. **Advanced functional materials**, **2018,** 28**,** 1804856. **(IF=13.325)**

(3) Yang, F. , Kamarudin, M. A., Zhang, P. , Kapil, G. , Ma, T. and Hayase, S. Enhanced Crystallization by Methanol Additive in Antisolvent for Achieving High-Quality $MAPbI_3$ Perovskite Films in Humid Atmosphere. **ChemSusChem**, 2018, 11, 2348. DOI: doi.org/10.1002/cssc.201800625. **(IF=7.411, cover feature)**

(4) Yang, F.; Kamarudin, M. A.; Kapil, G.; Hirotani, D.; Zhang, P.; Ng, C. H.; Ma, T.; Hayase, S. Magnesium-Doped $MAPbI_3$ Perovskite Layers for Enhanced Photovoltaic Performance in Humid Air Atmosphere. ***ACS Applied Materials & Interfaces,*** **2018**, 10 (29), 24543-24548, DOI: 10.1021/acsami.8b06619. **(IF=8.097)**

(5) Yang, F.; Kapil, G.; Zhang, P.; Hu, Z.; Kamarudin, M. A.; Ma, T.; Hayase, S. Dependence of AcetateBased Antisolvents for High Humidity Fabrication of $CH_3NH_3PbI_3$

Perovskite Devices in Ambient Atmosphere. ***ACS Applied Materials & Interfaces,*** **2018,** *10* (19), 16482-16489, DOI: 10.1021/acsami.8b02554. **(IF=8.097)**

(6) Yang, F, Zhang, P. T, G. Kapil, M. A. Kamarudin, C. H. Ng, S. Hayase* Melamine Functioned $MAPbI_3$ for 2D/3D Hetero Structured Perovskite with Enhanced Photovoltaic Performance and Stability in Ambient Atmosphere, **Solar RRL, 2018,** in press.

(7) Zhang, P.T., **Yang, F.,** Kapil, G., Shen, Q., Toyoda, T., Yoshino, K., & Hayase, S. (2018). Enhanced performance of ZnO based perovskite solar cells by Nb_2O_5 surface passivation. ***Organic Electronics 2018, in press***.**(IF=3.680)**

(8) Zhang, P.T., **Yang, F.,** Kamarudin, M. A.; C. H. Ng; Ma, T. and Hayase, S. (2018), Performance enhancement of mesoporous TiO_2-based perovskite solar cells by SbI_3 interfacial modification layer. ***ACS Applied Materials & Interfaces,*** **2018**, 10 (35), 29630-29637. *DOI: 10.1021/acsami.8b10062.* **(IF=8.097)**

Conference

(1) The 79th The Japan Society of Applied Physics (JSAP) Autumn Meeting (2018.09.18-2018.09.21), Tokyo (Japan) Poster Presentation. Title: Dependence of acetate-based anti-solvents on $CH_3NH_3PbI_3$ perovskite solar cells performances in high humidity air condition.

(2) The 79th The Japan Society of Applied Physics (JSAP) Spring Meeting (2018.03.18-2018.03.21), Oral Presentation. Nagoya (Japan), Title: Methanol Additive in Diethyl Ether Antisolvent for High-Quality $MAPbI_3$ Perovskite Films in Ambient Atmosphere

(3) 2018 MRS (Materials Research Society) Fall Meeting and Exhibit (2018.11.26-2018.12.01), Boston (America), Oral Presentation. Title: Effect of GeI_2 addition to inorganic

perovskite $CsPbI_2Br$ perovskite for enhancing efficiency and stabilization of αphase at room temperature

(4) IPEROP-19 Asia-Pacific International Conference on Perovskite, Organic Photovoltaics and Optoelectronics (2019.01.28-2018.0129), Kyoto (Japan), Poster Presentation. Title: Solvent engineering method for $CsPb_{1-x}Ge_xI_2Br$ perovskite with high phase stability and photovoltaic performance

Acknowledgement

First, I would like to express my deepest thanks to my supervisor Professor Shuzi Hayase. He gave me this wonderful opportunity to study and live in Japan. I admire his knowledge and personality. During my doctor course study, he gives me countless advices to my research and life.

Second, I would like to express my sincere gratitude to Professor Tingli Ma and Professor Shyam Pandey. Because of the recommendation of Professor Ma, I have the chance to join in the Professor Hayase lab as a doctor course student. She is very knowledgeable and creative and gives me many good advices to my research and life. Professor Shyam Pandey is kind, warmhearted has many creative skills on experiments. He gave me many suggestions for my research.

Third, I also like to thank my collaborators Professor Qing Shen and Professor Kenji Yoshino for their kind supply on my research.

Forth, I would like to thank all the members in the Hayase-Pandey & Ma laboratory, including Dr. Gaurav Kapil, Dr. Muhammad Akmal Kamarudin, Dr. Ripolles S. Teresa, Dr. Chi Huey Ng, Dr. Ajay Kumar Baranwal, Dr. Zhiguo Zhang, Dr. Xiao Huang, Dr. Zhaosheng Hu, Mr. Putao Zhang, Mr. Zhen Wang, Mr. Chu Zhang, Mr. Zhanglin guo, Mr. Kengo Hamada, Mr. Daisuke Hirotani, Mr. Nam Kyungsu, Mr. Yuma Hoshiba, Mr. Takehide Sato, Mr. Kazunari Tanaka, Miss Anusha Pradhan, Miss Megumi Furuta Mr. Kazuhiko Sakamoto, Miss Nishimura, Mr. Shimazaki et al. They helped me a lot on my experiments and daily life. And let me feel like in a big warm family.

Last, I would like to express my thanks to my family, including my parents, my sister and my wife. Their support and encouragement have always inspired me to fight for a better

research work and a better life in the future. Finally, I also expressed my gratitude to the persons who once made contribution to this thesis, I feel sorry but I could not show my thanks to them one by one.